

University of Nevada

Reno

✓
Source Functions, Site Response and Spectral Attenuation
in the Guerrero, Mexico Subduction Zone

A dissertation submitted in partial fulfillment of the
requirements for the degree of Doctor of Philosophy
in Geophysics

by

Raul Ramon Castro Escamilla

May 1991

The dissertation of Raul R. Castro Escamilla is approved:

John G. Anderson

Dissertation Adviser

M. W. W. W.

Department Chair

Ronald C. Dillely

Dean, Graduate School

University of Nevada

Reno

UNR LIBRARY

May 1991

ACKNOWLEDGMENTS

I feel fortunate for having John Anderson as my adviser. I am indebted to him not only for his support but also for sharing his knowledge and friendship.

Many of the ideas developed in this thesis (and a few still cooking) were motivated from lectures and discussions with Jim Brune.

I also want to acknowledge advisory committee members Keith Priestley, Steve Wesnousky, Robert Tompson and Rajaratnam Siddharthan. Notes from lectures on Integral Transforms by Robert Tompson proved to be very useful. I also benefited from discussions and lectures on soil dynamics from Rajaratnam Siddharthan, and I certainly enjoyed and learned from the Active Faulting lectures given by Steve Wesnousky.

In addition, I would like to thank all the graduate students and staff at the Mackay School of Mines for the friendly experiences and their cooperation whenever it was needed.

The material presented in Chapter 1 has recently been published and was coauthored with John Anderson and Shri Krishna Singh. Chapter 2 has also been submitted and coauthored with John Anderson and Jim Brune. Comments about this chapter by Bill Peppin, Peggy Johnson and Bill Walter are also appreciated.

This research was funded by Grants EAR-88-18641 and CES/BCS-88-08357 from the National Science Foundation. I also acknowledge support during my first three years at UNR from the Mexican National Council of Science and Technology (CONACYT).

Finally, I would like to thank my wife Shellie for her help and wonderful sense of humor during the preparation of this thesis.

ABSTRACT

Strong motion records digitally recorded on an accelerograph array installed since 1985 above the Guerrero, Mexico subduction zone are inverted to find the source spectra, the site response, and the quality factor Q of S waves. Results obtained using a two-step inversion and a complete parametric approach are not significantly different. We assume that the geometrical spreading is proportional to the inverse of the hypocentral distance and find that the frequency dependence of Q for frequencies $f > 0.8$ Hz does not follow a simple linear relation as observed in previous studies of attenuation in other regions. When the source spectra are interpreted in terms of Brune's model, the stress drops obtained are less than 20 bars for the larger events analyzed. The site functions obtained indicate that although all the stations used are on rock, the effect of the near surface geology caused important amplifications at some stations.

An extended data set from the same region was also used to analyze ratios of spectral amplitudes of P-wave radiation relative to S. P-wave spectra from the Guerrero events frequently equal or exceed the S-wave spectra at high frequencies ($f > 10$ Hz). Attenuation alone cannot account for such high ratios. This result is not predicted by simple dislocation models of earthquakes. To explain the results, Haskell's (1964) formulation was used to calculate the energy radiated by a shear fault, with energy from tensile motion superimposed. Small motions normal to the fault can account for P/S spectral ratios close to one. These results suggest that fault normal motions may be causing the anomalous P-wave radiation observed.

Numerical dislocation models based on Haskell's (1969) formulation are also used to estimate the magnitude of the normal motions necessary to produce the high P/S spectral ratios observed. Although these models depend on the nature of the assumed dislocations, a normal motion with amplitude of less than 10 % of the amplitude of shear slip is sufficient to produce P/S values comparable with the observations.

THE RESPONSE AT LOCATION AND SOURCE
SPECTRA OF S WAVES

Introduction	40
One	40
Method of Analysis	40
Discussion	40
Conclusions	40
References	40

II. P/S SPECTRAL RATIOS FROM THE JITTERED
ACCELEROGRAPH ARRAY

Introduction	41
Discrete Components	41
Example One	41
Four-Event Record Observations	41
Peak Ratio Correlation	41
Discussion	41
References	41

III. P AND S-WAVE DISPLACEMENTS FROM KINEMATIC
DISLOCATION MODELS

Introduction	42
Sensitivity to Source Time Function	42
Models that Incorporate Both Slips and Tensile Motions	42
Discussion and Conclusions	42
References	42

TABLE OF CONTENTS

INTRODUCTION	1
Chapter	
I. SITE RESPONSE, ATTENUATION AND SOURCE	
SPECTRA OF S WAVES	6
Introduction	6
Data	8
Method of Analysis	14
Discussion	33
Conclusions	43
References	45
II. P/S SPECTRAL RATIOS FROM THE GUERRERO	
ACCELEROGRAPH ARRAY	48
Introduction	48
Diagnostic Characteristics	50
Guerrero Data Set	61
P and S-wave Spectral Observations	64
Path Effect Cancellation	76
Discussion	83
References	85
III. P AND S-WAVE DISPLACEMENTS FROM KINEMATIC	
DISLOCATION MODELS	88
Introduction	88
Sensitivity to Source Time Function	89
Models that Incorporate Both Shear and Tensile Motions	96
Discussion and Conclusions	111
References	114

Appendices

A.	116
B.	119

APPENDIX A

One of the most important problems in geophysics is reaching a full understanding of the various processes, such as generation, reflection, mode and size migration, that influence ground motion. We describe here a number of characteristics of the structure and geometry of the Earth's crust, and the analysis of it. The structure of the Earth's crust is described in detail in the elastic properties of the material, which are used and through which the seismic waves.

The fundamental characteristics of the waves in the Earth, the structure and the propagation of the waves generally are important factors causing a complex behavior of waves at high frequency. Many studies of earthquakes determine the structure of the Earth's crust (P-wave, 1984) that can be explained for these factors.

The seismic waves in the elastic velocity structure of the Earth between the crust and mantle. Most of the waves in the crust are generated through mode conversion at different depths and elastic properties. During propagation, the waves and stress applied to the material may produce irreversible changes in the media. This process, called internal friction (Lauritzen and Stroh, 1987), causes energy loss in the elastic properties of the material and as a result, the waves attenuate along their path. The velocity of the waves is affected with the parameter called Q ($Q = \frac{1}{\sin^2 \theta} - \frac{1}{\cos^2 \theta}$) the energy loss per cycle. Attenuation is more significant at high frequencies because the wave travel more cycles between two points and time.

INTRODUCTION

One of the most important problems in seismology is reaching a full understanding of the various processes, such as attenuation, seismic source and site response, that affect the ground motion. The seismic source is basically characterized by the dimension and geometry of the rupture area, and the amount of slip. The radiation of seismic waves from the source also depends on the elastic properties of the material and the stress and strength near the rupture area.

The heterogeneous distribution of the strength on the faults, the friction and the irregularities of the fault geometry are important factors causing a complex radiation of energy at high frequency. Many studies of earthquakes document the occurrence of complex ruptures (Brune, 1990) that can be explained for these factors.

Propagation depends on the seismic velocity structure of the Earth between the source and receiver. Once the wave motion begins, the waves propagate through material with different composition and elastic properties. During propagation, the stresses and strains applied on the material may produce irreversible changes in the media. This process, called internal friction (Aki and Richards, 1980), causes imperfections in the elastic properties of the material and as a result, the waves attenuate along their path. The anelasticity of the media is quantified with the parameter called Q ($\frac{1}{Q(\omega)} = -\frac{\Delta E}{2\pi E}$, the energy lost per cycle). Anelasticity is most important at high frequencies because the waves travel more cycles between source and receiver.

Near the surface, where most of the records of earthquakes are obtained, drastic variations of the impedance (resistance to particle motion) due to changes in the lithology from hard rock to sediments or unconsolidated soils may amplify or further attenuate the seismic waves. High frequency waves are most affected by the strong near-surface variability of the velocity structure because the period of resonance of the shallow layers is comparable with the wavelengths propagating. Therefore, at high frequencies the identification and separation of the source, attenuation, and near surface effects is an interesting and important scientific problem.

In studying source processes, it is common to restrict the frequency band of the observations to less than 1 Hz (Langston and Helmberger, 1975; Kanamori and Stewart, 1976; Romanowicz and Monfret, 1986; among others), since at low frequencies propagation may be well approximated by vertically layered media. Thus, the strong interaction of source and propagation effects can be resolved. Ground motion at high frequencies ($f > 1$ Hz), however, is particularly important in earthquake engineering for studies of seismic risk. For these cases, the separation of the source and propagation effects becomes more difficult.

The main objective of this thesis is to study the source and propagation characteristics of body-waves generated by earthquakes recorded in the Guerrero, Mexico subduction zone. We also explore possible mechanisms to explain unexpectedly large amplitudes of high frequency radiation of P-waves, compared to S-waves, observed in many records from this region.

The Guerrero subduction zone is located along the west coast of Mexico. This region is known as the "Guerrero gap" because of the spatial break in the seismicity of the rupture zone. The last large earthquakes occurred in 1899 ($M=7.9$), 1908 ($M=7.0$) and 1911 ($M=7.6$) (Singh et al., 1981). Based on empirical relations between the average seismic moment and the average recurrence period in this region, Astiz et al. (1987) suggest a possible moment release of 10^{28} dyne-cm in a large event or a

sequence of small earthquakes. From the cumulative moment release of the Guerrero gap, Anderson, et al. (1989) estimated a slip rate of 6.2 cm/year which account for 90 % of the slip estimated from plate tectonics by Minster and Jordan (1978, 1979). Thus, the frequent occurrence of small and intermediate magnitude earthquakes and the high probability for a big event make the Guerrero gap a promising region to study subduction zone earthquakes.

A digital strong motion array has been operating in this region since 1985 (Anderson et al. 1986). Since the installation, the array has recorded on scale events at close hypocentral distances with magnitudes ranging from 2.2 to 8.1. The advantages of digital recording include high sampling rate (100 and 200 samples per second), high dynamic range and high signal to noise ratio. Because all the stations are located on granitic or metamorphic outcrops, data from this array provides a good opportunity to study several characteristics of the ground motion at high frequencies.

In the first part of this thesis, we study the decay of the spectral amplitudes with distance using intermediate magnitude ($4 < M < 7$) earthquakes recorded along the coast of Guerrero. We obtain attenuation curves for frequencies between 0.1 and 40 Hz. These attenuation curves are interpreted in terms of the specific attenuation $Q(f)$. In a second step, site effects and source functions are obtained by inverting the spectral amplitudes, after correction for attenuation. We also explore an alternative method to separate source and path effects from the spectral records. We adopt a parametric form for the attenuation and solve for Q , source, and site functions using a least-square inversion scheme. Since we do not constrain the source spectral functions to any particular shape, the results can be compared with parametric models proposed in the literature to infer the dynamics of the rupture. In addition, the resulting site functions can be used to analyze the variability of ground motions on rock sites.

Earthquake dislocation models (i.e. Aki, 1967; Brune, 1970) predict a body-wave spectral amplitude that is constant at low frequencies and that decays with frequency beyond a spectrum's corner frequency. Several models (Haskell, 1964; Savage, 1972) also predict the corner frequency of S to be equal or greater than that for P-waves. Other models predict higher corner frequencies for P waves (Molnar et al., 1973). Many studies of earthquakes report high amplitude P-wave radiation relative to S-wave at high frequencies (Hanks, 1981). In studying the spectral records from the Guerrero subduction zone, we also observed high P/S spectral amplitudes at high frequencies. Although these observations may reflect differences in the attenuation between P and S-waves, a complex rupture process may also be the cause. In the second part of the thesis (chapter 3), we study characteristics of the ground motion that can help to discriminate between source or propagation origin of the high P/S ratios observed in Guerrero, Mexico.

Recently, Brune et al. (1989) have suggested that normal fault motions are a characteristic of seismic faulting. If present, these would appear presumably at high frequencies because of the likely short-period nature of these normal vibrations. In the last part of the thesis (chapter 4), we study simple dislocation models, based on Haskell's (1969) formulation, that generate high P/S amplitude ratios. These numerical models are also used to estimate the magnitude of the normal motions necessary to produce the high P/S spectral ratios observed. In addition, since we used a homogeneous, isotropic, elastic space, we can reach a good understanding of the kinematics of the source that can be used to establish simple guide lines to distinguish path and source effects.

A complete understanding of high frequency waves has not yet been reached. This thesis however reports progress toward this goal in estimating the attenuation of S-waves for a wide band of frequencies ($0.1 < f < 40$ Hz), in evaluating the site response of hard rocks and in analyzing the radiation of P- and S-waves from kinematic source models.

REFERENCES

- Aki, K. (1967). Scaling law of seismic spectrum, *J. Geophys. Res.* 72, 1217-1231.
- Aki, K. and P. Richards (1980). *Quantitative Seismology: Theory and Methods*, W. H. Freeman, San Francisco.
- Anderson, J.G., P. Bodin, J.N. Brune, J. Prince, S.K. Singh, R. Quaas, and M. Onate (1986). Strong ground motion from the Michoacan, Mexico, earthquake, *Science*, 233, 1043-1049.
- Anderson, J.G., S.K. Singh, J.M. Espindola, and J. Yamamoto (1989). Seismic strain release in the Mexican subduction thrust, *Phys. Earth Planet. Inter.*, 58, 307-322.
- Astiz, L., H. Kanamori, and H. Eissler (1987). Source characteristics of earthquakes in the Michoacan seismic gap in Mexico, *Bull. Seism. Soc. Am.*, 77, 1326-1346.
- Brune, J.N. (1970). Tectonic stress and the spectra of seismic shear waves from earthquakes, *J. Geophys. Res.* 75, 4997-5009.
- Brune, J.N., P.A. Johnson and C. Slater (1989). Constitutive relations for foam rubber stick-slip, *Seis. Res. Lett.* 60, 26.
- Brune, J.N. (1990). Seismic source dynamics, radiation and stress, *Reviews of Geophysics*, Submitted.
- Hanks, T.C. (1981). The corner frequency shift, earthquake source models, and Q, *Bull. Seism. Soc. Am.*, 71, 597-612.
- Haskell, N.A. (1964). Total energy and energy spectral density of elastic wave radiation from propagating faults, *Bull. Seism. Soc. Am.*, 54, 1811-1841.
- Haskell, N.A. (1969). Elastic displacements in the near-field of a propagating fault, *Bull. Seism. Soc. Am.*, 59, 865-908.
- Kanamori, H. and G.S. Stewart (1976). Mode of strain release along the Gibbs fracture zone, Mid-Atlantic Ridge, *Phys. Earth Planet. Inter.*, 11, 312-332.
- Langston, C.A. and D.V. Helmberger (1975). A procedure for modeling shallow dislocation sources, *Geophys. J. R. Astr. Soc.*, 42, 117-130.
- Romanowicz, B. and T. Monfret (1986). Source process times of large earthquakes by moment tensor inversion of mantle waves and the effect of lateral heterogeneity, *Ann. Geophys.*, 4, B, 3, 271-283.
- Savage, J.C. (1972). Relation of corner frequency to fault dimensions, *J. Geoph. Res.* 77, 3788-3795.
- Singh, S.K., L. Astiz, and J. Havskov (1981). Seismic gaps and recurrence periods of large earthquakes along the Mexican subduction zone: A reexamination, *Bull. Seism. Soc. Am.*, 71, 827-843.

CHAPTER I

SITE RESPONSE, ATTENUATION AND SOURCE SPECTRA OF S WAVES

INTRODUCTION

The Guerrero Accelerograph Array (Anderson et al., 1986) provides an unequalled opportunity to study several characteristics of the ground motion induced by subduction earthquakes. The array has recorded, on scale and at close distances, ground motions from events with magnitudes ranging from less than 3 to 8.1, and several small and moderate earthquakes over a large range of distances (Anderson and Quaa, 1988). Thus, this high quality data set allows us to determine source spectra and estimates of Q . Since all the stations are sited on rock, and many of them have recorded several events, the strong motion records of the array can also be used to study the variability of ground motions on rock sites. Source functions, attenuation and site effects are important components needed for a study of the empirical characteristics of ground motions on rock sites.

We utilize two approaches to characterize the decay of spectral amplitudes with distance along the Guerrero subduction zone. The first approach is to seek a smooth description of the average amplitude as a function of distance without adopting any assumed parametric form. As pointed out by Baker et al. (1988), in the presence of crustal velocity gradients, the attenuation of body waves with distance may be more complicated than a simple $1/r$ geometrical spreading function and the non-parametric approach is intended to show the effect of any such complexities if they are present. The specific attenuation $Q(f)$ is obtained from the non-parametric curves in a second step. Site effects and source functions are also obtained after the spectral amplitudes are corrected for attenuation using the non-parametric curves.

The second approach is to adopt a parametric form for the attenuation and use a least squares inversion to obtain estimates of Q , source spectra and site response simultaneously. Here instead of using a two step inversion as in the first part of the analysis, we define an exponential attenuation function and specify the geometrical spreading to be either $1/r$ or $(1/r)^{1/2}$.

Even at rock sites, the site response plays an important role in the shape of the source spectra (e.g. Frankel, 1982; Anderson and Hough, 1984; Singh et al., 1988). When the site effect is common to all sites, it becomes difficult to distinguish between source and site effect. In our approach, which is similar to Andrews (1986), all systematic effects are assigned to the source by requiring that the geometrical average of the site effect over all sites is unity. Tucker et al., (1984) observed that typical rock sites amplify or deamplify the amplitudes of incident motion depending upon the azimuth and incidence angle of the incoming signal. Ideally, using events at different azimuths and distances, on the average these effects cancel out.

DATA

The data set used for this study consists of 9 moderate earthquakes $4 < M < 7$ recorded by at least three stations along the subduction zone (Table 1-1). These data are described in reports by Anderson et al. (1987,1988,1989). Figure 1-1 shows the location of the epicenters and the distribution of the stations of the array. The stations used for the present analysis are plotted with solid circles. The hypocentral distances range from 13 km to 133 km and as shown in Figure 1-2, most of the stations are at distances $r > 30$ km. All the instruments have a clock that is synchronized to Universal Time by Omega navigation signals. The events were located using P and S arrivals of the array and local seismological networks, as described by Anderson et al. (1988). The locations shown in Table 1-1 have an estimated error of about ± 5 km (on the average, the horizontal and vertical errors as given by the program HYPOINV are 2.7 km and 2.4 km respectively).

TABLE 1-1

Events used in this study

No.	Date	Lat N	Lon W	H	H (PDE)	M_{II}^1	m_b	M_s
1	Feb 18, 86	17.009	99.209	31.2		4.0		
2	May 29, 86	16.851	98.932	35.6	36.4	5.0	5.2	4.2
3	Jun 16, 86	17.076	99.621	33.8		4.3	4.5	
4	Apr 02, 87	16.839	99.694	18.0		4.0	4.8	
5	Jun 07, 87	16.654	98.909	22.9	40.6	4.9	5.5	4.8
6	Jun 09, 87	16.943	99.844	29.7		4.0	4.2	
7	Feb 08, 88	17.500	101.140	19.7	58.0	5.0	5.5	5.8
8	Aug 16, 88	17.034	99.834	12.5		4.6	4.2	
9	Apr 25, 89	16.579	99.462	17.3	33.0		6.3	6.9

¹ M_{II} is assigned by the Instituto de Ingenieria, UNAM, based on coda duration on short period vertical seismometers.

GUERRERO ACCELEROGRAPH ARRAY

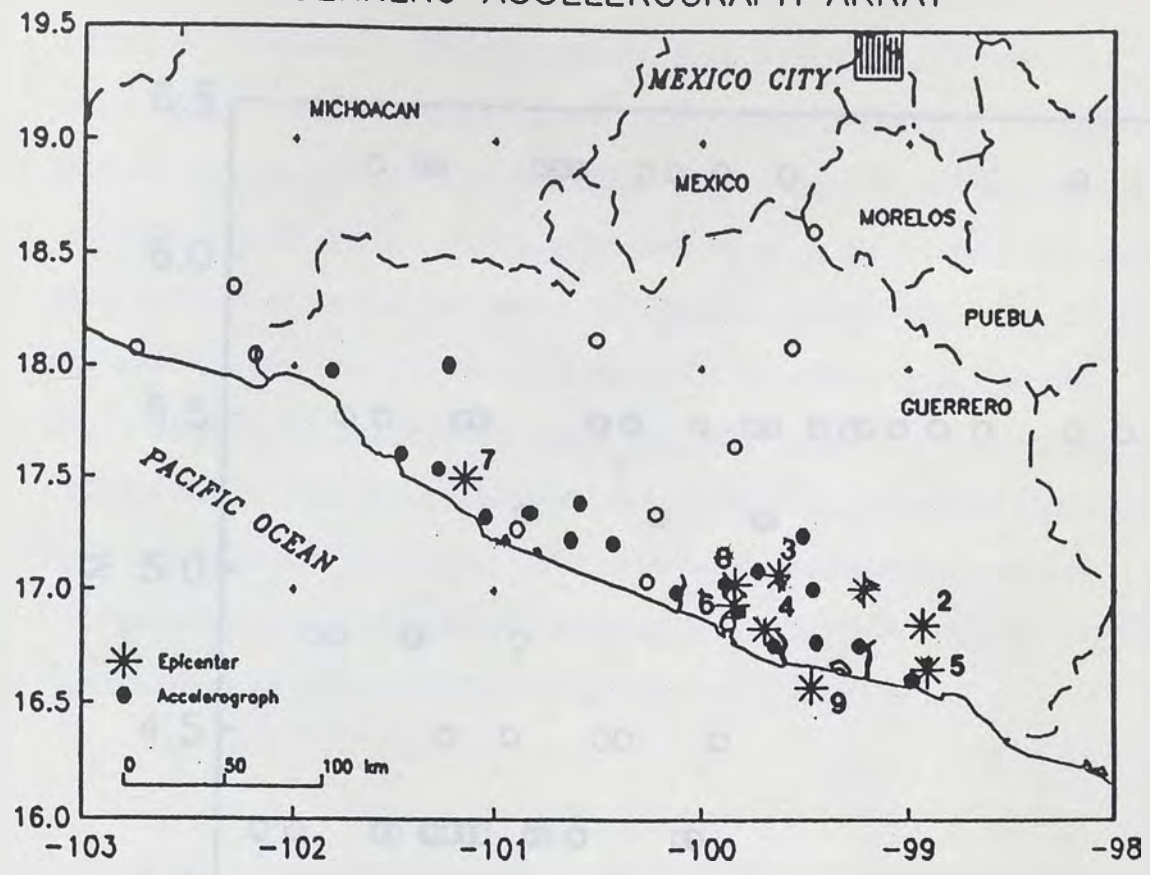


Figure 1-1. Epicenters and station locations. Only stations with solid circles were used.

Singh et al. (1988) observed that stations inland from the coast are characterized by anomalous amplification. Such effects could result from wave propagation phenomena associated with the dipping slab or geological differences among the sites. Inland stations usually have to be sited on the andesites of the trans-Mexican volcanic belt, while stations on the coast are most often sited on plutons. We decided to limit our study of attenuation to source - station paths which lie within the vicinity of the Pacific coast. On this basis, records from the stations Teacalco, Tonalapa, Filo de Caballo and La Comunidad (see Table 1-2) were removed for this study. The station El Paraiso (PARS) was also not used because those accelerograms appear to resonate at 10 Hz. Consequently the peak accelerations from this station are usually higher than the maximum acceleration recorded at other sites at comparable distances. For the April 25, 1989 earthquake, for instance, the peak acceleration at PARS is about four times higher than that for stations El Cayaco, Filo de Caballo and Atoyac (Figure 1-1).

TABLE 1-2

Stations used in this study

Station	Code	Lat °N	Lon °W	Ko sec	Events
Atoyac	ATYC	17.211	100.433	0.0218	7,9
Cerro de Piedra	CPDR	16.761	99.644	0.0453	2,3,4,5,6,8,9
Copala	COPL	16.610	98.980	0.0369	9
Coyuca	COYC	16.995	100.120	0.0498	3,4,5,6,7,9
El Balcon	BALC	18.009	101.222	0.0109	7
La Llave	LLAV	17.344	100.830	0.0416	7
La Union	UNIO	17.980	101.810	0.0273	7
La Venta	VNTA	16.913	99.819	0.0247	4,6,8,9
Las Mesas	MSAS	17.008	99.457	0.0240	1,2,3,5,6,9
Las Vigas	VIGA	16.758	99.230	0.0192	1,2,3,5,6,8,9
Los Magueyes	MAGY	17.387	100.594	0.0143	7
Ocotillo	OCLL	17.036	99.880	0.0258	4,5,6,8,9
Ocotito	OCTT	17.246	99.507	0.0365	1,2,5,6,8,9
Papanao	PAPN	17.325	101.039	0.0167	7
Petatlan	PETA	17.539	101.272	0.0246	7
San Marcos	SMR2	16.772	99.439	0.0221	5,8,9
Suchil	SUCH	17.224	100.639	0.0293	7
Xaltianguis	XALT	17.091	99.726	0.0251	4,5,6,8,9
Zihuatanejo	AZIH	17.608	101.462	0.0355	7

The accelerograms were base-line corrected by subtraction of the average of all the points of the time series. For each horizontal component the Fourier transform of the shear wave group of arrivals was computed. The initial time of the S-wave window was selected visually and the final time was selected automatically where the energy reaches 95% of the total. As described below, we initially analyze how the amplitudes decay with distance for different frequencies. For simplicity, we selected 26 spectral amplitudes in the frequency band $0.1 < f < 40$ Hz. To make these amplitudes as representative as possible of the average around the selected frequency, the use of smoothed spectra is preferable. The spectra were smoothed using a variable frequency band of $\pm 25\%$ of the central frequency. This algorithm has the property of conserving the total energy. Because in some cases the spectral amplitude of one of the components reaches the noise level before the other, each horizontal component was considered an independent measurement instead of using the average. For some frequencies only the amplitude of one of the components was used.

Figure 1-3 shows an example of one of the accelerograms used, the window selected and the corresponding spectrum. Some records are contaminated by noise at high and/or low frequencies. Spectra likely to be contaminated were removed by two techniques. First, we visually selected spectral windows for which the amplitudes appeared to exceed the noise. At low frequencies, we did not use the spectral amplitudes that tend to increase towards the low frequencies. For the record on Figure 1-3, for example, spectral amplitudes for frequencies less than 0.6 Hz were not used. Second, minimum spectral amplitudes were defined from instrumental characteristics, and frequencies with spectral amplitudes below this minimum (0.1 cm/sec) were excluded.

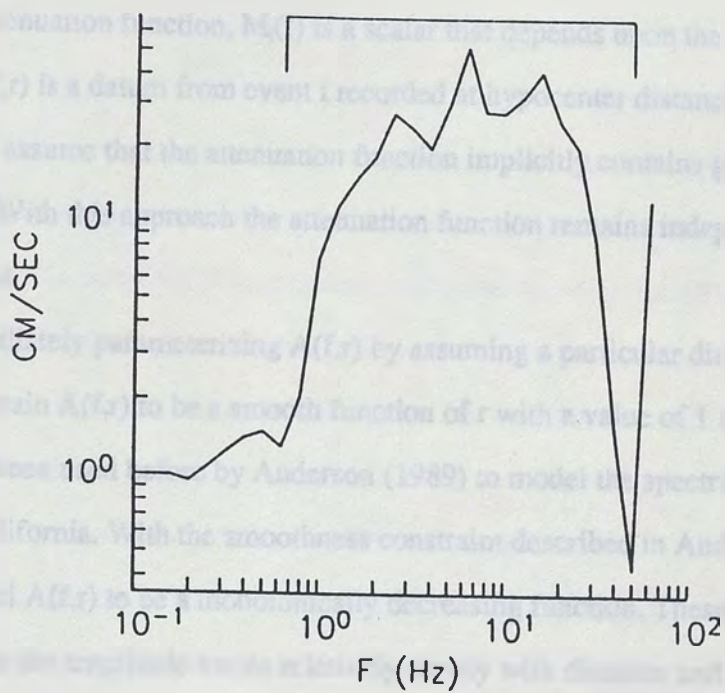
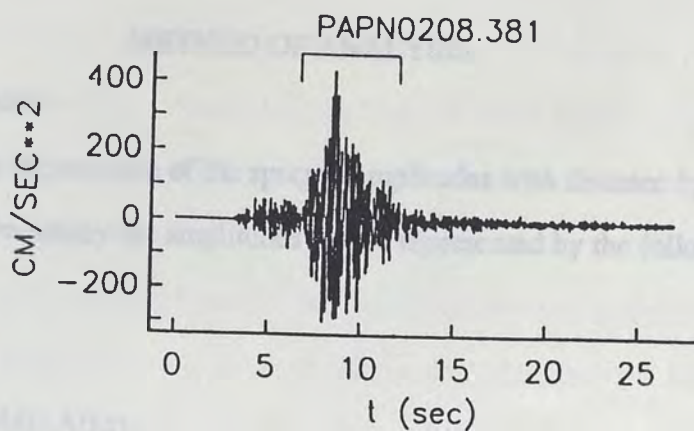


Figure 1-3. Accelerogram recorded at Papanoa and smoothed spectra. On top of the records the window selected for the analysis is also plotted.

METHOD OF ANALYSIS

Attenuation Functions

We explore the dependence of the spectral amplitudes with distance by considering that for a fixed frequency the amplitudes can be represented by the following model:

$$D_i(f,r) = M_i(f) A(f,r) \quad (1-1)$$

where $A(f,r)$ is the attenuation function, $M_i(f)$ is a scalar that depends upon the size of the i^{th} source and $D_i(f,r)$ is a datum from event i recorded at hypocenter distance r and frequency f . Here we assume that the attenuation function implicitly contains geometrical spreading and Q . With this approach the attenuation function remains independent of the size of the event.

Instead of immediately parameterizing $A(f,r)$ by assuming a particular distance dependence, we constrain $A(f,r)$ to be a smooth function of r with a value of 1 at $r=0$. A similar approach has been used before by Anderson (1989) to model the spectral attenuation in Southern California. With the smoothness constraint described in Anderson (1989), we also compel $A(f,r)$ to be a monotonically decreasing function. These constraints require that the amplitude varies relatively slowly with distance and are based on the idea that the inelastic properties in the crust tend to decrease the amplitudes with distance and that undulations may be related to other factors such as site conditions and wave propagation effects.

A least square inversion was used to solve (1) for each of the 26 frequencies selected (see Appendix). The result was a discretized attenuation function and a scaling factor M_i for each event.

Figure 1-4a shows the values of $\text{Log } D_i(f,r)$ (Equation 1-1) obtained for 0.5 Hz and all nine events in the study. The attenuation function shifts with the size of the event. In Figures 1-4b and 1-4c we plot $A(f,r)$ for 8 frequencies and the geometrical spreading functions $G(r)=(30/r)^{1/2}$ and $G(r)=30/r$. The attenuation functions $A(f,r)$ in Figure 1-4c were normalized to 30 km dividing $A(f,r)$ by the value of the function at 30 km for the corresponding frequency. Since the functions $A(f,r)$ carry the attenuation due to geometrical spreading and the attenuation due to Q , we expect $A(f,r)$ to decay faster than $G(r)$. Between 1 and 5 Hz, the slope of $A(f,r)$ is only slightly bigger than $G(r)=30/r$ indicating either a high value of Q or a less severe geometrical spreading function.

A comparison between the observed spectral amplitudes for event 9 (Table 1-1) and the amplitudes predicted by the inversion is displayed in Figure 1-5. Since the shape of the attenuation function $A(f,r)$ was constrained to be the same for all the events, the functions shown in Figure 1-5 represent the best fit in the least square sense, of all the events. Thus the function shown in this Figure not only has to match the trend of the data for this particular event, but the amplitudes and trends of the other 8 events as well. Relaxing the smoothness constraint would allow more structure in $A(f,r)$. From Figure 1-5, we conclude that the scatter in the data are great enough that less smoothing applied to $A(f,r)$ would not be justified.

The attenuation function obtained at 40 Hz is the least reliable because the spectral amplitudes at this frequency reach values close to the noise level (0.1 cm/sec). We also calculated the attenuation functions defining the noise level at 0.15 cm/sec, and found only small variation at frequencies lower than 40 Hz. The scatter of the observed spectral amplitudes can be attributed to site effects and to unmodeled radiation pattern and wave propagation effects. Because these curves made no assumption about the character of wave propagation, the contribution from wave propagation ought to be small, although some contribution could result from the smoothing applied to the atten-

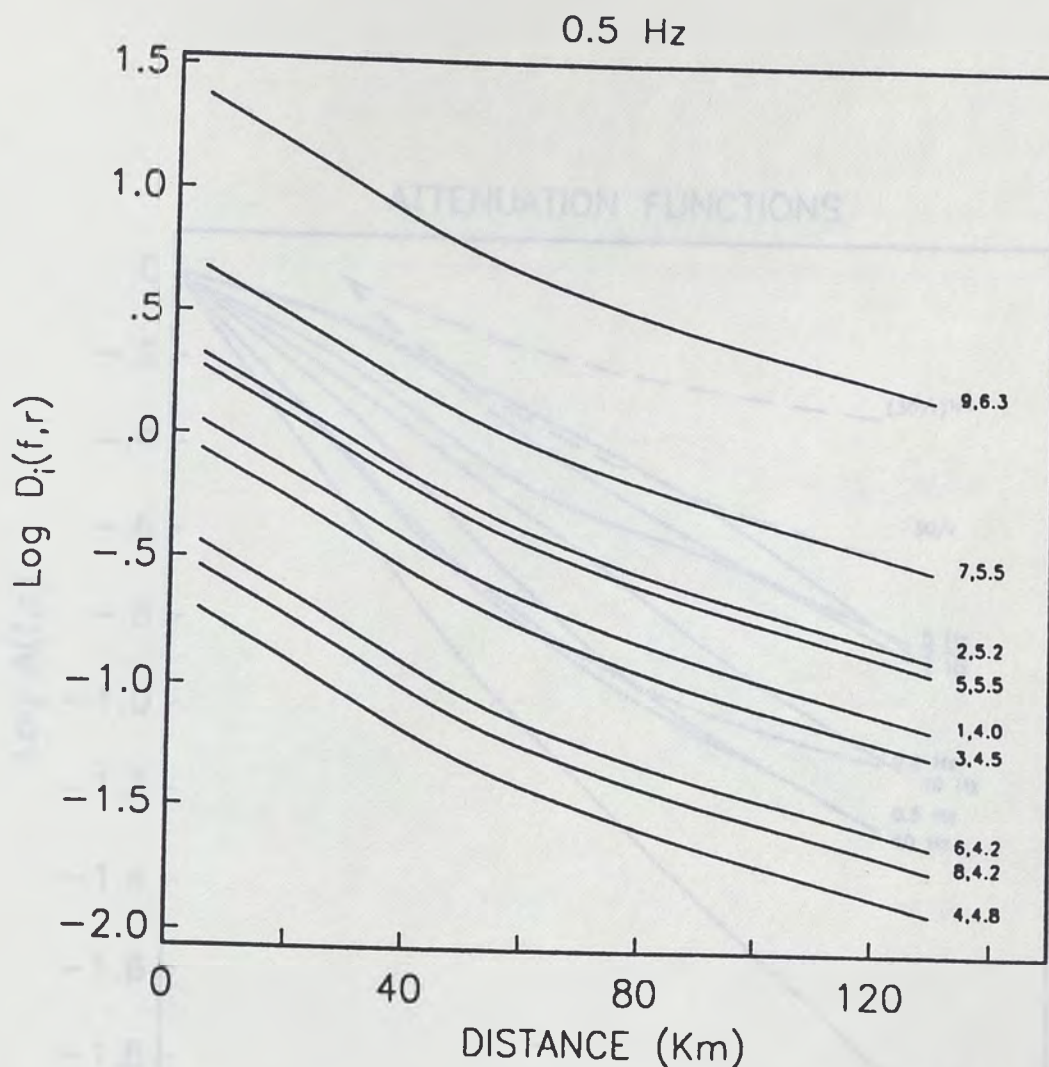


Figure 1-4a.

Spectral amplitude curves obtained using Equation (1) at 0.5 Hz for the 9 events analyzed. The first number to the right of each function refers to the event number and the second to the magnitude (M_H for event 1 and m_b for the rest).

Figure 1-4b.

obtained (Equation (1)) for 8 of the 26 frequencies analyzed. The geometrical spreading functions used to estimate Q are also shown. The dashed line on top correspond to $G(r) = (R/r)^{0.4}$ and the dashed line below to $Q(r) = 30/r$.

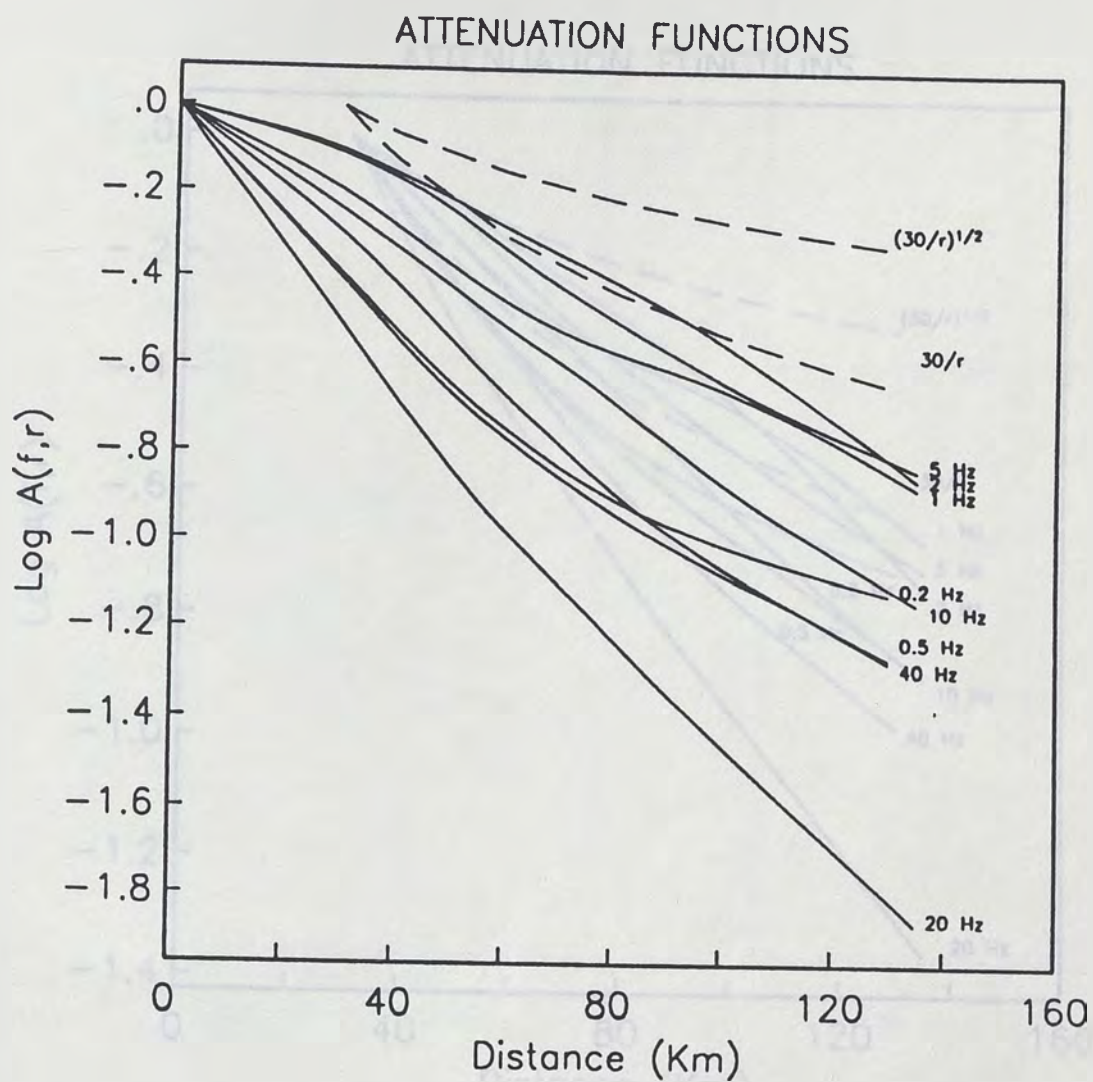


Figure 1-4b.

Attenuation functions $A(f,r)$ obtained (Equation (1)) for 8 of the 26 frequencies analyzed. The geometrical spreading functions used to estimate Q are also shown. The dashed line on top correspond to $G(r)=(30/r)^{1/2}$ and the dashed line below to $G(r)=30/r$.

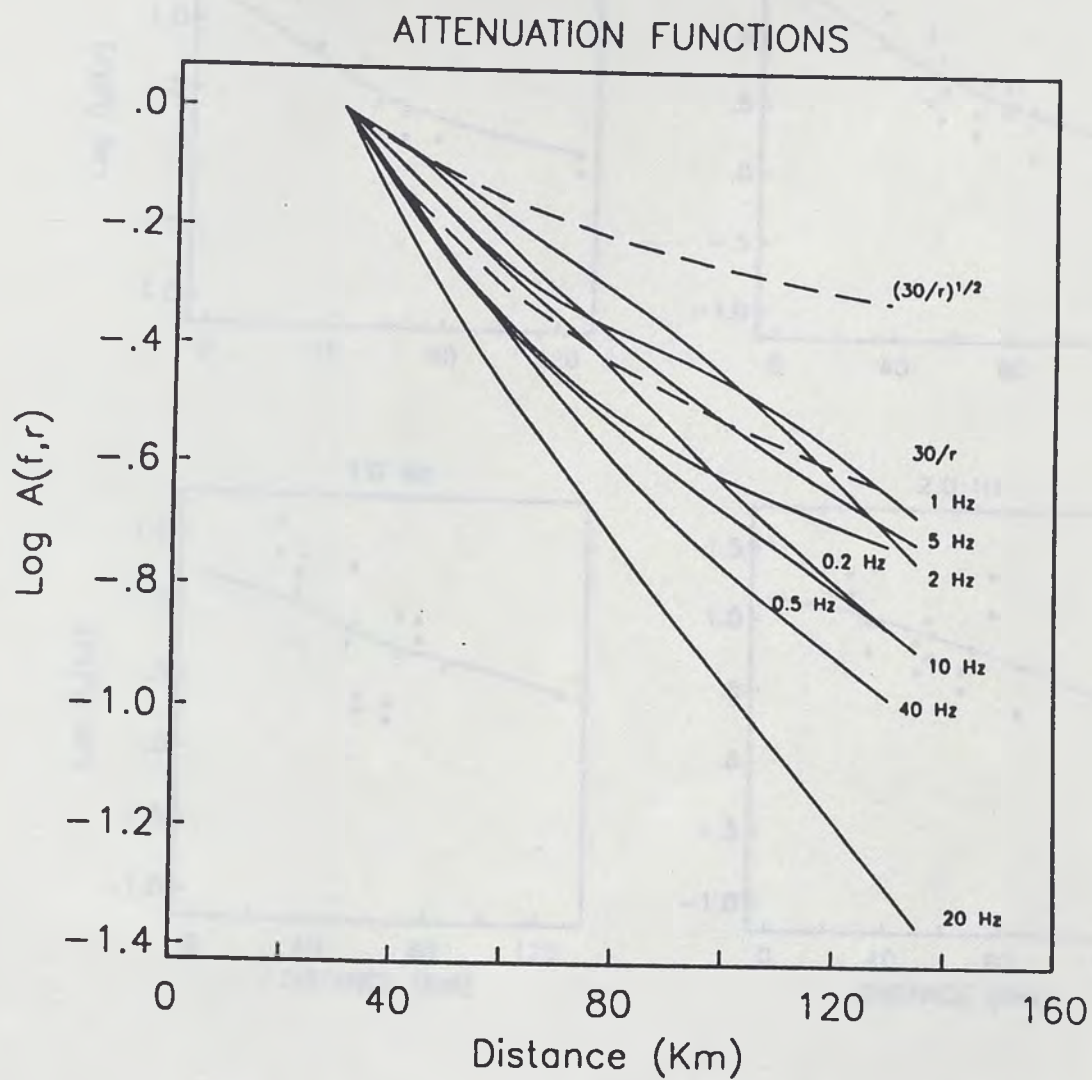


Figure 1-4c. Same as 4b but normalized to 30 km.

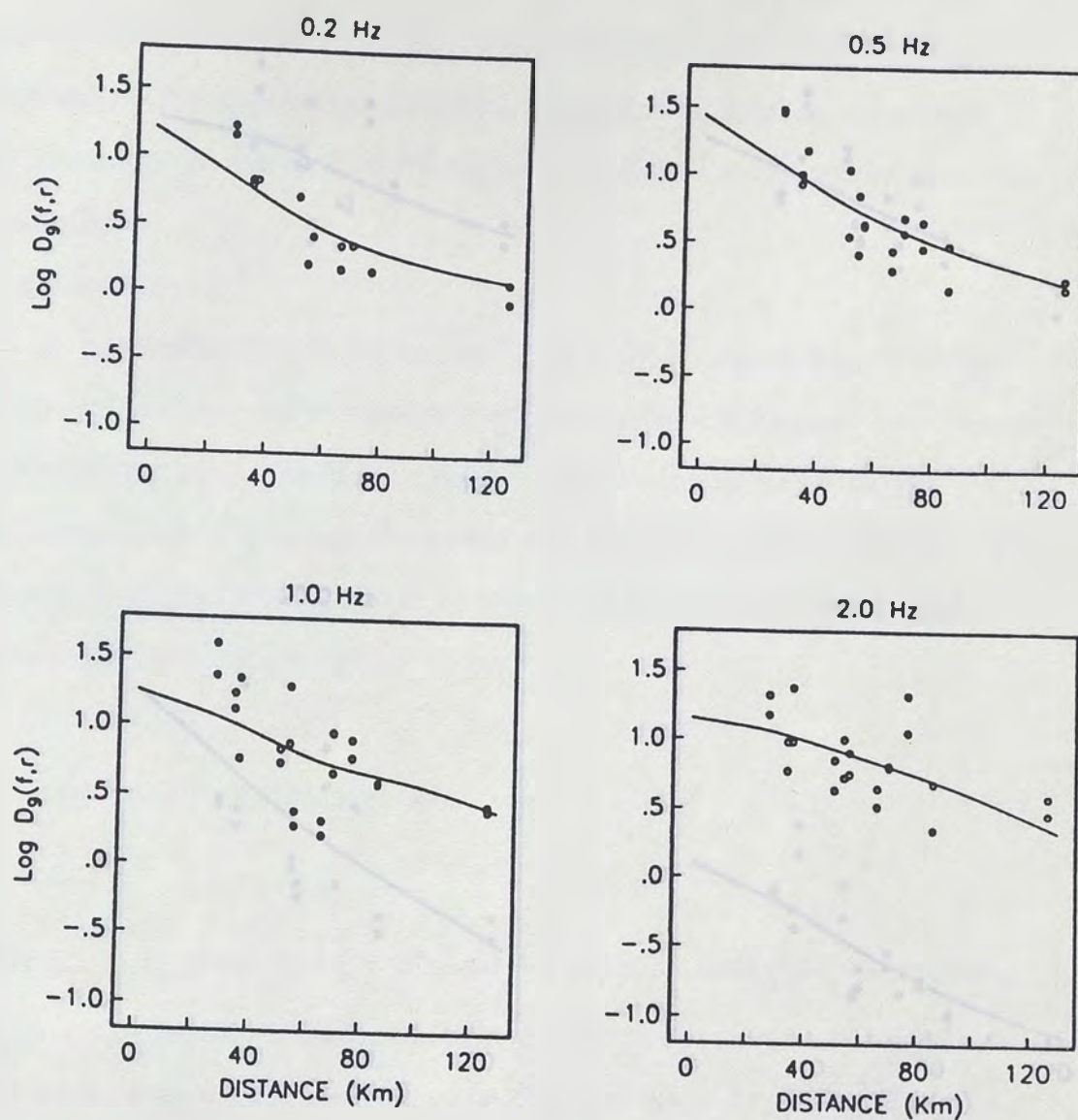


Figure 1-5. Open circles are spectral amplitudes recorded for the April 25, 1989 event ($M_s=6.9$) and the solid lines the amplitude functions obtained using Equation 1.

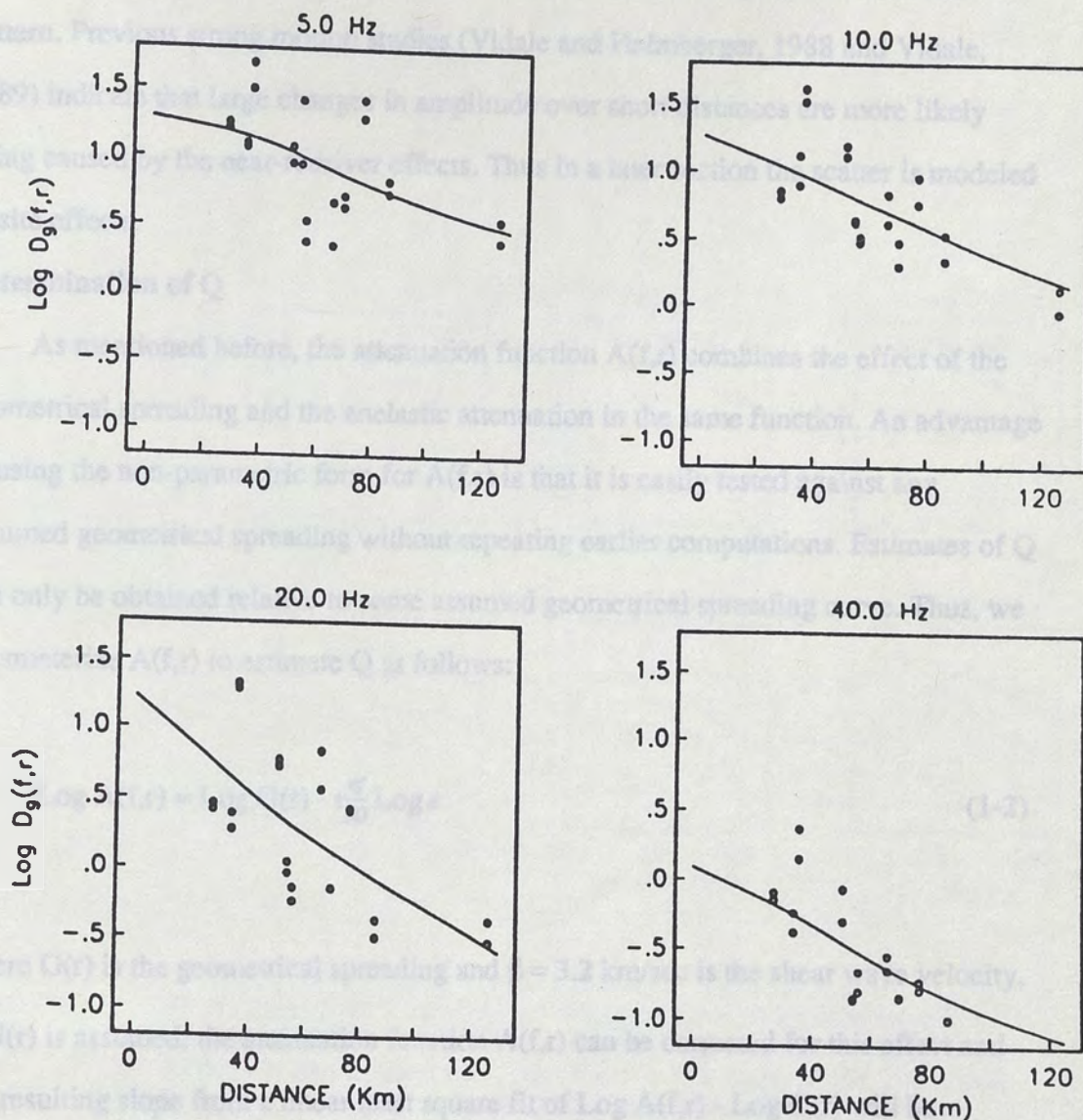


Figure 1-5. Open circles are spectral amplitudes recorded for the April 25, 1989 event ($M_s=6.9$) and the solid lines the amplitude functions obtained using Equation 1.

uation function and some could result from lateral heterogeneity. In the next section we will show that at high frequencies the scattering tends to average out the radiation pattern. Previous strong motion studies (Vidale and Helmberger, 1988 and Vidale, 1989) indicate that large changes in amplitude over short distances are more likely being caused by the near-receiver effects. Thus in a later section the scatter is modeled as site effects.

Determination of Q

As mentioned before, the attenuation function $A(f,r)$ combines the effect of the geometrical spreading and the anelastic attenuation in the same function. An advantage of using the non-parametric form for $A(f,r)$ is that it is easily tested against any assumed geometrical spreading without repeating earlier computations. Estimates of Q can only be obtained relative to some assumed geometrical spreading curve. Thus, we parameterize $A(f,r)$ to estimate Q as follows:

$$\text{Log } A(f,r) = \text{Log } G(r) - \frac{\pi f}{\beta Q} \text{Log } e \quad (1-2)$$

where $G(r)$ is the geometrical spreading and $\beta = 3.2$ km/sec is the shear wave velocity. If $G(r)$ is assumed, the attenuation function $A(f,r)$ can be corrected for this effect and the resulting slope from a linear least square fit of $\text{Log } A(f,r) - \text{Log } G(r)$ will be proportional to f/Q . Because most of the stations recorded events at distances $r > 30$ km, we normalize $A(f,r)$ to 30 km. Figure 1-6 shows the attenuation functions corrected by geometrical spreading and the regression used to estimate Q. At low frequencies ($f < 0.5$ Hz) the number of data points used to derive the attenuation functions is smaller than it is at higher frequencies and consequently the uncertainties are bigger. In Figure

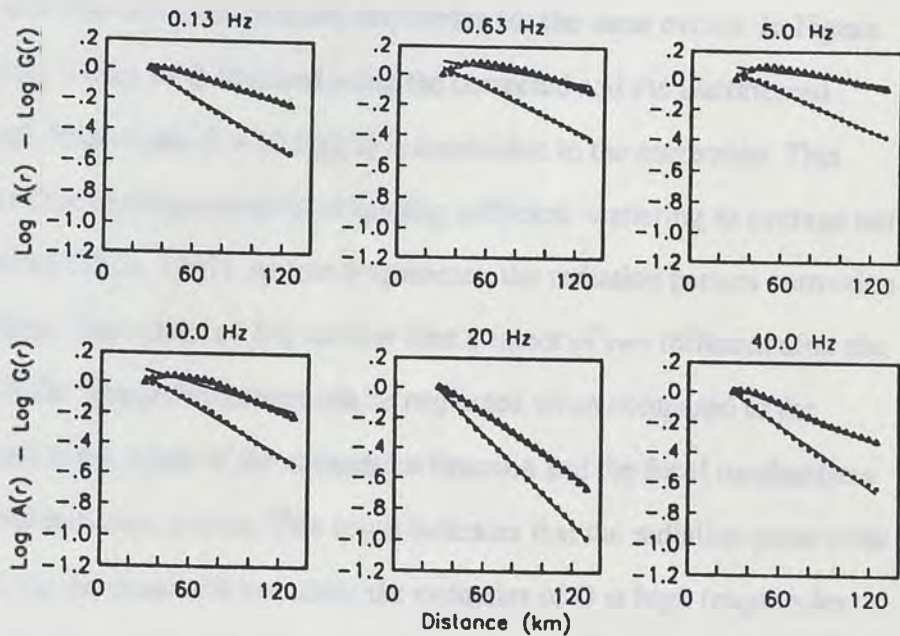


Figure 1-6. Attenuation functions obtained using the non-parametric model (Equation 1) after the geometrical spreading correction. Triangles for $G(r)=30/r$ and squares for $G(r)=(30/r)^{1/2}$. The slope of the regression lines shown are proportional to $1/Q$ (see Equation (2)).

geometrical spreading for that frequency band.

To test possible variations of Q due to radiation pattern, we used four of the biggest earthquakes (events 2,5,7,9 in Table 1-1) for which the focal mechanism was reported by the PDE, and calculate the S-wave far-field radiation pattern (see Aki and Richards, 1980 p.115) for each of the stations that recorded these events. We calculate Q for $G(r)=30/r$ as described previously, using spectral amplitudes corrected by the radiation pattern and also using uncorrected amplitudes for the same events. In Figure 1-7c we compare the values of Q obtained using the corrected and the uncorrected amplitudes. At high frequencies ($f > 10$ Hz), Q is insensitive to the correction. This may be the result of the heterogeneous crust causing sufficient scattering to average out the radiation pattern (Vidale, 1989). At low frequencies, the radiation pattern correction has a moderate effect. The values of $1/Q$ are less than a factor of two different after the correction for $f < 6$ Hz. These differences can be neglected when compared to the uncertainties related to the shape of the attenuation function and the focal mechanisms used to calculate the radiation pattern. This result indicates that the radiation pattern for events recorded along the coast will not affect the estimates of Q at high frequencies. Thus, remaining calculations do not utilize any radiation pattern correction.

In another set of calculations, we evaluated the effect of near surface attenuation (e.g. Singh et al., 1982; Anderson and Hough, 1984). Anderson and Hough (1984) described the trend of the spectrum at high frequencies by the exponential form $\exp(-\pi\kappa f)$. They associate κ_0 , the value of κ found for events recorded at short distances, with near surface attenuation at the site. We used observations of κ reported by Anguiano (1989) from the sites of the Guerrero Accelerograph Array and estimated values of κ_0 for each station with the method described in Anderson (1989). Table 1-2 lists the values of κ_0 obtained. We correct all spectral amplitudes for the attenuation near the surface with this assumed exponential form. With the corrected amplitudes, we recalculated $A(f,r)$ and Q as before. Figure 1-7d shows the values of Q obtained

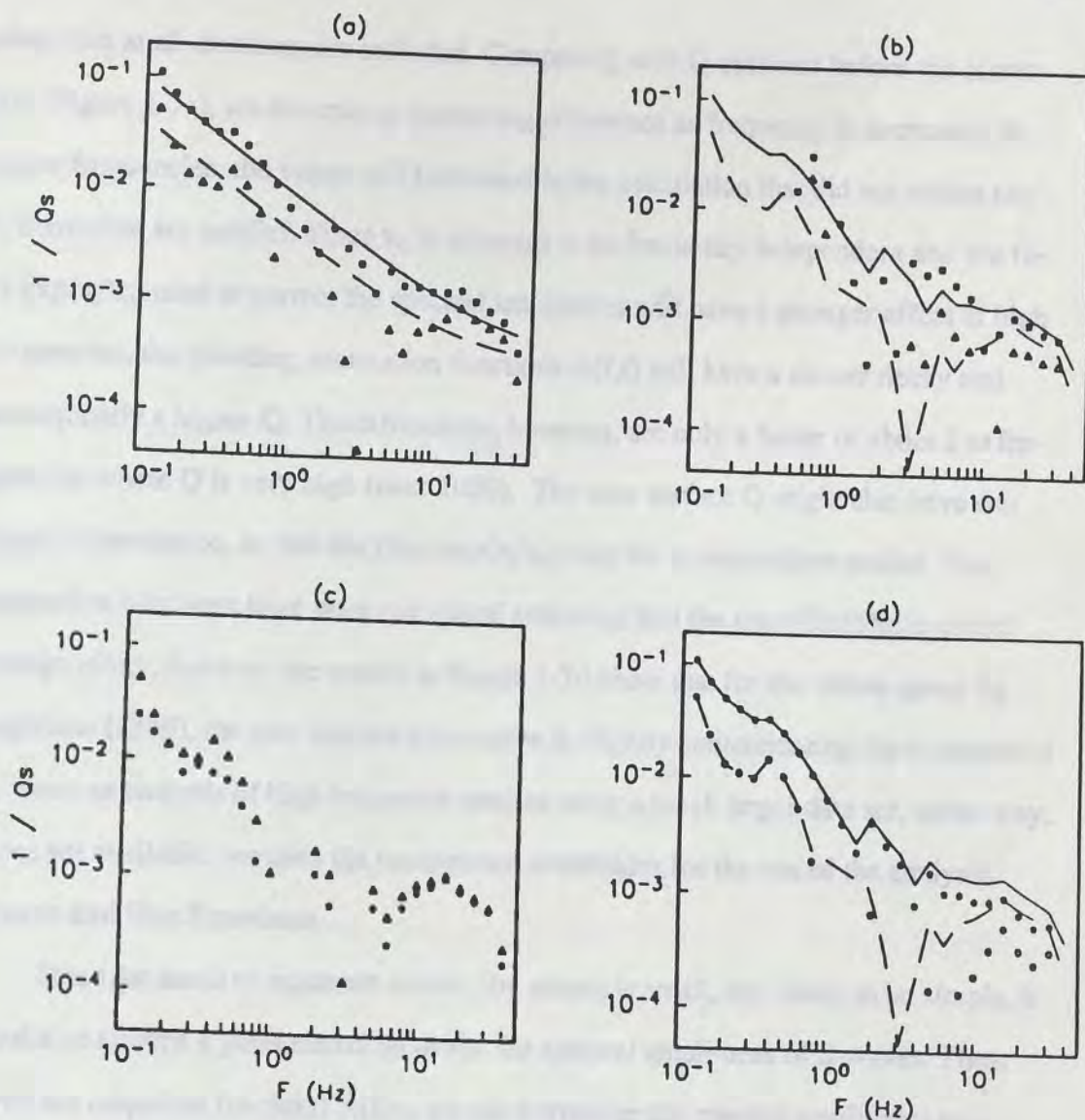


Figure 1-7. $1/Q$ estimates. (a) Using the non-parametric attenuation functions $A(f,r)$ (Equation (1)). Squares for $G(r)=(30/r)^{1/2}$ and triangles for $G(r)=30/r$. Straight lines are a fit of the form $1/Q = c + d/f$ (see Table 1-4). Solid line for $G(r)=(30/r)^{1/2}$ and dashed line for $G(r)=30/r$. (b) Using the parametric model (Equation 6). Squares for $G(r)=(30/r)^{1/2}$ and triangles for $G(r)=30/r$. For comparison we also plot the values of Q displayed on (a), solid line for $G(r)=(30/r)^{1/2}$ and dashed line for $G(r)=30/r$. (c) Effect of the radiation pattern. Filled circles after correction and triangles without correction. (d) Effect of the near source attenuation factor κ_0 . Filled circles for $G(r)=(30/r)^{1/2}$ and empty circles for $G(r)=30/r$ after the κ_0 correction. The lines shown are the values of $1/Q$ displayed on (a).

when data at all distances are included. Comparing with Q obtained before the correction (Figure 1-7a), we observe an increasing difference as frequency is increased. At higher frequencies, the values of Q obtained in the calculation that did not utilize any κ_0 correction are smaller. Since κ_0 is assumed to be frequency independent and the filter $\exp(\pi f \kappa_0)$ used to correct the spectral amplitudes will have a stronger effect at high frequencies, the resulting attenuation functions $A(f,r)$ will have a slower decay and consequently a higher Q . The differences, however, are only a factor of about 2 at frequencies where Q is very high (over 1000). The near surface Q might also have frequency dependence, so that the filter $\exp(\pi f \kappa_0)$ may be an incomplete model. The attenuation functions have been calculated assuming that the site effects have a zero average effect, however the results in Figure 1-7d show that for the values given by Anguiano (1989), the near surface attenuation is slightly contaminating the estimates of Q . Since an analysis of high frequency spectra using a much larger data set, under way, is not yet available, we used the uncorrected amplitudes for the rest of the analysis.

Source and Site Functions

Since for small to moderate events, the source is small, and likely to be simple, it is valid to assume a point source to model the spectral amplitudes of S-waves. Thus, given the empirical functions $A(f,r)$, we can normalize the spectral amplitudes to a common distance, at which differences in the residuals will be determined by the product of the acceleration source spectra and the site response, e.g.:

$$R_{ij}(f) = S_i(f) Z_j(f) = D_i(f,r) / A(f,r) \quad (1-3)$$

Here, $S_i(f)$ is the acceleration source function of the event i at frequency f , $Z_j(f)$ is the site response of the station j , and $R_{ij}(f)$ is the residual spectral amplitude after correction for path effect using $A(f,r)$. The average of $R_{ij}(f)$ over all stations recording the i^{th} event would yield $M_i(f)$ as defined in Equation (1-1). We assume that the site term in

Equation (1-3) carries the amplification due to low velocity layers near the surface, topographic and other three-dimensional effects, and some of the near surface attenuation. Phillips and Aki (1986) and Andrews (1986) used a similar model to separate site effects from source functions in California.

A system of linear equations can be set by rewriting (1-3):

$$\text{Log } S_i(f) + \text{Log } Z_j(f) = \text{Log } R_{ij}(f) \quad (1-4)$$

Equation (1-4) was solved for site and source for the 26 frequencies used previously. Since all the stations used in this analysis are on hard rock, we impose that the logarithmic sum of site effects in (1-4) equals zero. This condition eliminates the linear dependence in which an arbitrary function of frequency can be added to the site term and subtracted from the source term for a system without the constraint. The term $S_i(f)$ will differ from $M_i(f)$ (Equation (1-1)) because in Equation (1-4) the average of $\text{Log } Z_j(f)$ over all stations in the array is constrained to equal zero. In contrast, in Equation (1-1) the implicit assumption is that the average of $\text{Log } Z_j(f)$ over all stations recording the i^{th} event is zero.

Figure 1-8 shows the acceleration source spectra normalized to 30 km as a function of frequency for the 9 events used. Figure 1-9 shows the site response of each station. The errors associated with this result for the different frequencies are listed in Table 1-3.

The source functions obtained can also be expressed in terms of the far-field source acceleration spectrum $f^2 \dot{M}_0(f)$ by writing (e.g. Boore, 1986):

$$S(f) = \frac{2\pi R_{ps}}{\rho\beta^3 r} f^2 \dot{M}_0(f) \quad (1-5)$$

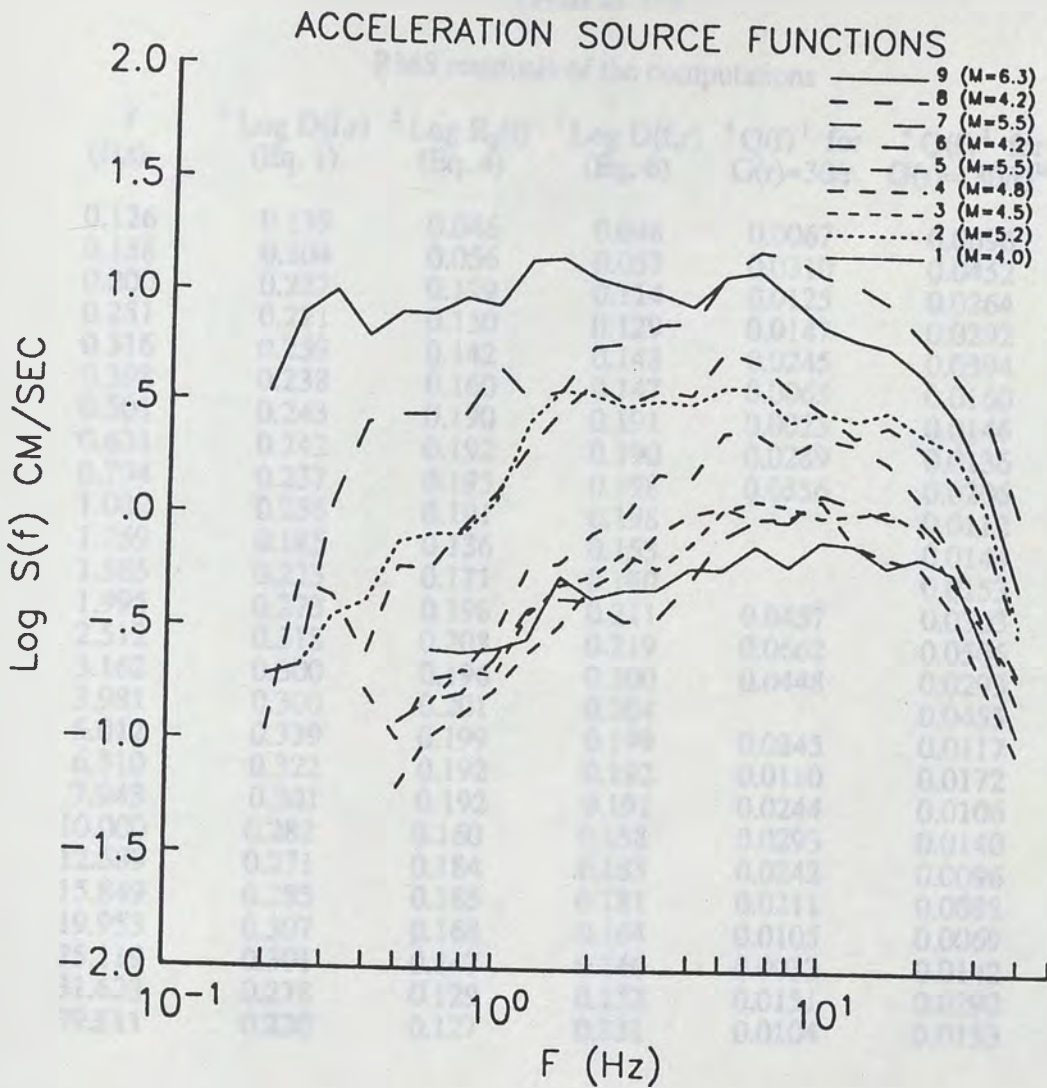


Figure 1-8. Acceleration source function normalized to 30 km using the non-parametric approach (Equation (3)).

In Figure 1-10 we plot $f^2 \dot{M}_0(f)$ with $\rho = 2.8 \text{ gm/cm}^3$, $\beta = 3.2 \text{ km/sec}$, $r=30 \text{ km}$ and average radiation pattern $R_{pr}=0.6$.

TABLE 1-3

RMS residuals of the computations

f (Hz)	¹ Log D(f,r) (Eq. 1)	² Log R _{ij} (f) (Eq. 4)	³ Log D(f,r) (Eq. 6)	⁴ Q(f) ⁻¹ for G(r)=30/r	⁴ Q(f) ⁻¹ for G(r)=(30/r) ^{1/2}
0.126	0.139	0.046	0.048	0.0067	0.0096
0.158	0.204	0.056	0.057	0.0310	0.0452
0.200	0.222	0.129	0.114	0.0125	0.0264
0.251	0.221	0.130	0.129	0.0147	0.0292
0.316	0.259	0.142	0.143	0.0245	0.0394
0.398	0.238	0.160	0.147	0.0065	0.0160
0.501	0.243	0.190	0.191	0.0023	0.0146
0.631	0.242	0.192	0.190	0.0289	0.0136
0.794	0.237	0.195	0.198	0.0356	0.0206
1.000	0.236	0.191	0.198		0.0112
1.259	0.185	0.136	0.153		0.0144
1.585	0.223	0.171	0.180		0.0153
1.995	0.273	0.198	0.211	0.0457	0.0303
2.512	0.318	0.208	0.219	0.0662	0.0506
3.162	0.300	0.196	0.200	0.0448	0.0293
3.981	0.300	0.201	0.204		0.0455
5.012	0.339	0.199	0.199	0.0245	0.0117
6.310	0.322	0.192	0.192	0.0110	0.0172
7.943	0.301	0.192	0.191	0.0244	0.0106
10.000	0.282	0.160	0.158	0.0293	0.0140
12.589	0.271	0.184	0.183	0.0242	0.0096
15.849	0.285	0.185	0.181	0.0211	0.0088
19.953	0.307	0.168	0.164	0.0105	0.0069
25.119	0.301	0.147	0.146	0.0033	0.0142
31.623	0.278	0.129	0.132	0.0151	0.0290
39.811	0.220	0.127	0.131	0.0104	0.0153

$$\text{RMS} = [1/n \sum (\text{res}_i)^2]^{1/2}$$

$$^1 \text{res}_i = \text{Log } D_i(f,r) - \text{Log } [M_i(f) A(f,r)]$$

$$^2 \text{res}_i = \text{Log } R_{ij}(f) - \text{Log } [S_i(f) Z_j(f)]$$

$$^3 \text{res}_i = \text{Log } D_{ij}(f,r) - \text{Log } [S_i(f) Z_j(f) e^{-\pi f r / \beta Q} G(r)], \text{ for } G(r)=30/r$$

$$^4 \text{res}_i = (\text{Log } A_i - \text{Log } G(r)) - r f \text{Log } e \pi / \beta Q$$

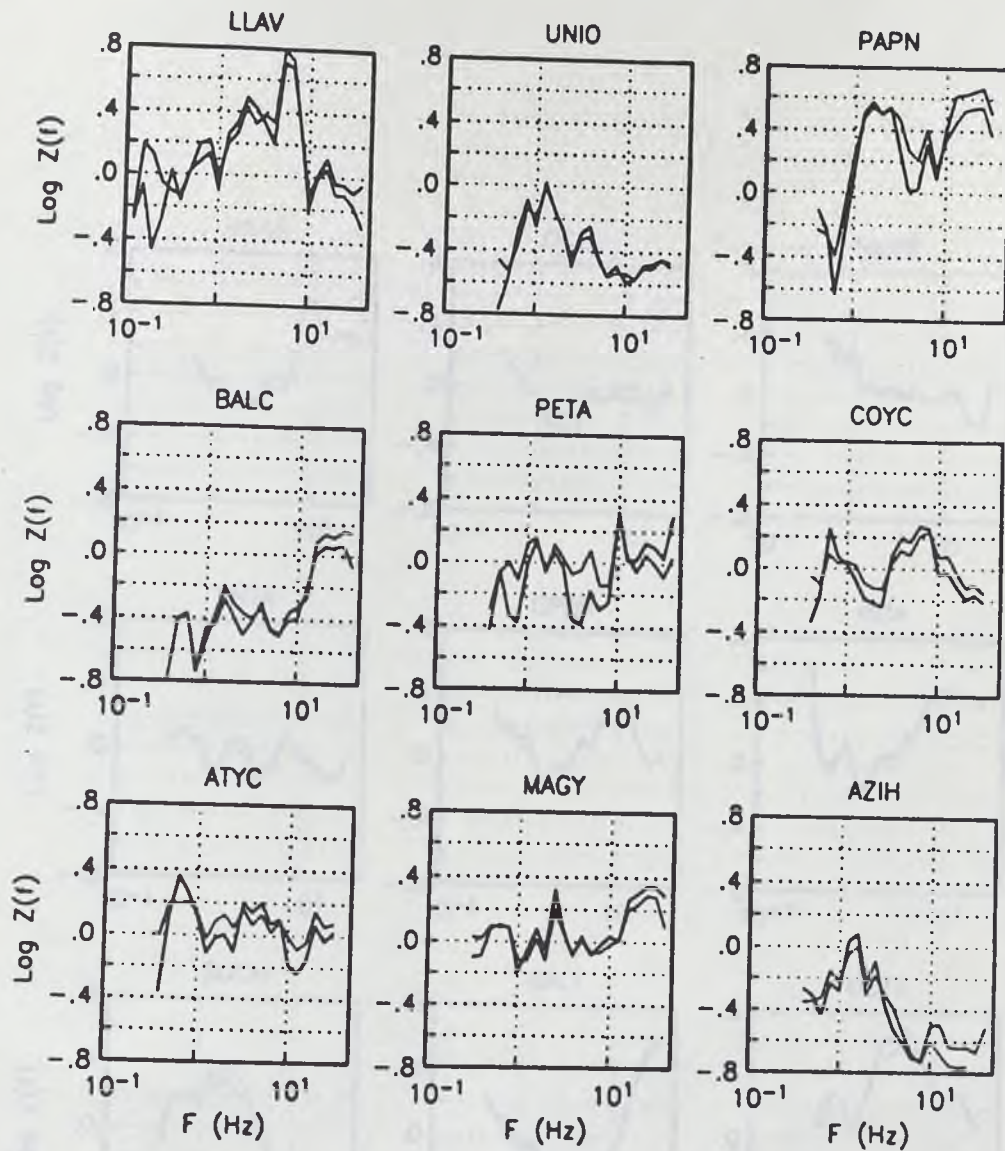


Figure 1-9.

Site response functions. Light lines for the non-parametric model after reducing the spectral amplitudes to zero distance and the solid lines for the parametric model for $G(r)=30/r$ (Equation 5).

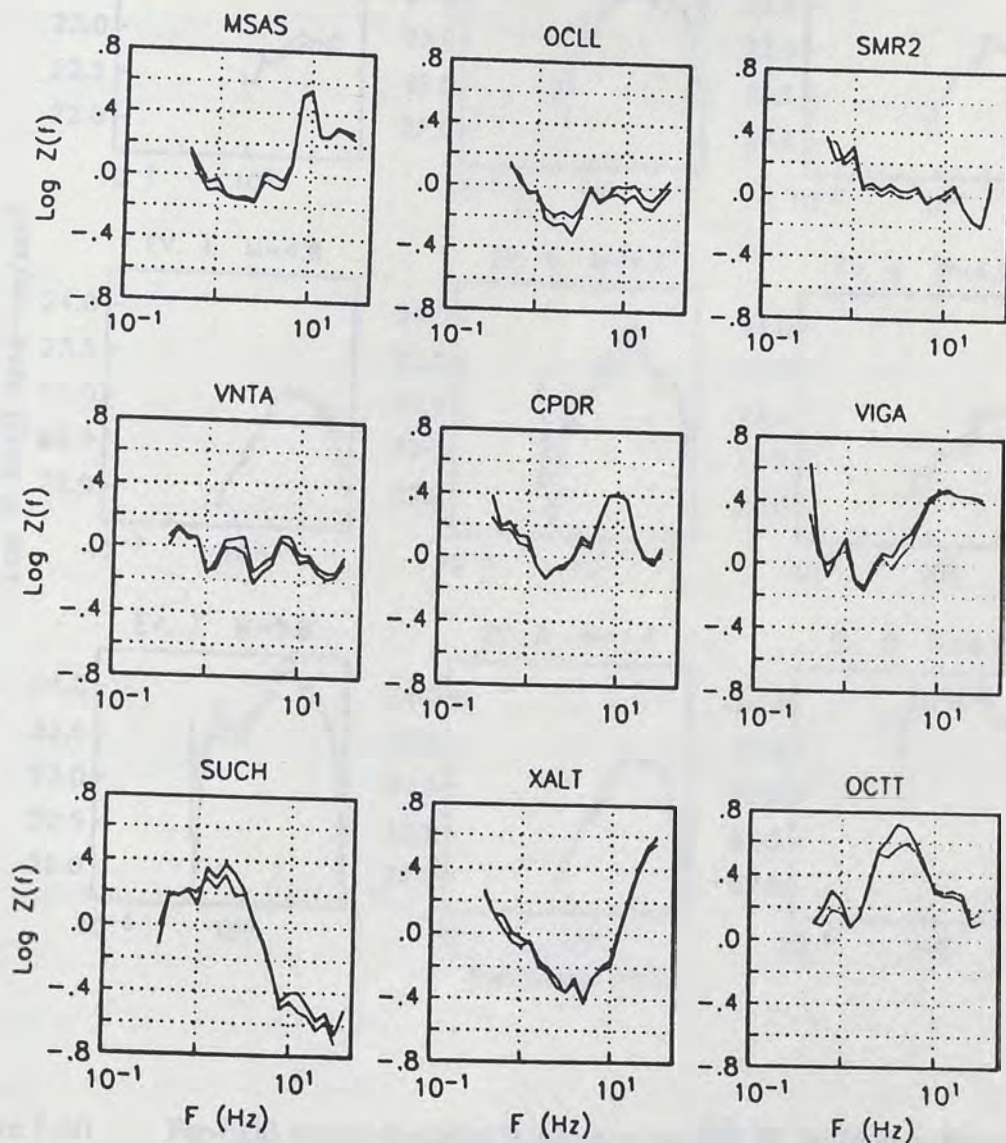


Figure 1-9.

Site response functions. Light lines for the non-parametric model after reducing the spectral amplitudes to zero distance and the solid lines for the parametric model for $G(r)=30/r$ (Equation 5).

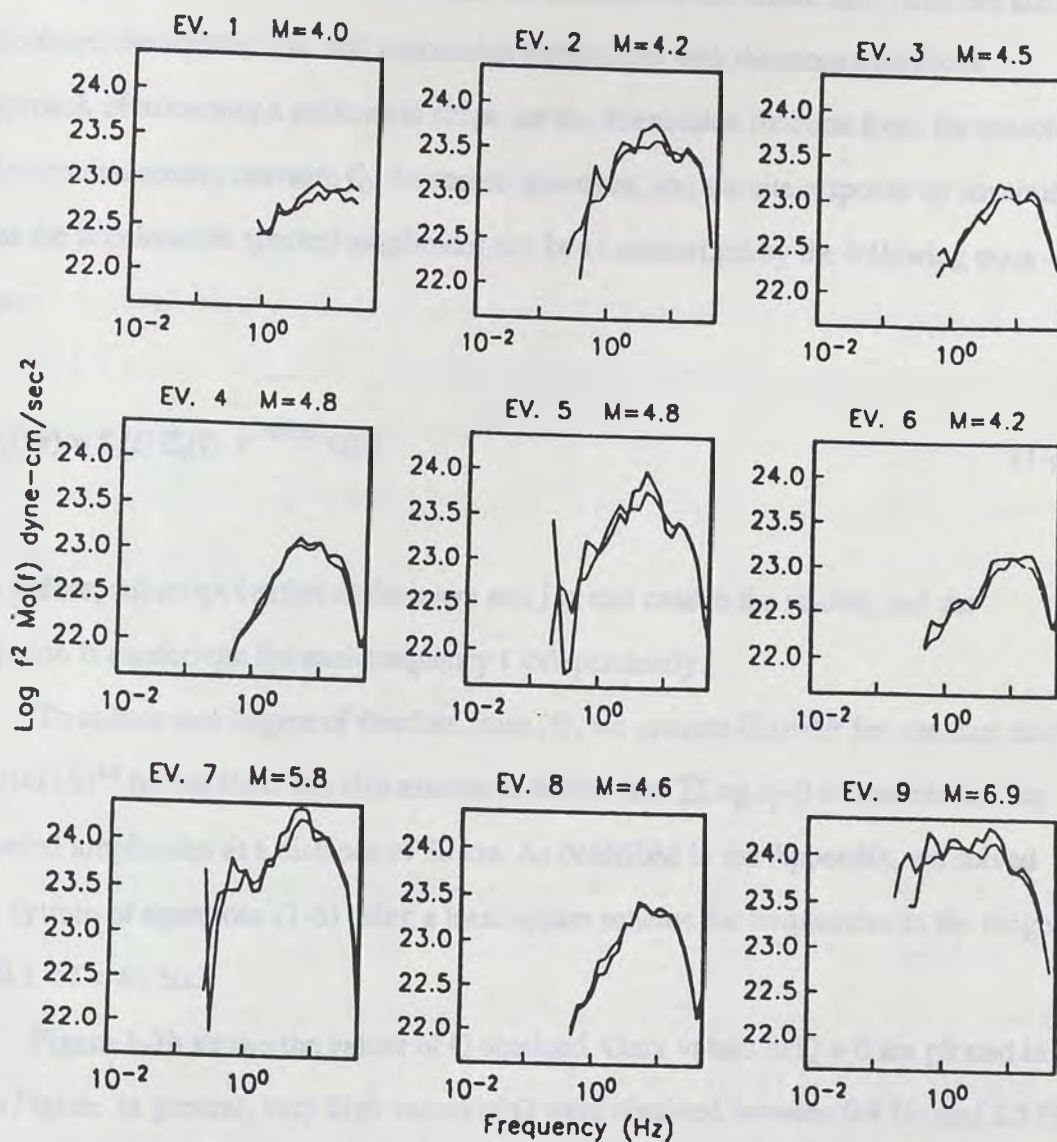


Figure 1-10. Far-field source spectrum in acceleration $f^2 M_0(f)$. Solid lines for the parametric and dotted lines for the non-parametric model.

Parametric Model

The previous non-parametric estimate for the attenuation function is experimental, and its shape depends to some extent on the smoothness constraint. Thus, we also calculated the source, site, and attenuation parameters with the more traditional approach of assuming a parametric shape for the attenuation function from the outset. We simultaneously estimate Q , the source spectrum, and the site response by assuming that the acceleration spectral amplitudes can be characterized by the following equation:

$$D_{ij}(f,r) = S_i(f) Z_j(f) e^{-\pi f r / \beta Q} G(r) \quad (1-6)$$

As before, subscript i refers to the event and j in this case to the station, and the solution is carried out for each frequency f independently.

To reduce one degree of freedom from (6), we assume $G(r)=1/r$ for one case and $G(r)=(1/r)^{1/2}$ for another. We also assume as before that $\sum \log z_j = 0$ and normalize the spectral amplitudes at a distance of 30 km. As described in the Appendix, we solved the system of equations (1-6) using a least square scheme for frequencies in the range of $0.1 < f < 40$ Hz.

Figure 1-7b shows the values of Q obtained. Only values of $Q > 0$ are plotted in this Figure. In general, very high values of Q were obtained between 0.9 Hz and 2.5 Hz regardless of the assumption of $G(r)$. For comparison, we also plot in this Figure the values of $1/Q$ computed from the non-parametric attenuation model (Figure 1-7a), continuous line for $G(r)=(30/r)^{1/2}$ and dashed line for $G(r)=30/r$. At high frequencies ($f > 8$ Hz) the parametric model predicts higher values of Q . With the assumptions of $G(r)$ made, we obtain the likely upper and lower limits of Q for the area under study. The geometrical spreading corrections used are based on numerical results obtained by

Wang and Herrmann (1980) for a layered crustal model. Their results indicate that at short epicentral distances the spectral amplitudes decay as a body wave (as $1/r$) while at greater distances the body wave arrivals combine to form surface waves and then the amplitudes decay as $(1/r)^{1/2}$. To test the possibility of a more rapid decay, we also solved (6) assuming $G(r)=(30/r)^{3/2}$ obtaining negative values of Q for all the frequencies considered except for $20 < f < 32$ where $12300 > Q > 8500$. We consider the values of Q after the $30/r$ correction a reasonable upper limit.

The acceleration source functions and the site responses are shown in Figures 1-10 and 1-9 respectively for $G(r)=30/r$. The residuals between model and observation (RMS) associated with the inversion ($\text{RMS}^2 = \|\Gamma x - d\|^2 / n$) are listed in Table 1-3. It is interesting to notice the consistency of results between the parametric and the non-parametric solutions.

DISCUSSION

Attenuation

As in previous studies of the attenuation in the Guerrero region (Rodriguez et al., 1983; Mahdyiar et al., 1986; Novelo-Casanova et al., 1985; Singh et al., 1989), we also find a frequency-dependent Q function. The lines on Figure 1-7a are the result of a least square fit of the form $1/Q = c + d/f$. The solid line on top of this Figure was obtained using the values of Q for $G(r)=(30/r)^{1/2}$ (solid squares) and the dashed line below using the values of Q for $G(r)=30/r$ (open triangles). This equation is an additive attenuation model (e.g. Rovelli, 1982; Richards and Menke, 1983; Hough et al., 1988) in which the apparent attenuation equals the sum of a Q frequency dependent function plus a frequency independent attenuation part. We also fit the values of Q shown in this Figure with an exponential function of the form $Q=af^b$. Table 1-4 lists the coefficients a to d obtained and the RMS for $1/Q$. Because for either the parametric or the non-parametric

approach we have computed individual inversions per frequency, the uncertainties in the estimated parameters are different from one frequency to another. Thus to obtain the model parameters shown in Table 1-4 we used a weighted linear regression. Each value of Q was weighted by $1/\text{err}$ where err is the sum of the variance of Q after fitting Equation (1-2) and the variance of $A(f,r)$ resulting from Equation (1-1). Based on the RMS values obtained, the estimates of Q are better fit with a model of the form $1/Q(f) = 1/3413 + 1/248f$ for $G(r)=30/r$ and $Q(f) = 96f^{0.96}$ for $G(r)=(30/r)^{1/2}$ (see Table 1-4). In general, the values of Q obtained from the non-parametric model between 0.8 and 6 Hz are higher than the values expected from either the additive or the exponential models. This suggests that $Q(f)$ in this frequency band is a more complicated function than previously thought.

TABLE 1-4

Regression parameters for $Q=af^b$ and $Q^{-1}=c+df^{-1}$

G(r)	a	b	rms	c	d	rms
$1/r$	278	0.92	0.0059	0.000293	0.004029	0.0046
$(1/r)^{1/2}$	96	0.96	0.0066	0.000347	0.009631	0.0067

Source Functions

One advantage of using the attenuation functions $A(f,r)$ (Equation (1-1) and Figure 1-4) to separate the path effect from the spectral records is that we do not have to assume any particular geometrical spreading function, since this is included in $A(f,r)$. By applying this correction, we reduced the acceleration source functions shown in Figure 1-8 to 30 km. The low frequency slopes of many of the source spectra displayed in this Figure appear to be less than ω^2 . The spectra are approximately flat for intermediate frequencies. At higher frequencies ($f > 20$ Hz), however, the source spectra obtained in this study diminish abruptly. The same result was obtained when we used

the parametric model prescribed in Equation (1-6). This departure of the source spectral amplitudes at high frequencies has been interpreted in other studies (Hanks, 1982; Anderson and Hough, 1984; Singh et al., 1989) as a site effect. An alternative explanation is that this feature of the spectra is controlled by the source (Papageorgiou and Aki, 1983a,b; Hanks, 1982; Archuleta et al., 1982).

Although some near-surface propagation effects are carried by the site term in Equations (1-3) and (1-6), probably the source term includes the array average of the near-surface attenuation, which is responsible for the rapid amplitude fall-off with frequency. When the source spectra shown in Figure 1-8 is corrected using an average $\kappa_0 = 0.02$, the abrupt high-frequency fall-off disappears. However, since both site and source terms are frequency dependent, this ambiguity may not have been resolved completely by imposing the constraint $\sum \text{Log } z_j = 0$ when we solved Equations (1-3) and (1-6).

To analyze in more detail the source spectra obtained, we converted the acceleration spectra to displacement (Figure 1-11). For the larger earthquakes (events 2, 5, 7 and 9 listed in Table 1-1) we also plot the low frequency level expected from the seismic moment, e.g.:

$$\Omega = 2R_{ps}M_0/4\pi\rho\beta^3r \quad (\text{Keilis-Borok, 1960}) \quad (1-7)$$

We used the same values for ρ , β , r and R_{ps} as above. In general the level of the displacement spectra agrees reasonably well with the low-frequency level expected from M_0 reported by PDE. The low-frequency level calculated from M_0 is slightly higher than that from the source spectra but this discrepancy is likely due to an overestimated M_0 . The focal depths used by PDE to estimate M_0 are generally deeper than the focal depths obtained after locating the events using local data (see Table 1-1).

The comparison of low-frequency levels between different data sets shown in Figure 1-11 indicates that the baseline of the source spectra was not altered by imposing the condition $\sum \text{Log } z_j = 0$ when solving Equations (1-3) and (1-6), and the possibility of a shifting of the source spectra level due to this condition must be ruled out.

It is also interesting to notice in Figure 1-11 that the amplitude decay rate changes for the different events. Events 1 and 9, the smallest and biggest events respectively, tend to decay as ω^{-2} up to about 15 Hz where as for the rest of the events, the spectral amplitudes decay abruptly. The rest of the events, having intermediate magnitudes with respect to events 1 and 9 may decay close to ω^{-1} at low frequencies. Changes in the rate of decay of spectral amplitudes for earthquakes with different moments have also been observed in other regions. Tucker and Brune, 1973 found a correlation between low stress drop events and the high-frequency fall off studying the aftershocks of the San Fernando earthquake, namely, displacement spectra with slopes of -1 at high frequencies had low stress drops. They interpreted this correlation as an evidence of a partial stress drop mechanism (Brune, 1970). Archuleta et al., 1982 also observed differences in the slope of the spectral amplitudes of earthquakes with a wide range of seismic moments in Mammoth Lakes, California. More recently Brune et al., 1986, analyzing earthquakes from the Anza, California array, also found that events with low stress drops (0.1 bar to 1.0 bar) tend to have a high-frequency spectral fall-off less steep than the events with higher stress drops.

Based on the Brune, 1970 model, we calculate the stress drop for events 2,5,7 and 9 ($\Delta\sigma = 2.5939 \times 10^{-22} M_0 f_c^3$), see Table 1-5 and Figure 1-11. The corner frequency f_c was selected as the intersection of the low frequency level calculated from M_0 and a straight line that fit the spectral roll off. The slope of this line decays as ω^{-1} for events 2 (M=4.2) and 5 (M=4.8), as $\omega^{-1.5}$ for event 7 (M=5.8) and as ω^{-2} for event 9 (M=6.9). It

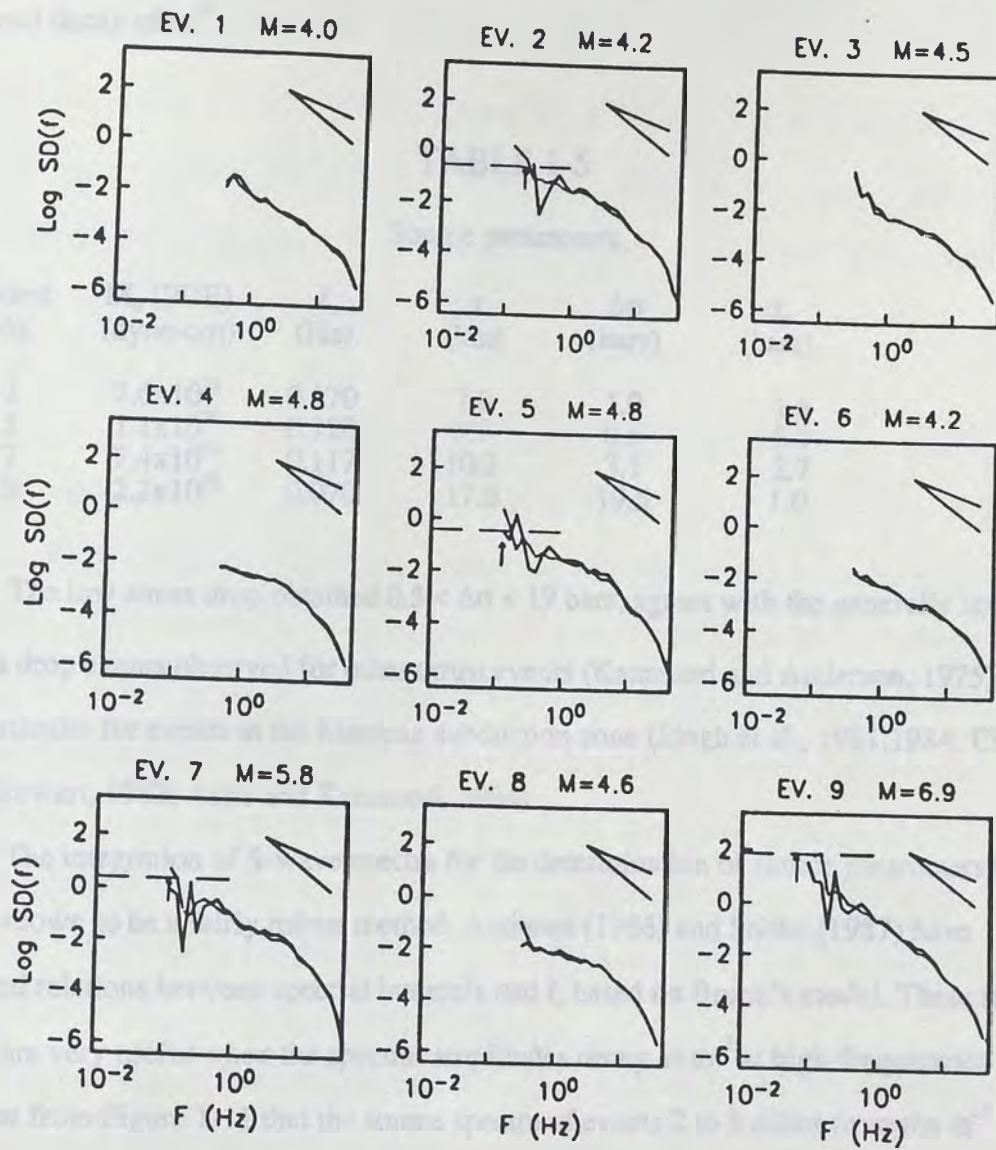


Figure 1-11. Far-field source spectrum in displacement $M_0(f)$. Solid lines for the parametric and dotted lines for the non-parametric model. The horizontal dashed line on source functions 2,5,7,9 defines the spectral level expected from the M_0 reported by PDE. The arrow indicates the point where f_c was selected.

is interesting to notice how the spectral decay seems to increase as the size of the event increases. This however does not hold for event 1, the smallest event, which has a well defined decay of ω^{-2} .

TABLE 1-5

Source parameters

Event No.	M_0 (PDE) (dyne-cm)	f_c (Hz)	r (km)	$\Delta\sigma$ (bars)	σ_a (bars)
2	7.6×10^{23}	0.170	7.0	1.0	1.5
5	1.1×10^{24}	0.120	9.9	0.5	5.1
7	7.4×10^{24}	0.117	10.2	3.1	2.7
9	2.2×10^{26}	0.070	17.0	19.5	1.0

The low stress drop obtained $0.5 < \Delta\sigma < 19$ bars, agrees with the generally low stress drop events observed for other thrust events (Kanamori and Anderson, 1975) and in particular for events in the Mexican subduction zone (Singh et al., 1981, 1984; Chael and Stewart, 1982; Astiz and Kanamori, 1984).

The integration of S-wave spectra for the determination of source parameters has been shown to be a fairly robust method. Andrews (1986) and Snoke (1987) have derived relations between spectral integrals and f_c based on Brune's model. These relations are very useful when the spectral amplitudes decay as ω^{-2} at high-frequencies. It is clear from Figure 1-11 that the source spectra of events 2 to 8 differ from the ω^{-2} decay. Because the definition of apparent stress does not require any high-frequency decay assumption, e. g.:

$$\sigma_a = \mu E_s / M_0 \quad (1-8)$$

this parameter will give a better estimate of the stress when derived from the source spectra shown in Figure 1-11.

In Equation (1-8) E_s is the seismic energy radiated as S-wave and is determined from the integration of the squared velocity spectra (Wu, 1966):

$$E_s = I\rho\beta r^2 \int V^2(f) df \quad (1-9)$$

where $I = 24\pi / 15$, $\mu = 3.3 \times 10^{11}$ dyne/cm and ρ , β , M_0 and r the same as above. Table 1-5 lists the values of σ_s obtained using (8) and (9). Although the values of apparent stress are as low as the values of $\Delta\sigma$ previously obtained, σ_s does not increase with either M_0 or the rate of high-frequency decay.

Site Response

The site functions obtained using the two approaches described in the previous sections (Equations (1-3) and (1-6)) are shown in Figure 1-9. In general, there is very good agreement between the functions obtained using the corrected spectral amplitudes (Equation (1-3)) and the site functions obtained using the parametric model (Equation (1-6)). In interpreting the site functions, it is important to keep in mind that these were obtained under the condition that for a given frequency their sum over all sites must equal zero and that we do not account for effects due to wave propagation through a possible laterally heterogeneous medium nor low-frequency radiation pattern effects. Thus the amplifications shown in Figure 1-9 may not be entirely due to changes in impedance or thickness of near-surface layers.

The character of the site responses shown suggests that in addition to the amplifications due to the low velocity layers near the surface, these functions also have information about deamplifications possibly produced near the surface. At high frequencies, this deamplification could be related to the near surface attenuation mechanism described by Anderson, 1989 but only to the extent that κ_0 for the site differs from the array average. Notice, for instance, stations UNIO and AZIH for $f > 1.5$ Hz and SUCH for $f > 6$ Hz. For other stations like PAPN and MAGY, the amplification of these sites at high frequencies seems to predominate over the near surface attenuation.

The site functions of stations UNIO, BALC and AZIH are the least reliable. Note in Figure 1-1 that these stations are located in the extreme of the array, and one source was used (event 7). Thus, estimates for their site functions do not benefit from redundant data, and are more likely than other sites to have systematic errors.

In general we can distinguish 3 groups of sites: (1) sites with maximum amplifications in a well defined frequency band such as MSAS, CPDR, SUCH, XALT, OCTT; (2) stations with small amplifications or lack of them (OCLL, UNIO, BALC, AZIH, SMR2, VNTA); and (3) sites with amplifications that ring in a wider frequency band (the rest of the stations). The maximum amplification of the first group of stations is possibly related with the natural period of resonance of the site. The stations OCTT and LLAV, are the sites with the most important amplifications. OCTT amplifying the spectral amplitudes up to about 4 times at 5 Hz and LLAV up to about 6 times at 7 Hz.

Although we do not have independent information to test the validity of the site functions obtained, we can make a consistency test by multiplying the site functions with the corresponding source and attenuation functions to estimate the spectral amplitudes at a given site. In Figure 1-12 we compared the strong motion spectra recorded at OCTT and VIGA from the May 29, 1986 ($M=4.2$) earthquake with the spectral amplitude obtained after source, attenuation and corresponding site function were multiplied. The observed spectrum is the average between the horizontal components. The calculated spectra for these stations, with high site effects, is in good agreement with the spectral amplitudes observed. This is true in general for our data set, indicating that the source, attenuation and site functions are the only factors needed to describe the main features of the observed spectra.

In view of that, we estimate the average site effects of stations El Paraiso (PARS), La Comunidad (COMD) and Filo de Caballo (FICA) which were previously excluded in the analysis. Figure 1-13 shows the site functions estimated for these stations using the non-parametric attenuation functions discussed above. The average site effect of

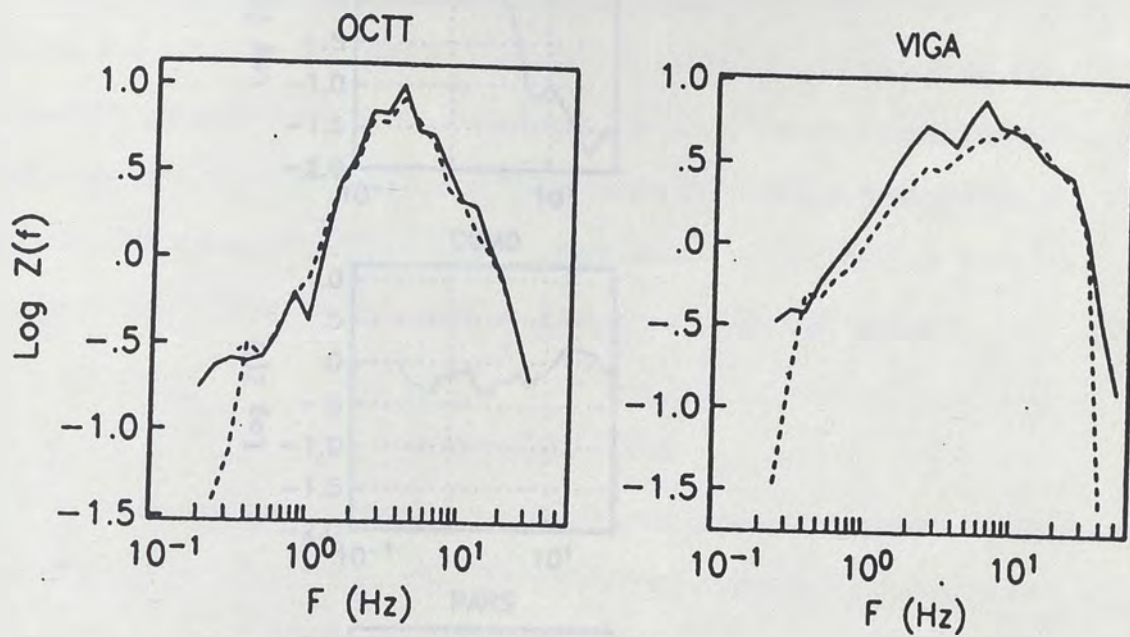


Figure 1-12. The solid lines are average spectral amplitudes observed at OCTT and VIGA from event 2 and the dashed lines the spectral amplitudes calculated multiplying source, site and attenuation functions obtained using the non-parametric approach.

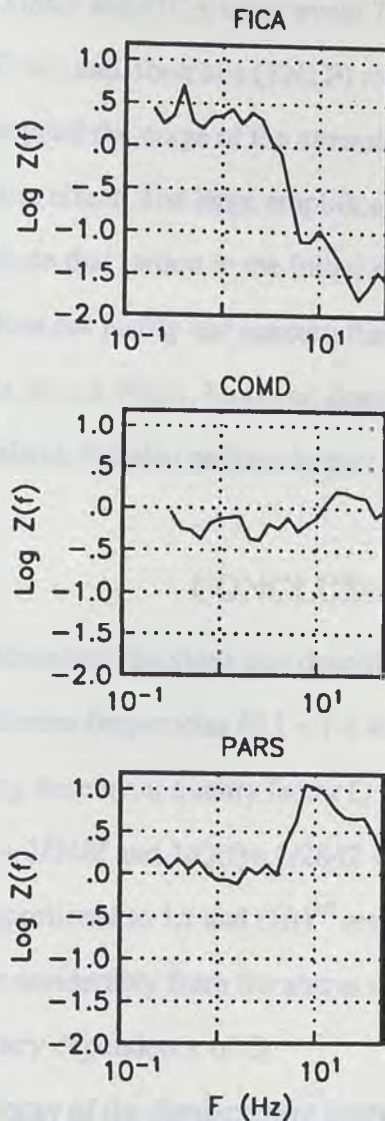


Figure 1-13. Average site effect estimated using the non-parametric attenuation functions (Equation 1) and the source functions (Equation 3) normalized to zero distance. The site function shown for PARS is the average obtained from the source functions 3, 7 and 9.

PARS was obtained using the source functions from events 3, 7, and 9 (see Table 1-1); and for stations COMD and FICA using event 7 and 9 respectively. Although the stations Teacalco (TEAC) and Tonalapa (TNLP) recorded events 7 and 9, their hypocentral distances are beyond the range of the attenuation functions, consequently we could not estimate their site effect. The large amplification at PARS at 10 Hz justifies the decision to not include that station in the initial regression. The relatively flat amplification at COMD does not justify our concern that the station would have anomalous effects because it is inland. FICA, however, does have a large site effect, perhaps in part because it is inland, but also perhaps in part due to its location on a ridge.

CONCLUSIONS

We derive attenuation functions that describe the decay of the spectral amplitudes with distance at different frequencies ($0.1 < f < 40$ Hz). These curves were used to obtain a frequency dependent quality factor Q of S-waves that can be approximated by $1/Q(f) = 1/3413 + 1/248f$ and $1/Q(f) = 1/2882 + 1/104f$ assuming that the geometrical spreading is proportional to $1/r$ and $(1/r)^{1/2}$ respectively. Between 0.8 and 6 Hz, the values of Q depart considerably from the above relations, suggesting a more complicated frequency dependence of Q .

The spectral decay of the displacement source functions obtained after correcting the spectral amplitudes by the effect of attenuation tends to increase as the magnitude of the event increases for $m_b > 4.2$. The low stress drop ($\Delta\sigma < 20$ bars) estimated for the largest events using Brune's model seems to be a common characteristic of subduction zone events (e.g. Kanamori and Anderson, 1975, Singh et al. 1981, 1984) in the Guerrero region. However, these low stress drops can also be explained by a partial stress drop mechanism (Brune, 1970).

The source and the site response functions obtained are consistent with those obtained using an entirely parametric model. Stations that show important site effects (e.g. OCTT, LLAV) can have amplifications up to 6 times compared to other stations at frequencies perhaps related to the natural frequency of the site. Although the models used to derive the site functions (Equations (1-3) and (1-6)) do not account for wave propagation effects such as Moho reflections, these have been minimized by introducing smoothing constraints in the analyses. However, if reflections or other wave propagation mechanisms are affecting the spectral amplitudes, then the site functions here obtained would carry that effect. In any event, the site functions obtained show that the near surface characteristics of hard rock sites should be taken into account for future spectral studies in this area.

Alvarez, J. M., Villavicencio, B., V. V. V. V., F. Perez, E. Casavari, L. E. de Peris (1988). Centro de Mexico: Accelerograph Array: Summary of data collected in January to June, 1987, Report OAA-3, Seismological Laboratory, Mackay School of Mines, University of Nevada, Reno.

Anderson, J. G. and R. Quast (1984). The Mexico earthquake of September 19, 1985: effect of magnitude on the character of strong ground motion: An example from the Guerrero, Mexico strong motion network. *Earthquake Spectra* 1, 635-646.

Anderson, J. G., R. Quast, S. K. Singh, R. Castro, D. Alvarez, J. H. Velasco, B. Jena, R. Vasquez, G. Castro, C. Perez, B. Lopez, and E. Mejia (1987). Accelerograms from the Guerrero, Mexico, strong motion array for the April 25, 1987 earthquake (M=6.9). A preliminary report, Report OAA-4, Seismological Laboratory, Mackay School of Mines, University of Nevada, Reno.

Anderson, J. G. (1970). A preliminary descriptive model for the dynamic characteristics of the spectral decay parameter in southern California. *Submitted*.

Andrews, D. T. (1986). Objective determination of source parameters and estimation of earthquake of distance and hypocenter. *Geophys. Res. Lett.* 13, 229-237, American Geophysical Union.

Angelino, R. A. (1989). Estimación del momento de atracción sísmica a partir de aceleraciones fuertes en la costa de Guerrero, México. M. S. Thesis, Fac. de Ingeniería, UNAM.

Arrowsmith, R. J., R. Crowder, C. Wood, and J. Spudich (1982). Source parameters of the 1980 Magnitude 6.5, California earthquake sequence. *J. Geophys. Res.* 87, 4595-4607.

Auda, L. and H. Barrozo (1984). An earthquake of magnitude 6.5 in Guerrero, Guerrero, Mexico. *Phys. Earth Planet. Interiors* 34, 21-48.

REFERENCES

- Aki, K. and P. Richards (1980). *Quantitative seismology: Theory and methods*, W.H. Freeman and Company, San Francisco, Calif.
- Anderson, J. G. and S. E. Hough (1984). A model for the shape of the Fourier amplitude spectrum of acceleration at high frequencies, *Bull. Seism. Soc. Am.* 74, 1969-1993.
- Anderson, J. G., P. Bodin, J. N. Brune, J. Prince, S. K. Singh, R. Quaas, and M. Onate (1986). Strong ground motion from the Michoacan, Mexico earthquake, *Science* 233, 1043-1049.
- Anderson, J. G., R. Quaas, D. Almora, J. M. Velasco, E. Guevara, L. E. de Pana, A. Gutierrez, and R. Vazquez (1987). Guerrero, Mexico Accelerograph Array: Summary of data collected in 1986, Report GAA-3, Institute of Geophysics and Planetary Physics, UC San Diego, La Jolla, CA, 185pp.
- Anderson, J. G., R. Quaas, D. Almora, J. M. Velasco, R. Vazquez, P. Perez, E. Guevara, L. E. de Pavia (1988). Guerrero, Mexico Accelerograph Array: Summary of data collected in January to June, 1987, Report GAA-5, Seismological Laboratory, Mackay School of Mines, University of Nevada, Reno.
- Anderson, J. G. and R. Quaas (1988). The Mexico earthquake of September 19, 1985-effect of magnitude on the character of strong ground motion: An example from the Guerrero, Mexico strong motion network, *Earthquake Spectra* 4, 635-646.
- Anderson, J. G., R. Quaas, S. K. Singh, R. Castro, D. Almora, J. M. Velasco, E. Mena, R. Vasquez, G. Castro, C. Perez, B. Lopez, and R. Mejia (1989). Accelerograms from the Guerrero, Mexico, strong motion array for the April 25, 1989 earthquake ($M_s=6.9$): A preliminary report, Report GAA-6, Seismological Laboratory, Mackay School of Mines, University of Nevada, Reno.
- Anderson, J. G. (1989). A preliminary descriptive model for the distance dependence of the spectral decay parameter in southern California. Submitted.
- Andrews, D. J. (1986). Objective determination of source parameters and similarity of earthquakes of different size, in *Earthquake Source Mechanics*, Geophys. Monogr. 37, Maurice Ewing Vol. 6, pp 259-267, American Geophysical Union.
- Anguiano, R. A. (1989). Estimacion del parametro de atenuacion usando espectros de movimientos fuertes en la costa de Guerrero, Mexico, M. S. Thesis, Fac. de Ingenieria, UNAM.
- Archuleta, R. J., E. Cranswick, C. Mueller, and P. Spudich (1982). Source parameters of the 1980 Mammoth lakes, California earthquake sequence, *J. Geophys. Res.* 87, 4595-4607.
- Astiz, L. and H. Kanamori (1984). An earthquake doublet in Ometepec, Guerrero, Mexico, *Phys. Earth Planet. Interiors* 34, 24-45.

- Baker, J. S. (1988). Wave propagation modeling of ground-motion attenuation in the Northeastern United States and adjacent Canada, Proceedings of EPRI conference on earthquake ground-motion estimation in Eastern North America.
- Boore, D. M. (1986). Short-period P- and S-wave radiation from large earthquakes: Implications for spectral scaling relations, *Bull. Seism. Soc. Am.*, 76, 43-64.
- Brune, J. N. (1970). Tectonic stress and the spectra of seismic shear waves from earthquakes, *J. Geophys. Res.*, 75, 4997-5009.
- Brune, J. N., J. Fletcher, F. L. Vernon, L. Harr, T. C. Hanks, and J. Berger (1986). Low stress-drop earthquakes in light of new data from the Anza, California telemetered digital array, in *Earthquake Source Mechanics*, Geophys. Monogr. 37, Maurice Ewing Vol.6, pp 269-274, American Geophysical Union.
- Chael, E. P. and G. S. Stewart (1982). Recent large earthquakes along the Middle American trench and their implications for the subduction process, *J. Geophys. Res.*, 87, 329-338.
- Frankel, A. (1982). The effects of attenuation and site response on the spectra of micro-earthquakes in the Northeastern Caribbean, *Bull. Seism. Soc. Am.*, 72, 1379-1402.
- Hanks, T.C. (1982). f_{max} , *Bull. Seism. Soc. Am.* 72, 1867-1879.
- Hough, S. E., J. G. Anderson, J. N. Brune, F. Vernon, III, J. Berger, J. Fletcher, L. Haar, T. Hanks, and L. Baker (1988). Attenuation near Anza, California, *Bull. Seism. Soc. Am.*, 78, 672-691.
- Kanamori, H., and D. L. Anderson (1975). Theoretical basis of some empirical relations in seismology, *Bull. Seism. Soc. Am.*, 65, 1073-1096.
- Keilis-Borok, V. (1960). Investigation of the mechanism of earthquakes, *Sov. Res. Geophys.* 4, 201 pp.
- Mahdyiar, M., S. K. Singh, and R. P. Meyer (1986). Moment-magnitude scale for local earthquakes in the Petatlan region, Mexico, based on recorded peak horizontal velocity, *Bull. Seism. Soc. Am.* 76, 1225-1240.
- Menke, W. (1984). *Geophysical data analysis: Discrete inverse theory*, Academic Press, Inc., New York.
- Novelo-Casanova, D. A., E. Berg, V. Hsu, and C. E. Helsley (1985). Time-space variation of seismic S-wave coda attenuation (Q_c) and magnitude distribution (b-values) for the Petatlan earthquake, *Geophys. Res. Lett.* 12, 789-792.
- Papageorgiou, A. and K. Aki (1983a). A specific barrier model for the quantitative description of inhomogeneous faulting and the prediction of strong ground motion. Part I. Description of the model, *Bull. Seism. Soc. Am.* 73, 693-722.
- Papageorgiou, A. and K. Aki (1983b). A specific barrier model for the quantitative description of inhomogeneous faulting and the prediction of strong ground motion. Part II. Application of the model, *Bull. Seism. Soc. Am.* 73, 953-978.

- Phillips, W. S. and K. Aki (1986). Site amplification of coda waves from local earthquakes in Central California, *Bull. Seism. Soc. Am.*, 76, 627-648.
- Richards, P. G. and W. Menke (1983). The apparent attenuation of a scattering medium, *Bull. Seism. Soc. Am.*, 73, 1005-1021.
- Rodriguez, M., J. Havskov, and S. K. Singh (1982). Q for coda waves near Petatlan, Guerrero, Mexico, *Bull. Seism. Soc. Am.* 73, 321-326.
- Rovelli, A. (1982). On the frequency dependence of Q in Friuli from short-period digital records, *Bull. Seism. Soc. Am.* 72, 2369-2372.
- Singh, S. K., L. Astiz and J. Havskov (1981). Seismic gaps and recurrence periods of large earthquakes along the Mexican subduction zone: a reexamination, *Bull. Seism. Soc. Am.*, 71, 827-843.
- Singh, S. K., T. Dominguez, R. Castro, and M. Rodriguez (1984). P waveform of large, shallow earthquakes along the Mexican subduction zone, *Bull. Seism. Soc. Am.* 74, 2134-2156.
- Singh, S. K., E. Mena, and R. Castro (1988). Some aspects of source characteristics of the 19 September, 1985, Michoacan earthquake and ground motion amplification in and near Mexico City from strong motion data, *Bull. Seism. Soc. Am.*, 78, 451-477.
- Singh, S. K., E. Mena, J. G. Anderson, J. Lermo, and R. Quaas (1989). Source spectra and RMS acceleration of Mexican subduction zone earthquakes, *Pure and Applied Geophys.*, In press.
- Tucker, B. E., and J. N. Brune (1973). Seismograms, S-wave spectra, and source parameters for aftershocks of San Fernando earthquake, in San Fernando California Earthquake of February 9, 1971, Vol. III, 69-122, U.S. Department of Commerce.
- Tucker, B. E., J. L. King, D. Hatzfeld, and I. L. Nersesov (1984). Observations of hard-rock site effects, *Bull. Seism. Soc. Am.*, 74, 121-136.
- Vidale, J. E., and D. H. Helmberger (1988). Elastic finite-difference modeling of the 1971 San Fernando, California earthquake, *Bull. Seism. Soc. Am.*, 78, 122-142.
- Vidale, J. E. (1989). Influence of focal mechanism on peak accelerations of strong motions of the Whittier Narrows, California, earthquake and an aftershock, *J. Geophys. Res.*, 94, 9607-9613.
- Wang, C. Y. and R. B. Herrmann (1980). A numerical study of P-, SV-, and SH-wave generation in a plane layered medium, *Bull. Seism. Soc. Am.* 70, 1015-1036.
- Wu, F.T. (1966). Lower limit of the total energy of earthquakes and partitioning of energy among seismic waves. Ph.D. Thesis, California Institute of Technology, Pasadena, 1966.

CHAPTER II

P/S SPECTRAL RATIOS FROM THE GUERRERO ACCELEROGRAPH ARRAY

INTRODUCTION

High amplitude of high frequency P-wave radiation relative to S-wave radiation has been observed in many spectral studies of earthquakes recorded at close distances (Linde and Sacks, 1972; Trifunac, 1972; etc.) and teleseismic distances (Hanks and Wyss, 1972; Wyss and Hanks, 1972; among others). A review of these studies is given by Hanks (1981). Rautian et al. (1978), studying earthquakes from the Garm region observed that in addition to the corner frequency of S being smaller than that of P waves, at high frequencies the ratio of P/S spectra often continued to increase. More recently, Abrahamson and Litehiser (1989) suggested that the ratio of vertical to horizontal peak acceleration increases with magnitude. These observations have been interpreted as an effect of the differences in the attenuation between P and S waves (Furuya, 1969; King and Helmberger, 1975), but it has also been suggested that they are a source property (Tucker and Brune, 1973; Molnar et al., 1973; Rautian et al., 1978; Hanks, 1981).

A fundamental problem in interpreting the differences between the radiated P and S-wave energy is the separation of source and structure. This problem cannot be definitively solved for surface observations since attenuation common to all sites can always be hypothesized. In the light of these difficulties, however, this paper attempts to identify those characteristics of ground motion that would be most useful to discriminate between a source or propagation origin for high amplitudes of the P-wave relative to the S-wave. In brief, if the cause of high P/S spectral amplitudes is caused by a wave propagation effect, then a distance dependence is expected. If it is caused by wave propagation only in the vicinity of the accelerograph site, then variability from site to site is expected. If it is caused by a source effect, then a magnitude dependent effect is expected. In the next section we give some quantitative estimates of the size of the expected effects.

Following this, we apply these criteria to strong motion records from Guerrero, Mexico. These data are specially suited for several reasons. Since the Guerrero network uses digital strong motion accelerographs, it records larger earthquakes with lower corner frequencies than typical networks. Secondly, the stations of the Guerrero Accelerograph Array (GAA) are all sited on igneous or metamorphic outcrops. And finally, the attenuation of S-waves in the region is known from recent studies of Q (Novelo-Casanova et al., 1985; Mahdyiar et al., 1986; Singh et al. 1989; Castro et al. 1990). Thus uncertainties due to propagation path can be minimized.

By comparing the spectral amplitudes of P and S-waves recorded for the GAA at different sites and a variety of distances and azimuths, we will show that the enrichment in high-frequency motion of P-waves compared to S is highly variable, to the point where dependence on the hypocentral distance and the recording site is of lower order. Dependence of the P/S spectral ratio on earthquake size would imply a source phenomenon rather than an effect of attenuation. While our data are equivocal in this

respect, we demonstrate the possibility of the hypothesis that anomalous P-wave radiation may be generated during the rupture process by normal motions, as recently suggested by Brune et al. (1989) and Oden and Martins (1985).

DIAGNOSTIC CHARACTERISTICS

Diagnostics of a Wave Propagation Effect

To explore the effects of wave propagation, we employ a simple model for spectral amplitudes of P and S waves, after Boore (1986):

$$U_v(f,r) = C_v G(r) D_v(f,r) S(f) Z_v \quad (2-1)$$

In (2-1), $U_v(f,r)$ is the spectral amplitude at frequency f and hypocentral distance r , C_v is a scaling factor that depends on wave type and radiation pattern, $G(r)$ is the geometrical spreading, D_v describes the effects of anelastic and scattering attenuation, $S(f)$ is the source function and Z_v is the surface amplification factor. Following Boore, we take $C_v = R_{pv} / 2\pi\rho v^3$ where R_{pv} is radiation pattern, ρ is the density, and v is either α (P velocity) or β (S velocity). The shape of the source function $S(f)$ is controlled mainly by the seismic moment M_0 and the corner frequency f_c ; the later may be different for P- and S-waves. Molnar et al. (1973) showed that dislocation models for which both the duration of slip and the time required for the rupture area to develop are small compared to the time needed by the body waves to cross the source area can generate $f_p > f_s$.

We are primarily interested in the spectral ratio of P to S waves, derived from Equation (2-1). For this purpose, and since our initial object is to investigate wave propagation effects on the spectral ratios, we will assume that P and S waves both follow the same geometrical spreading ($G(r)$), and both have the same source function

S(f). Using an average of R_{pp} over the radiation pattern equal to 0.44, and R_{ps} of 0.60 (Boore and Boatwright, 1984), and assuming $\alpha = 1.732\beta$, gives $C_p / C_s = 0.14$. Combining these with Equation (2-1) gives:

$$\frac{U_p(f, r)}{U_s(f, r)} = 0.14 \frac{Z_p D_p(f, r)}{Z_s D_s(f, r)} \quad (2-2)$$

To account for attenuation along the path and also in the near surface, we expand (2) using the assumption:

$$D_v(f, r) = d_v(f, r) \exp(-\pi \kappa_0 f), \quad (2-3)$$

where $d_v(f, r) = \exp(-\pi f r / v Q_v(f))$ and κ_0 is the decay parameter near the surface (Anderson and Hough, 1984). In Guerrero, unlike in California, κ has a very weak distance dependence, at least for S-waves (J. Humphrey, personal communication), so that in this case d_v effectively isolates the effects of whole path attenuation.

The surface amplification factor is $Z_v = (\rho_0 v_0 / \rho_r v_r)^{1/2}$, where v_0 and ρ_0 are the average crustal velocity and density respectively and v_r and ρ_r the velocity and density near the surface (Boore, 1986), thus $Z_p / Z_s = 1$. Boore introduced a frequency dependence in the amplification factors by averaging the wave velocities over a depth corresponding to a quarter-wavelength using standard crustal velocities. He obtained that for $f < 1$ Hz, $Z_p / Z_s = 1$ and $Z_p < Z_s$ for higher frequencies. Thus by using $Z_p = Z_s$ at high frequencies, we may overestimate the effect of wave propagation in the generation of high P/S ratios. In reality, however, the decreasing velocities, and possible occurrence of stratifications, are likely to generate complicated patterns of amplitude interference

at different frequencies for the P and S waves incident on the site. Castro et al. (1990) found evidence of variability in the S-wave amplification among the Guerrero sites. Because of the limited number of P-waves per station in the data set here used, we cannot infer the P-wave site response. In addition, the variability in site response to incident S- and P-waves cannot be simply modeled. It is likely, however, that the consequence would be introduction of considerable variability from one site to another in the P/S spectral ratios. Thus, we will interpret stability of the P/S spectral ratios with regard to observations on several sites as evidence that near surface site effects are not a dominant factor in controlling the amplitudes.

Several attenuation studies that used stations sited on hard rock (e.g. Frankel, 1982; Anderson and Hough, 1984, among others) indicate that the near-surface attenuation is also an important factor controlling the shape of the spectral amplitudes. Hough et al. (1988), based on estimates of the spectral decay parameter κ , found average values of κ_0 of 7.9 and 4.9 msec for P- and S-waves, respectively, in hard rock at Anza, California, implying higher attenuation for P-waves near the surface. More recently, Frankel and Wennerberg (1989) found for the same region that the values of Q for P and S of the shallow layer below the stations are not significantly different. Since the stations of the GAA are also on hard rock, we expect the near-surface attenuation of P- to be comparable to that for the S-waves.

To evaluate the attenuation function (Equation 2-3) quantitatively, we use the values of $Q_s(f)$ reported by Castro et al. (1990) for Guerrero (see Figure 2-1) and $\kappa_s = 0.02$. Although Q for P-waves is not known for the Guerrero region, we can estimate upper and lower limits by using values of Q_p / Q_s reported in other studies (e.g. Hough and Anderson, 1988). Observed values of Q_p / Q_s varied from 0.58 for Central Asia (Rautian et al., 1978) to 1.66 for the San Andreas region. Hough et al. (1988) obtained a $Q_p / Q_s = 0.83$ for California from observations on hard rock sites. We used this value and $Q_p / Q_s = 9/4$ (Knopoff, 1964) as the lower and upper limits, respectively, for our calcu-

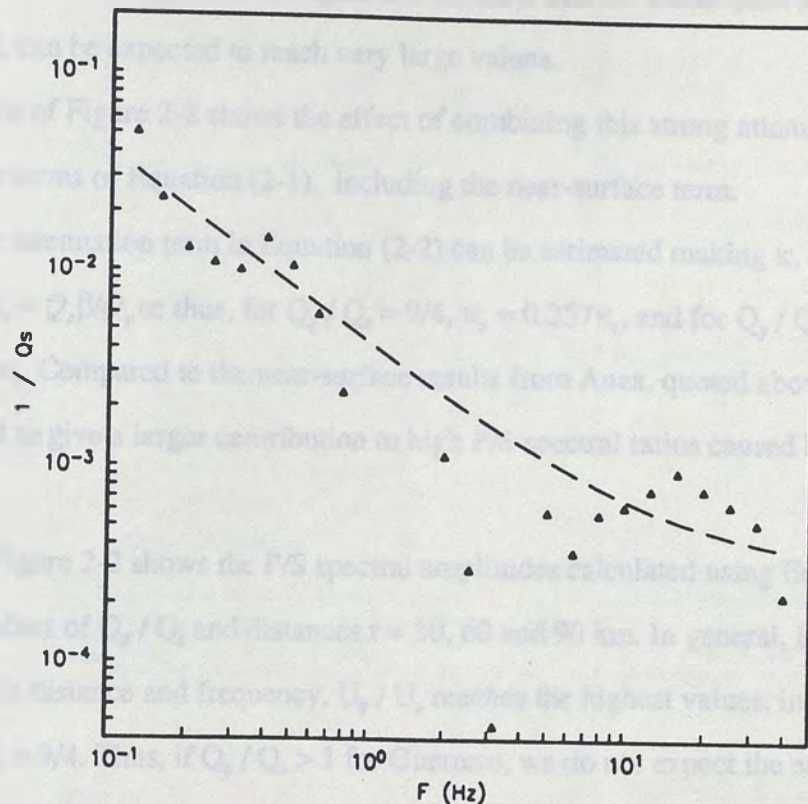


Figure 2-1. $1/Q_s$ for S-waves in Guerrero taken from Castro et al. (1990). The dash line correspond to the Q frequency relation $1/Q_s = 1/3413 + 1/248f$.

lations. On the right side of Figure 2-2, we isolate the attenuation effect along the path (d_p), and plot the P/S ratio as a function of frequency. For the entire range of Q_p/Q_s considered, d_p/d_s increases with distance. The increase is more rapid for larger values of Q_p/Q_s . The Figures on the right side of Figure 2-2 all show that for whole-path attenuation alone, d_p/d_s can be expected to reach very large values.

The left side of Figure 2-2 shows the effect of combining this strong attenuation factor with other terms of Equation (2-1), including the near-surface term.

The near surface attenuation term in Equation (2-2) can be estimated making $\kappa_v = r / Q_s v$, so that $\kappa_p / \kappa_s = Q_s \beta / Q_p \alpha$; thus, for $Q_p / Q_s = 9/4$, $\kappa_p = 0.257 \kappa_s$, and for $Q_p / Q_s = 0.83$, $\kappa_p = 0.693 \kappa_s$. Compared to the near-surface results from Anza, quoted above, these values tend to give a larger contribution to high P/S spectral ratios caused by attenuation.

The left side of Figure 2-2 shows the P/S spectral amplitudes calculated using Equation (2-1) for three values of Q_p / Q_s and distances $r = 30, 60$ and 90 km. In general, U_p / U_s still increases with distance and frequency. U_p / U_s reaches the highest values, in excess of 1.0, for $Q_p / Q_s = 9/4$. Thus, if $Q_p / Q_s > 1$ for Guerrero, we do not expect the effect of differential attenuation of P and S waves to appear at short distances unless it also shows a very strong distance dependence. Notice also that if $S(f)$ is the same for P and S waves, then U_p / U_s is independent of magnitude.

Diagnostics of a Source Effect

Recent studies of rupture mechanism in foam rubber by Brune et al. (1989) and numerical modeling of stick-slip by Oden and Martins (1985) have suggested that normal motions are an important factor in the rupture process. Haskell (1964) has also shown numerically that tensile fault ruptures introduced additional energy in the P radiation compared with a pure shear faulting. Blandford (1975) combined Haskell's results for the far field radiation of tensile and shear faults to explain the corner frequency shift of shallow earthquakes (Trifunac, 1972; Molnar et al., 1973; Hanks, 1981).

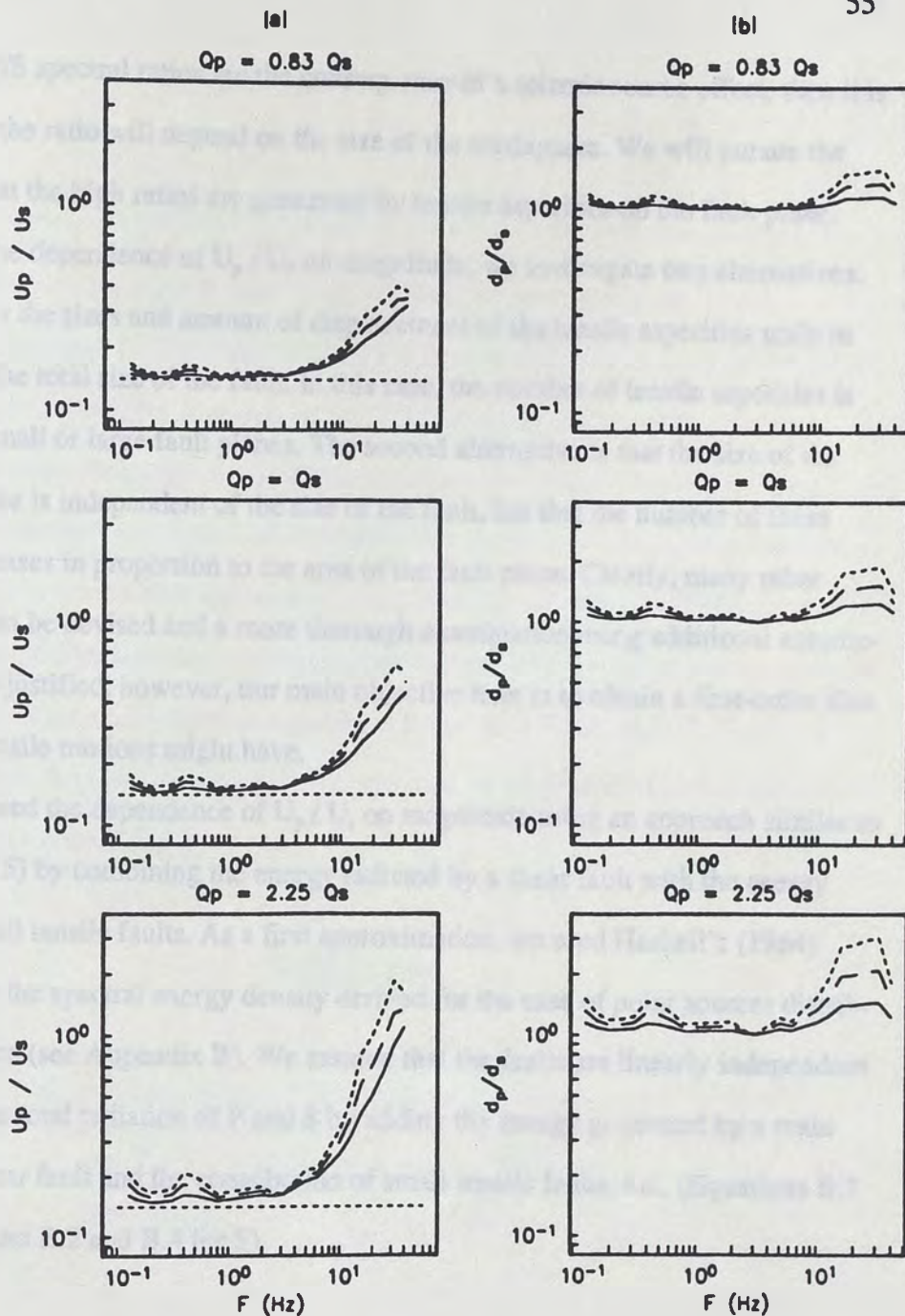


Figure 2-2. (a) P/S spectral ratio calculated using equation 1 and the values of $Q(f)$ for S-waves reported by Castro et al. (1990). Solid line for a hypocentral distance of 30 km, dashed line for 60 km and dotted line for 90 km. (b) P/S attenuation ratio along the path for the same distances used in (a).

If high P/S spectral ratios are the consequence of a seismic source effect, then it is plausible that the ratio will depend on the size of the earthquake. We will pursue the assumption that the high ratios are generated by tensile asperities on the fault plane. Then, to test the dependence of U_p / U_s on magnitude, we investigate two alternatives. The first is that the sizes and amount of displacement of the tensile asperities scale in proportion to the total size of the fault. In this case, the number of tensile asperities is the same for small or large fault planes. The second alternative is that the size of the tensile asperities is independent of the size of the fault, but that the number of these asperities increases in proportion to the area of the fault plane. Clearly, many other assumptions can be devised and a more thorough examination using additional assumptions would be justified, however, our main objective here is to obtain a first-order idea of the effect tensile motions might have.

We explored the dependence of U_p / U_s on magnitude using an approach similar to Blandford (1975) by combining the energy radiated by a shear fault with the energy radiated by small tensile faults. As a first approximation, we used Haskell's (1964) expressions for the spectral energy density derived for the case of point sources distributed over a plane (see Appendix B). We assume that the faults are linearly independent and simulate the total radiation of P and S by adding the energy generated by a main longitudinal shear fault and the contribution of small tensile faults, i.e., (Equations B.1 and B.3 for P; and B.2 and B.4 for S)

$$E_v(\omega) = E_v(\omega)^L + n E_v(\omega)^T \quad (2-4)$$

The spectral density of the far-field radiated energy can also be expressed in terms of the displacement spectrum (Haskell, 1967) as:

$$E_v(\omega) = 8\pi\rho v r^2 \omega^2 U_v(\omega)^2 \quad (2-5)$$

where ρ is the density, v is either P- or S-wave velocity, r is the distance between the source and the observation point, and $U_v(\omega)$ the displacement spectrum.

Figure 2-3a shows U_p / U_s for the idealized case in which the size of the asperities increases with magnitude for $M = 4, 5$ and 6 . Table 2-1 lists the fault dimensions used. The area of the main fault and the slip chosen satisfies the definition of the seismic moment ($M_0 = \mu A s$) for $\mu = 3.3 \times 10^{11}$ dyne/cm². The duration of the source function for the asperities is scaled with the width ($\tau = W/V_r$) and the opening is 20 % of the slip of the main fault. Large asperities excite the spectral amplitudes of P at low frequencies while small asperities excite them at high frequencies. As a result, U_p / U_s increases with magnitude in the frequency band that is affected by large asperities but not small ones, 5-10 Hz in Figure 2-3a.

TABLE 2-1

Fault parameters used in Figure 2a. The number of subfaults was kept constant ($n=4$). Rupture velocity $V_r = 2.3$ km/sec and distance $r = 40$ km.

M	Main Fault				Subfaults			
	L	W	D	τ	L	W	D	τ
	(km)	(km)	(cm)	(sec)	(km)	(km)	(cm)	(sec)
4	2.24	1.12	1.21	0.97	0.50	0.25	0.242	0.11
5	4.85	2.42	8.15	2.11	1.08	0.54	1.630	0.23
6	10.48	5.24	55.15	4.56	2.34	1.17	11.03	0.51

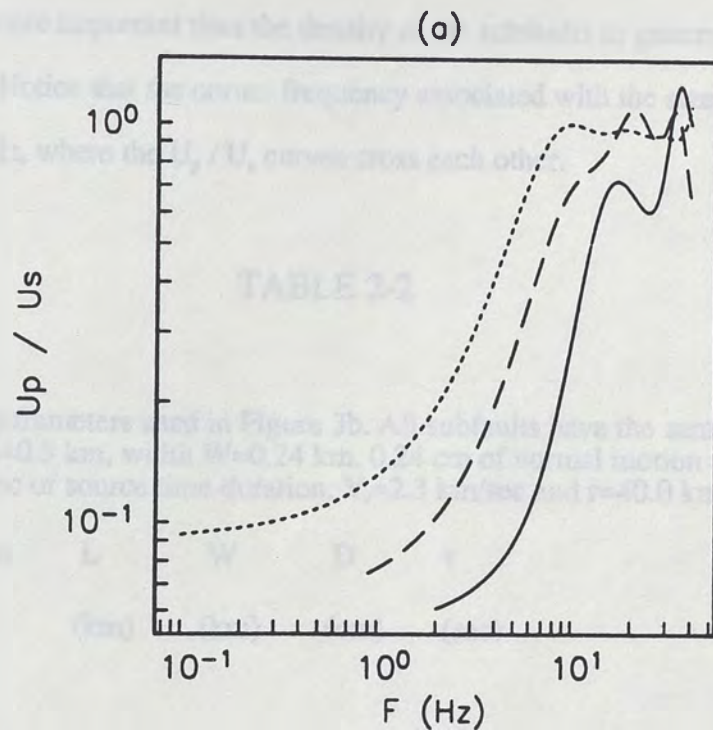


Figure 2-3. (a) Spectral ratio calculated using Equation (B7) of the appendix. The fault dimensions used are listed in Table 2-1. Solid line for a magnitude $M=4$, dashed line for $M=5$ and dotted for $M=6$. The number of subfaults is the same for the three cases ($n=4$).

In Figure 2-3b, we keep the size of the tensile asperities constant and change the number of them with increased magnitude. The sum of the areas of the subfaults is 20 % of the area of the main fault for all three cases. Despite the fewer subfaults for $M=4$, relative to that for $M=5$ and $M=6$, the spectral amplitudes of P at $f > 10$ Hz are considerably greater than S . This indicates that the size of the asperity relative to the size of the main fault is more important than the density of the subfaults in generating high values of U_p / U_s . Notice that the corner frequency associated with the size of the subfault is about 12 Hz, where the U_p / U_s curves cross each other.

TABLE 2-2

Fault parameters used in Figure 3b. All subfaults have the same length $L=0.5$ km, width $W=0.24$ km, 0.24 cm of normal motion and 0.11 sec of source time duration. $V_r=2.3$ km/sec and $r=40.0$ km.

M	n	L (km)	W (km)	D (cm)	τ (sec)
4	4	2.24	1.12	1.21	0.97
5	19	4.85	2.42	8.15	2.11
6	88	10.48	5.24	55.15	4.56

In both cases (Figure 2-3a and Figure 2-3b), the U_p / U_s ratio show potential diagnostic characteristics. In Figure 2-3a, the spectral ratios increase to a high value at a frequency that depends strongly on magnitude. In Figure 2-3b, the ratio also increases at high frequencies above the level expected for a shear crack. In this case also, at high frequencies, the spectral ratio is magnitude dependent, small earthquakes showing a

SUBMITTED DATA SET

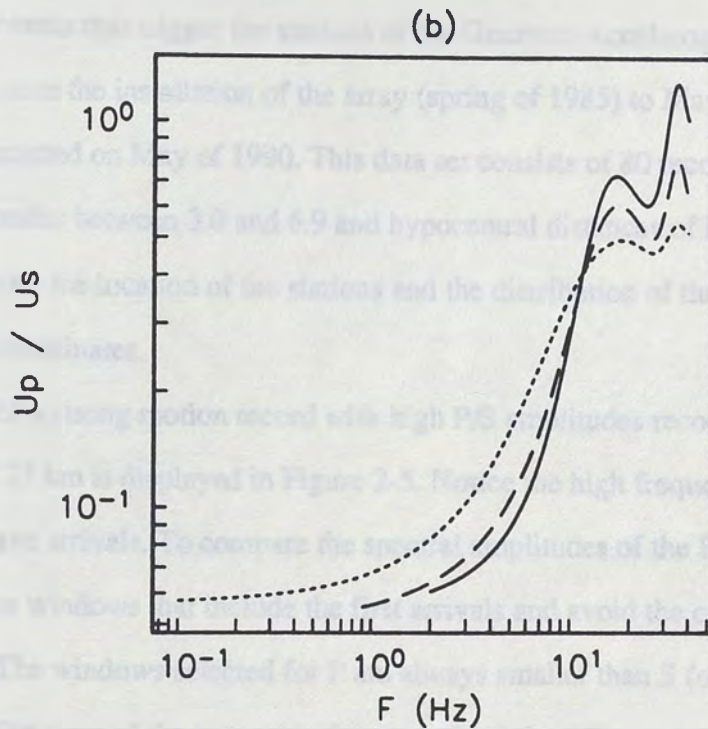


Figure 2-3. (b) Same as in (a) but the dimensions of the subfaults are the same (see Table 2-2). The density of the subfaults increase with M .

higher P/S spectral ratio than large events. The generality of these diagnostic characteristics is unknown at present. We next compare them with actual data from the Guerrero array.

GUERRERO DATA SET

We analyze events that trigger the stations of the Guerrero Accelerograph Array with the P arrival since the installation of the array (spring of 1985) to May of 1989 and four events that occurred on May of 1990. This data set consists of 80 recordings of events with magnitudes between 3.0 and 6.9 and hypocentral distances of less than 120 km. Figure 2-4 shows the location of the stations and the distribution of the events with known epicentral coordinates.

An example of a strong motion record with high P/S amplitudes recorded at hypocentral distance of 23 km is displayed in Figure 2-5. Notice the high frequency energy content in the P-wave arrivals. To compare the spectral amplitudes of the P and S-waves, we choose windows that include the first arrivals and avoid the codas as much as possible. The windows selected for P are always smaller than S (on the average half the size). For most of the cases this does not affect the P/S spectral amplitudes at high frequencies ($f > 1$ Hz). However, when the time windows of the S-waves are considerable larger than the P windows, the S-wave spectra will tend to have higher amplitudes. In the next section we will show that in spite of that, we observed high P/S spectral ratios. The same window was used for the 3 channels to compute the Fourier transform, the spectral amplitudes were smoothed, and then the vectorial sum for each frequency was calculated. Figure 2-5 also shows the square root of the sum of the power spectra of the 3 components as a function of frequency, in dashed lines for P and in solid lines for S. The spectral amplitudes of P for this event exceed the S-wave spectra for frequencies higher than 20 Hz. More typical examples of the spectral amplitudes

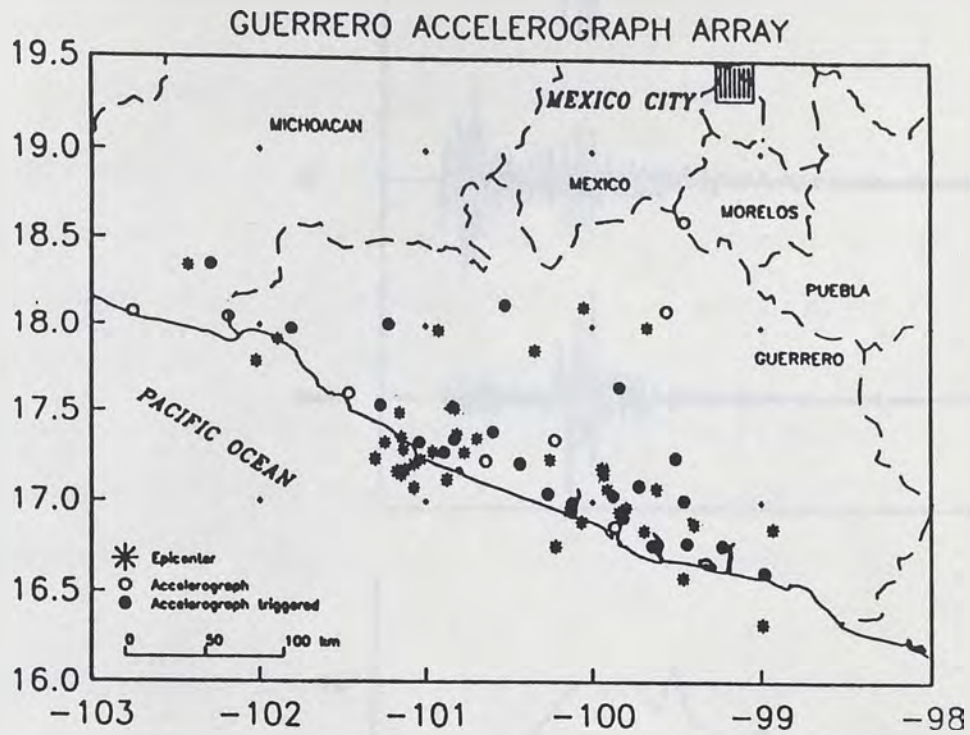


Figure 2-4. Distribution of stations used and locations of events.

Figure 2-5. On top, the acceleration record of a May, 1989 earthquake (M=5.2) at San Marcos (198925). The time window used to calculate the Fourier spectra are indicated with the brackets. Below, the acceleration spectra (square root of the sum of the power spectra of the three components) is displayed. Dashed line for P and solid line for S waves.

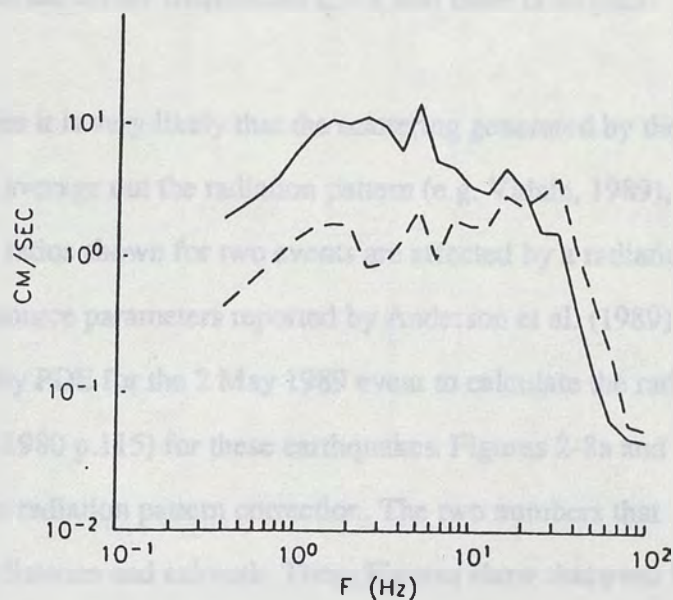
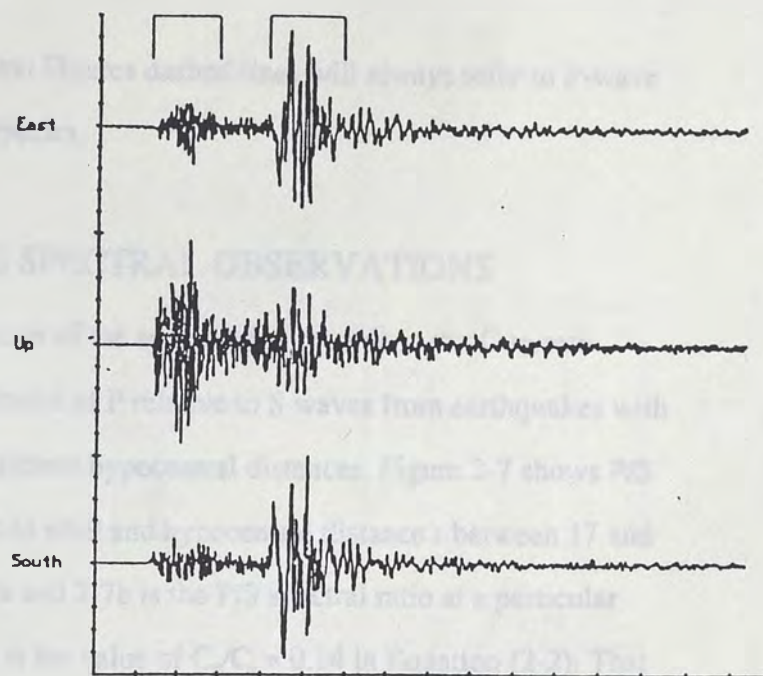


Figure 2-5.

On top, the acceleration record of 2 May, 1989 earthquake ($M=5.2$) at San Marcos (SMR2). The time windows used to calculate the Fourier spectra (square root of the sum of the power spectra of the three components) is displayed. Dashed line for P and solid line for S waves.

analyzed are shown in Figure 2-6.

For comparison purposes, in the next Figures dashed lines will always refer to P-wave spectra and solid lines to S-wave spectra.

P AND S-WAVE SPECTRAL OBSERVATIONS

To analyze the spectral character of the acceleration records in the Guerrero region, we first compare the amplitudes of P relative to S waves from earthquakes with the same magnitude recorded at different hypocentral distances. Figure 2-7 shows P/S spectral ratios for events with $4.2 < M < 6.9$ and hypocentral distance r between 17 and 119 km. Each curve in Figures 2-7a and 2-7b is the P/S spectral ratio at a particular station. The horizontal dashed line is the value of $C_p/C_s = 0.14$ in Equation (2-2). That is the expected value of P/S when the corner frequencies $f_p = f_s$ and there is no path effect.

Although at high frequencies it is very likely that the scattering generated by the structure along the path tends to average out the radiation pattern (e.g. Vidale, 1989), we explore how the P/S spectral ratios shown for two events are affected by a radiation pattern correction. We used the source parameters reported by Anderson et al. (1989) for the 25 April 1989 event and by PDE for the 2 May 1989 event to calculate the radiation pattern (Aki and Richards, 1980 p.115) for these earthquakes. Figures 2-8a and 2-8b show the P/S ratios after the radiation pattern correction. The two numbers that label the curves are hypocentral distance and azimuth. These Figures show that even if the scattering does not average out the radiation pattern, we still observe high P/S spectral values. Notice also that at high frequencies the variability of the ratios increased after the correction suggesting that the uncorrected spectral amplitudes had already averaged out.

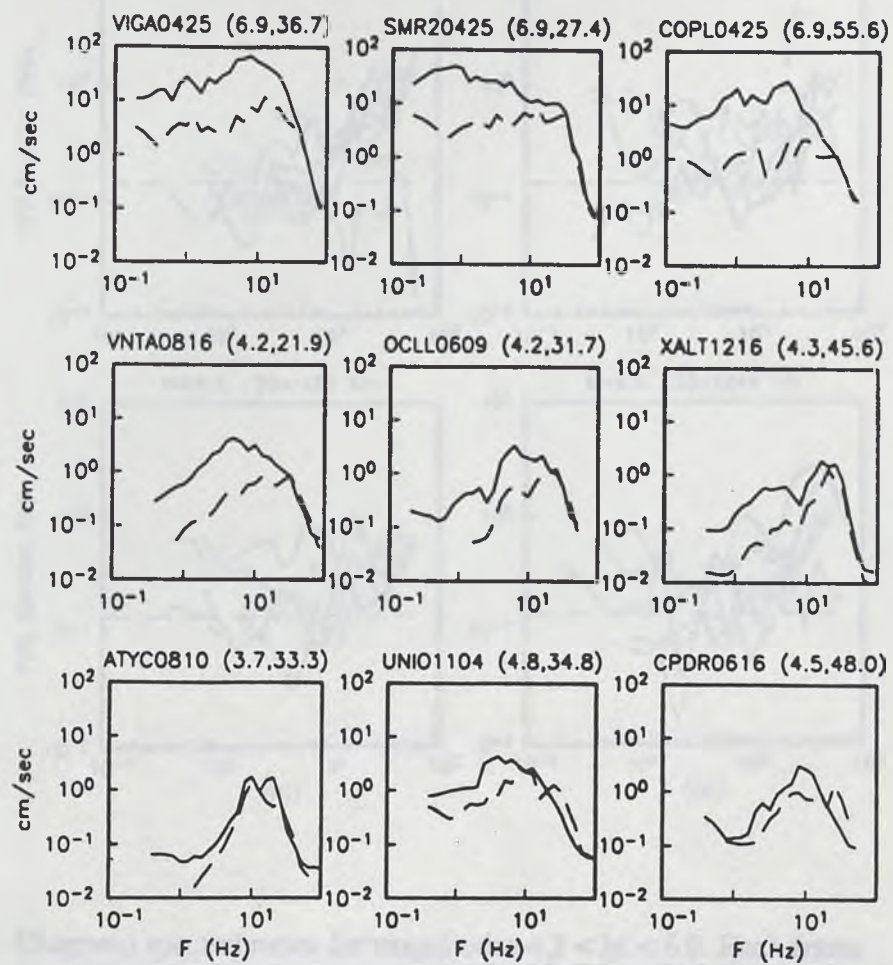


Figure 2-6.

Typical acceleration spectra observed at different sites. The numbers in parenthesis are magnitude and hypocentral distance respectively.

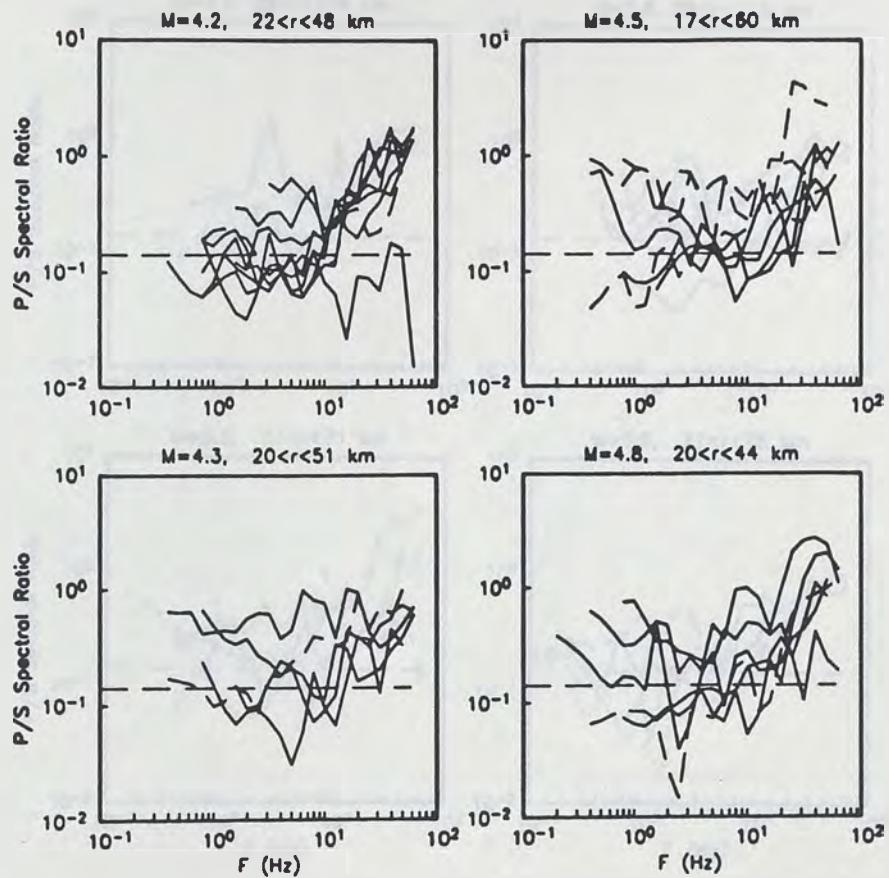


Figure 2-7.

Observed spectral ratios for magnitudes $4.2 < M < 6.9$. Each frame contains several earthquakes, except for $M=5.2$ and $M=6.9$ that have only one. The range of hypocentral distances r is indicated on top of each frame. We used solid lines for events with hypocentral distance $r < 40$ Km, dashed line for $40 < r < 70$, and dotted line for $r > 70$ Km.

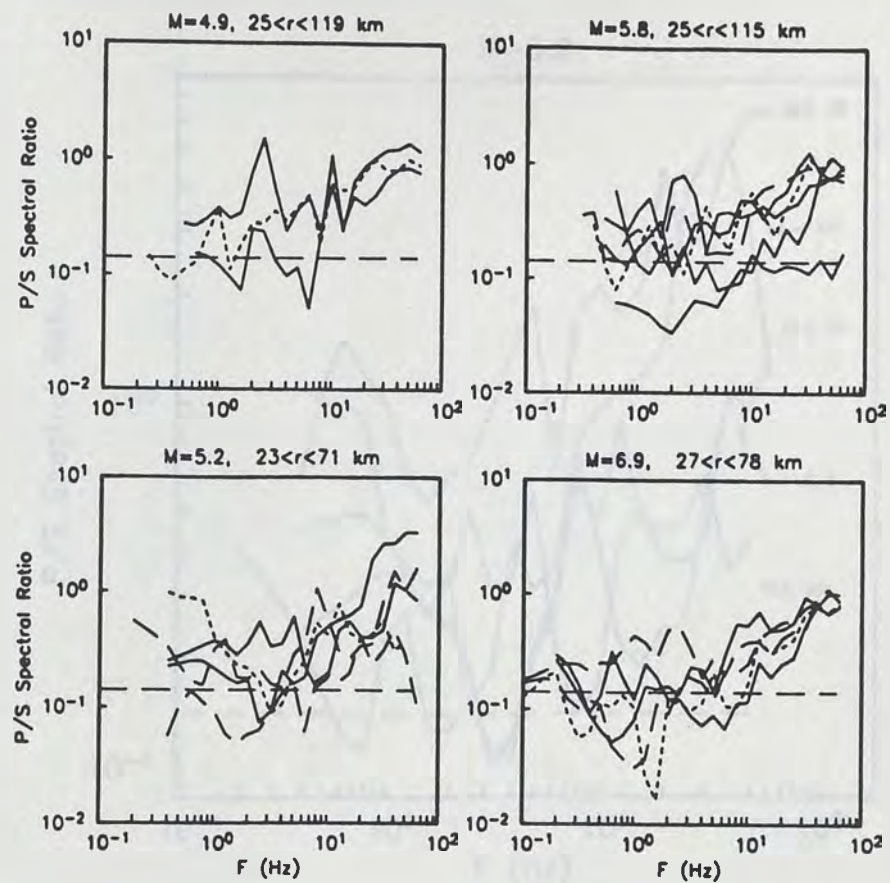


Figure 2-7.

Observed spectral ratios for magnitudes $4.2 < M < 6.9$. Each frame contains several earthquakes, except for $M=5.2$ and $M=6.9$ that have only one. The range of hypocentral distances r is indicated on top of each frame. We used solid lines for events with hypocentral distance $r < 40$ Km, dashed line for $40 < r < 70$, and dotted line for $r > 70$ Km.

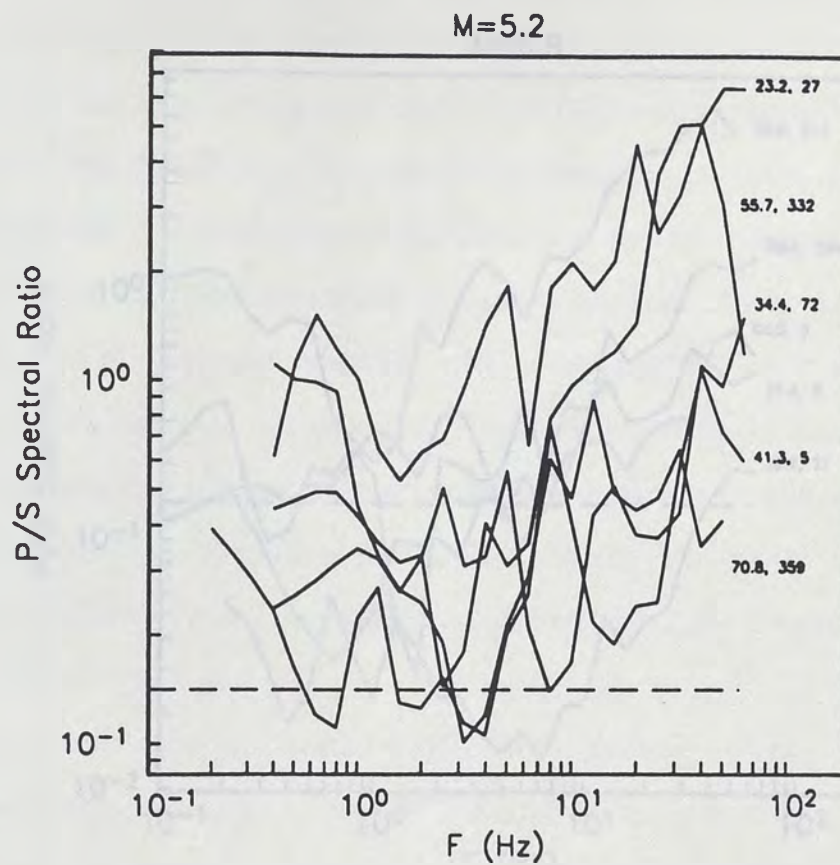


Figure 2-8.

(a) P/S spectral ratios of the 2 May 1989 earthquake after the P and S wave spectra were corrected by the effect of the radiation pattern.

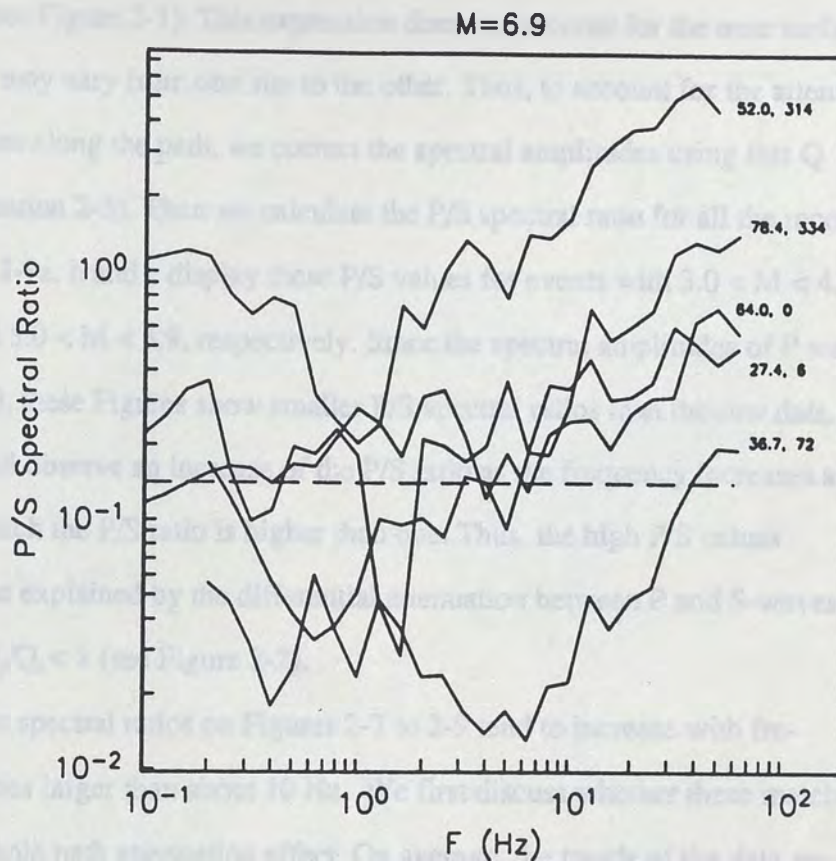


Figure 2-8. (b) Same as in (a) but for the 25 April 1989 event.

We prepare another version of Figure 2-7 by making a partial attenuation correction. Although Q for P is not known in the Guerrero region, we can correct the S -wave spectra using the Q frequency dependent relation derived by Castro et al. (1990) relative to a geometrical spreading function that is proportional to $1/r$, namely $1/Q_s = 1/3413 + 1/248f$ (see Figure 2-1). This expression does not account for the near surface attenuation which may vary from one site to the other. Thus, to account for the attenuation of the S -waves along the path, we correct the spectral amplitudes using this Q function in d_s (Equation 2-3). Then we calculate the P/S spectral ratio for all the records available. Figures 2-9a, b and c display these P/S values for events with $3.0 < M < 4.1$, $4.1 < M < 5.0$, and $5.0 < M < 6.9$, respectively. Since the spectral amplitudes of P were not corrected for Q , these Figures show smaller P/S spectral ratios than the raw data. In spite of this, we still observe an increase of the P/S ratio as the frequency increases and several cases in which the P/S ratio is higher than one. Thus, the high P/S values observed can not be explained by the differential attenuation between P and S -waves along the path if $Q_p/Q_s < 1$ (see Figure 2-2).

In general, the spectral ratios on Figures 2-7 to 2-9 tend to increase with frequency at frequencies larger than about 10 Hz. We first discuss whether these match the criteria for a whole path attenuation effect. On average, the trends of the data are not inconsistent with trends in Figure 2-2, and thus at first glance might be attributed to attenuation. However, the different types of lines for different distance ranges in Figure 2-7 show no significant trends with distance. Nearly half the records have a spectral ratio greater than one, some at frequencies as low as about 20 Hz. As discussed in the previous section (see Figure 2-2), differences in attenuation between P and S can produce P/S ratios greater than one at frequencies $f > 20$ Hz for the extreme case in which $Q_p/Q_s > 2$. However, $Q_p > 2Q_s$ was not found in shallow crustal conditions in any of the papers reviewed by Anderson and Hough (1988). Thus, differences in whole path atten-

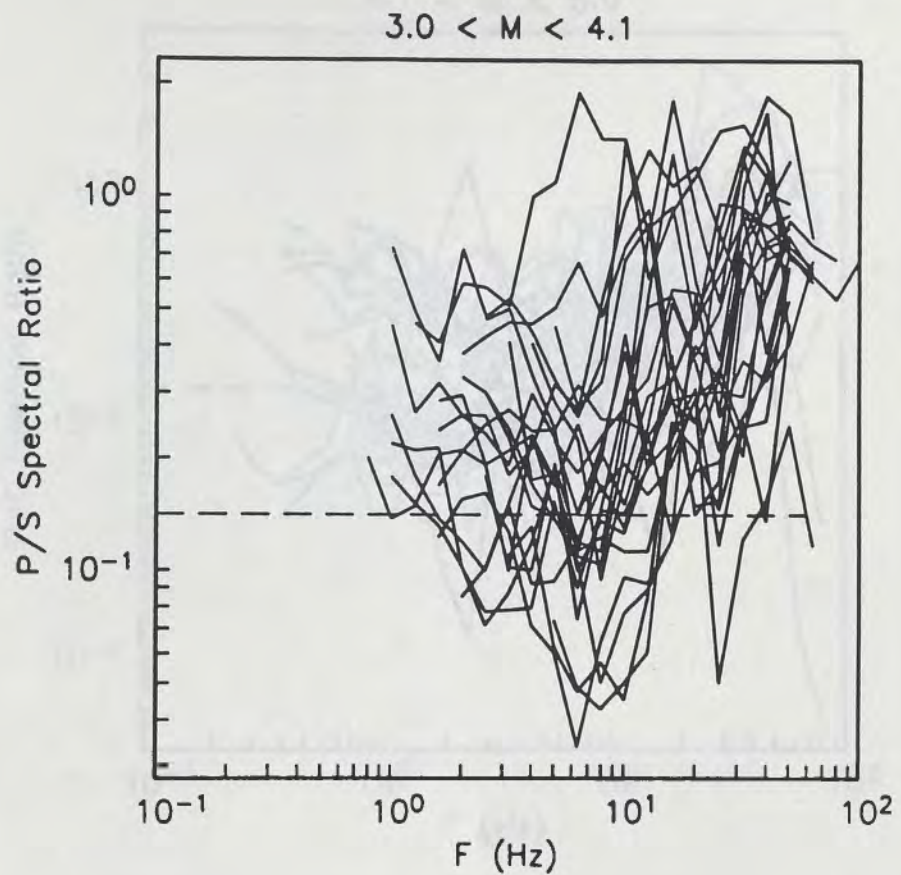


Figure 2-9.

Spectral ratios after the S-wave spectra was corrected by the effect of the attenuation along the path using the $Q(f)$ function reported by Castro et al. (1990). (a) For events with magnitudes between 3.0 and 4.1;

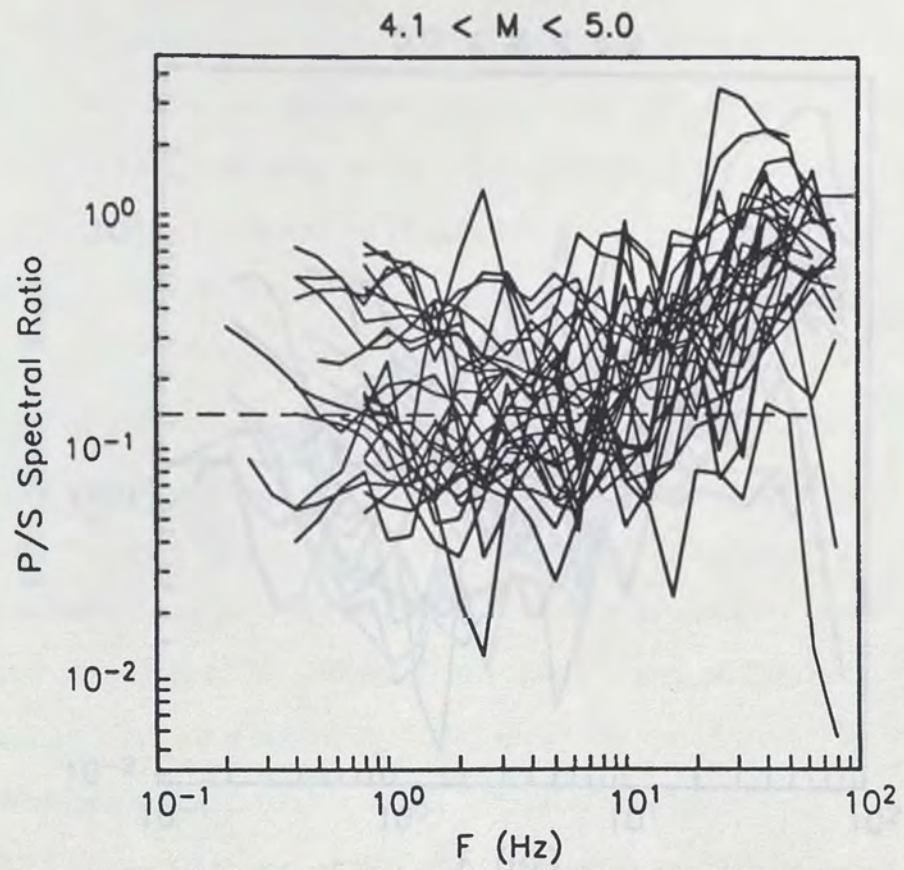


Figure 2-9. (b) for events with M between 4.2 and 5.0;

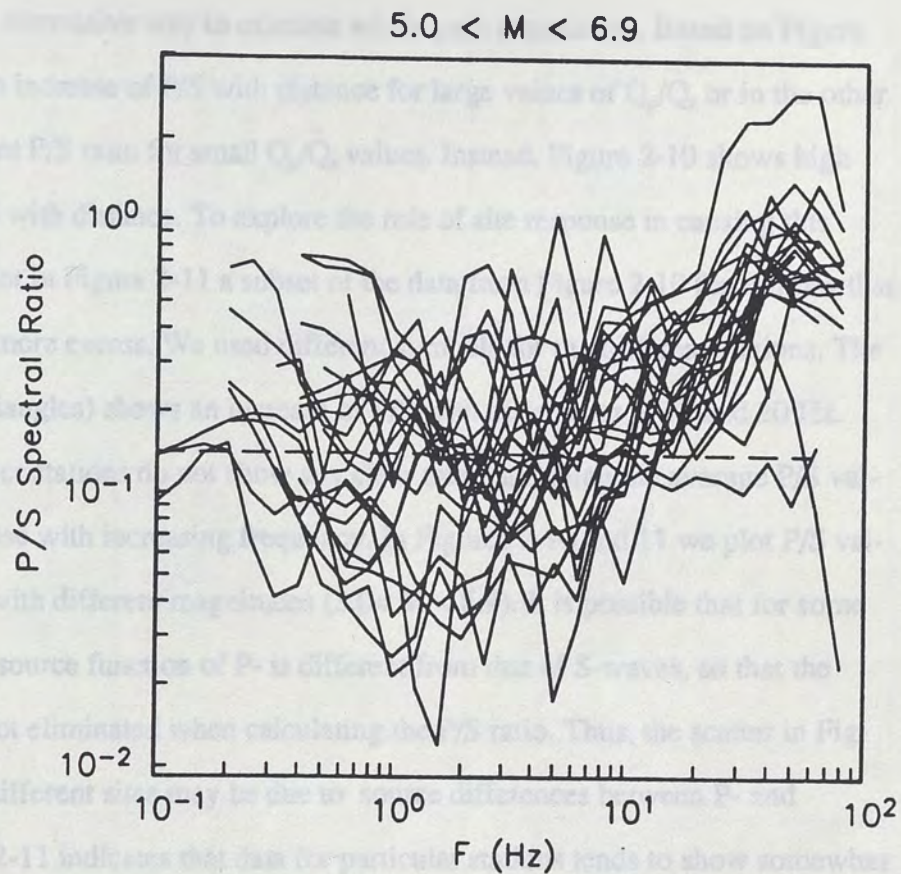


Figure 2-9. (c) for magnitudes between 5.1 and 6.9.

uation between P and S waves alone are not sufficient to explain the high P/S ratios displayed in Figure 2-7; this points toward additional differences in their source functions or site effects.

In Figure 2-10 we plot P/S amplitudes as a function of distance for 2, 3, 5, 10, 20 and 40 Hz, as an alternative way to examine whole path attenuation. Based on Figure 2-2, we expect an increase of P/S with distance for large values of Q_p/Q_s or in the other extreme a constant P/S ratio for small Q_p/Q_s values. Instead, Figure 2-10 shows high variability of P/S with distance. To explore the role of site response in causing this variability, we plot in Figure 2-11 a subset of the data from Figure 2-10 for stations that recorded five or more events. We used different symbols for the different stations. The station OCLL (triangles) shows an increase of P/S with distance at 5, 10 and 20 Hz. However, the other stations do not show any clear trend, although the average P/S values tend to increase with increasing frequency. In Figures 2-10 and 11 we plot P/S values from events with different magnitudes ($3.0 < M < 6.9$). It is possible that for some of the events the source function of P- is different from that of S-waves, so that the source effect is not eliminated when calculating the P/S ratio. Thus, the scatter in Figure 2-11 for the different sites may be due to source differences between P- and S-waves. Figure 2-11 indicates that data for particular stations tends to show somewhat less scatter than the data set as a whole, suggesting a small but non-zero average site effect. Within the scatter, there may be a tendency for the P/S ratio to increase with distance, but the confidence of such a trend is low. Thus the data do not suggest a strong propagation path effect.

We next discuss whether the data match the criteria for a source effect. It is clear from Equation (2-1) that if the source function $S(f)$ is the same for P and S waves ($S(f)_p/S(f)_s = \text{constant}$), then for a fixed distance r the P/S spectral ratio at a given frequency f must be the same for all magnitudes. On Figures 2-7 or 2-9 there are no obvious tendencies for the ratios to depend on magnitude, but a tendency could be

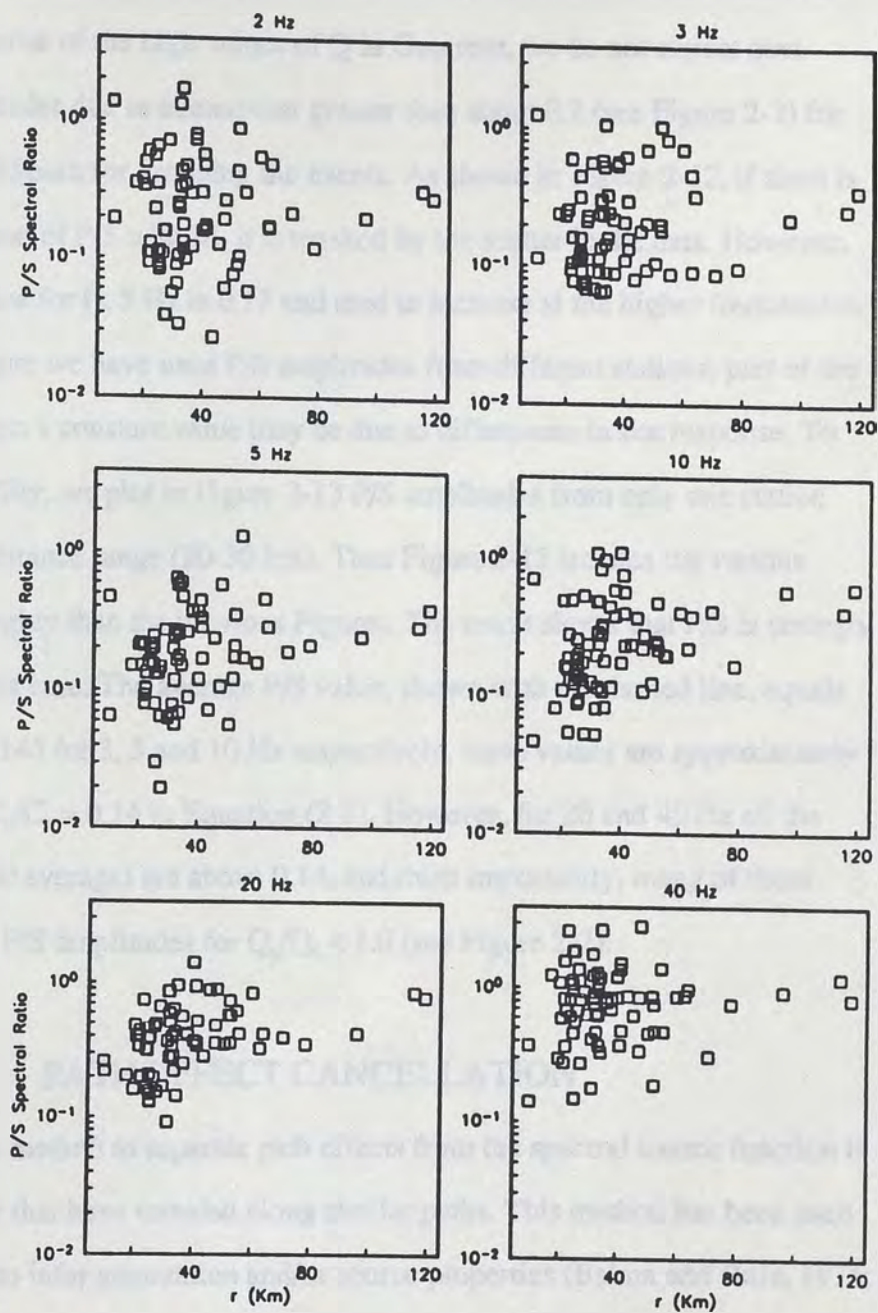


Figure 2-10. Spectral ratios as a function of hypocentral distance for 2, 3, 5, 10, 20 and 40 Hz. The events used have magnitudes $M < 6.9$.

hidden by the scatter in the curves. This is explored more in Figure 2-12 where we plot P/S ratios versus magnitude for the same frequencies as Figure 2-11. We group the events by symbol according to their hypocentral distance. The dashed line is the average P/S value. Because of the high values of Q in Guerrero, we do not expect deviations in P/S amplitudes due to attenuation greater than about 0.2 (see Figure 2-2) for the 10 km interval chosen for grouping the events. As shown in Figure 2-12, if there is a systematic variation of P/S with M , it is masked by the scatter in the data. However, the average P/S value for $f < 5$ Hz is 0.17 and tend to increase at the higher frequencies. Because in this Figure we have used P/S amplitudes from different stations, part of the deviation of P/S from a constant value may be due to differences in site response. To explore this possibility, we plot in Figure 2-13 P/S amplitudes from only one station (PAPN), and one distance range (20-30 km). Thus Figure 2-13 isolates the various effects more thoroughly than the previous Figures. The result shows that P/S is strongly scattered even in this case. The average P/S value, shown with the dashed line, equals 0.144, 0.135 and 0.145 for 3, 5 and 10 Hz respectively, these values are approximately the same value of $C_p/C_s = 0.14$ in Equation (2-2). However, for 20 and 40 Hz all the P/S values (and their average) are above 0.14, and most importantly, many of them above the expected P/S amplitudes for $Q_p/Q_s < 1.0$ (see Figure 2-2).

PATH EFFECT CANCELLATION

An alternative method to separate path effects from the spectral source function is to use wave arrivals that have traveled along similar paths. This method has been used in previous studies to infer attenuation and/or source properties (Bakun and Bufe, 1975; Castro, 1983; Frankel and Wennerberg, 1989; among others). For two events of different size but same focal location and recorded at the same station, the path effect can be

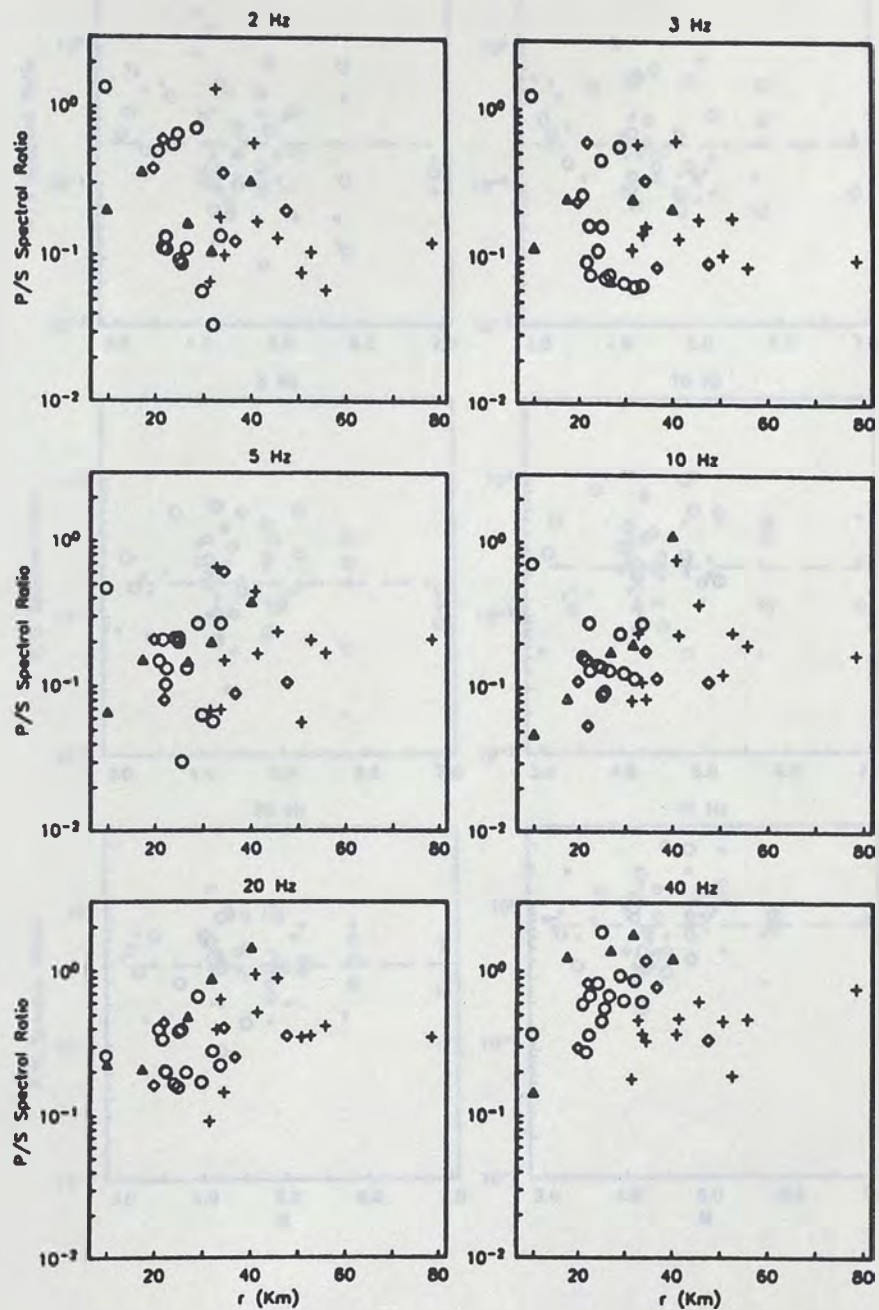


Figure 2-11.

Same as Figure 10. Only stations with 5 or more events are displayed. Different symbols are used to identify the stations as follow: OCLL triangles, PAPN octagons, VIGA diamonds, and XALT pluses.

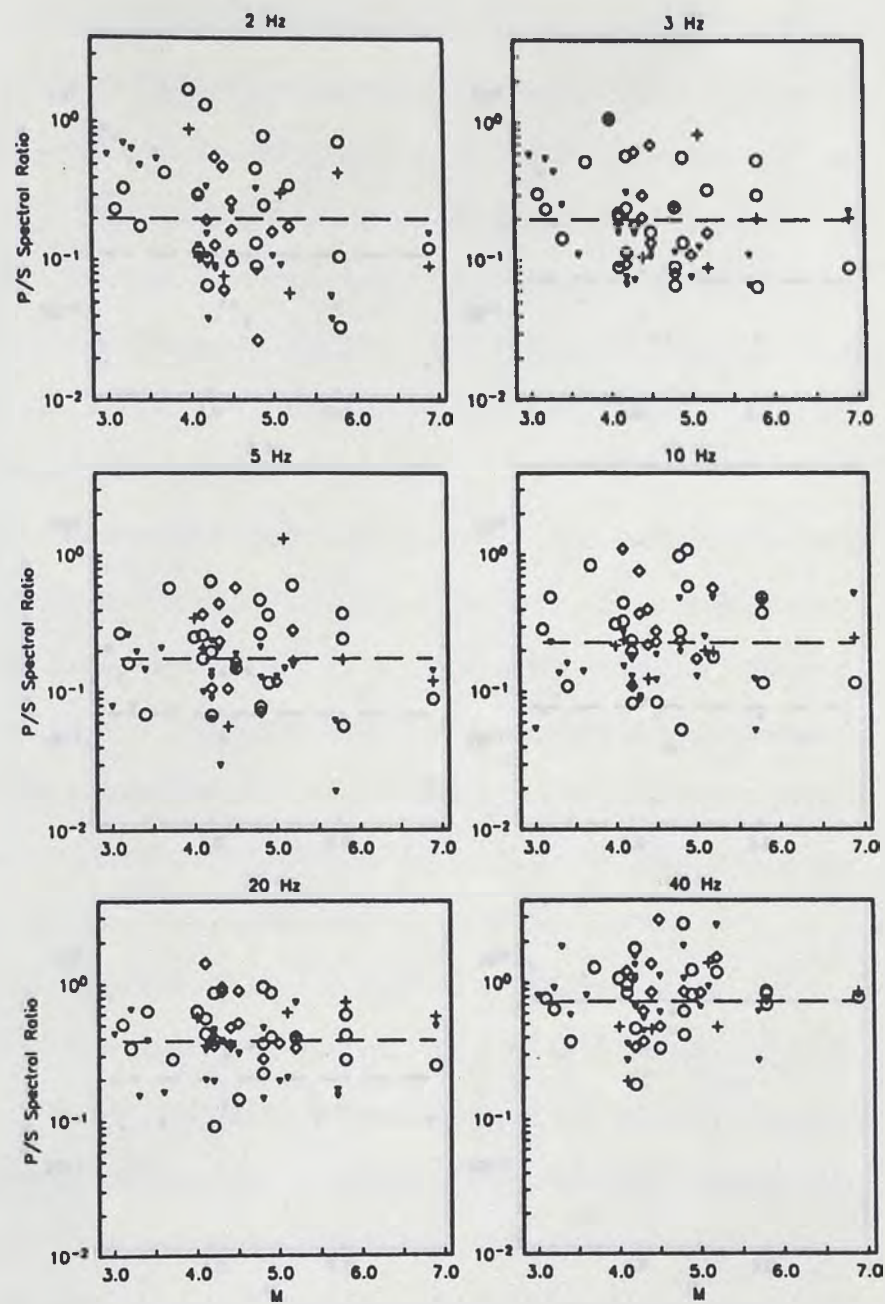


Figure 2-12.

Spectral ratios as a function of magnitude for the same frequencies shown in figure 10. (a) The symbols identify events with same distance range as follows: triangles for $20 < r < 30$ Km, octagons for $30.1 < r < 40$ Km, diamonds for $40.1 < r < 50$ Km, and pluses for $50.1 < r < 60$ Km.

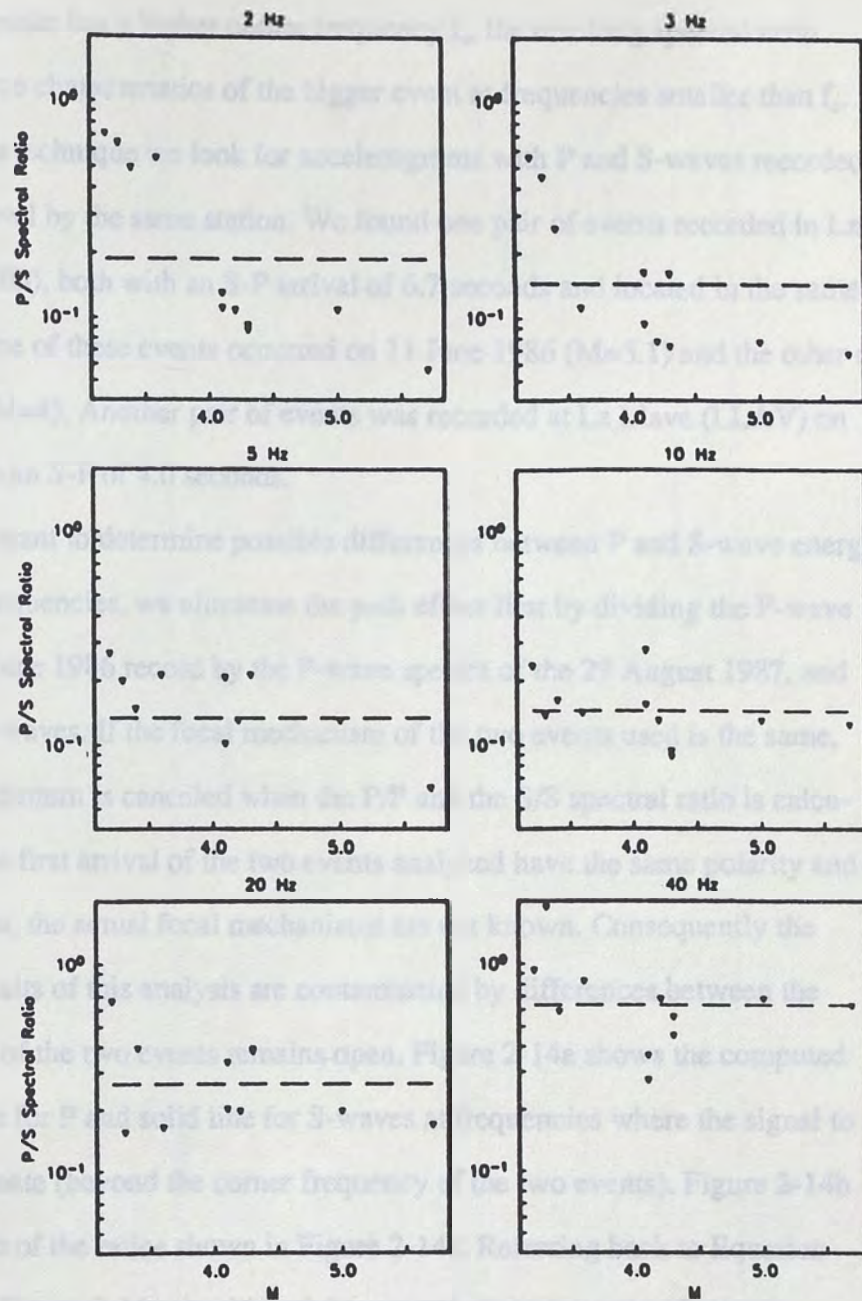


Figure 2-12. (b) same as (a) but only spectral ratios from PAPN is displayed.

eliminated by taking the spectral ratio of the two events for either P- or S-waves. Since the smaller earthquake has a higher corner frequency f_c , the resulting spectral ratio describes the source characteristics of the bigger event at frequencies smaller than f_c .

To apply this technique we look for accelerograms with P and S-waves recorded above the noise level by the same station. We found one pair of events recorded in La Comunidad (COMD), both with an S-P arrival of 6.7 seconds and located in the same epicentral area. One of these events occurred on 11 June 1986 ($M=5.1$) and the other on 29 August 1987 ($M=4$). Another pair of events was recorded at La Llave (LLAV) on 31 May 1990 with an S-P of 4.0 seconds.

Because we want to determine possible differences between P and S-wave energy radiated at high frequencies, we eliminate the path effect first by dividing the P-wave spectra of the 11 June 1986 record by the P-wave spectra of the 29 August 1987, and likewise for the S-waves. If the focal mechanism of the two events used is the same, then the radiation pattern is canceled when the P/P and the S/S spectral ratio is calculated. Although the first arrival of the two events analyzed have the same polarity and similar wave forms, the actual focal mechanisms are not known. Consequently the possibility that results of this analysis are contaminated by differences between the focal mechanisms of the two events remains open. Figure 2-14a shows the computed ratio in dashed line for P and solid line for S-waves at frequencies where the signal to noise ratio is adequate (beyond the corner frequency of the two events). Figure 2-14b shows the P/S ratio of the ratios shown in Figure 2-14a. Referring back to Equation (2-1), the ratios in Figure 2-14a should both be asymptotic to the ratio of seismic moments (23.8 for those events) at low frequencies (not shown). Above the corner frequency of the larger event ($f_c = 1.8$ Hz) the ratio should begin to drop, and then level out beyond the corner frequency of the smaller event ($f_c = 6.3$ Hz). The ratio of ratios is expected to be one at the low frequency asymptote. At high frequencies a value of the ratio of ratios in excess of one indicates that the earthquake in the numerator generated

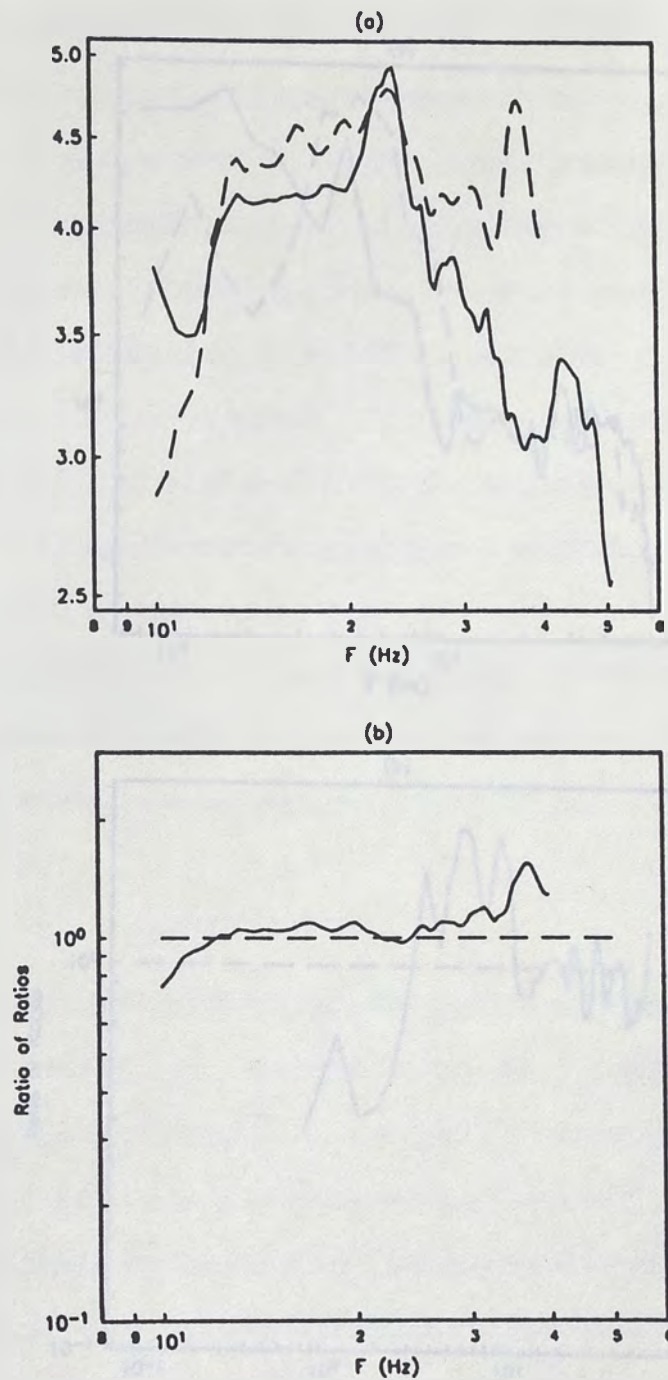


Figure 2-13.

Spectral ratios at COMD (La Comunidad) between the 11 June 1986 ($M=5.1$) and the 29 August 1987 ($M=4$) earthquakes. (a) The dashed line between the P-wave spectra and the solid line between the S-wave spectra. (b) The ratio of the ratios between P and S waves is shown.

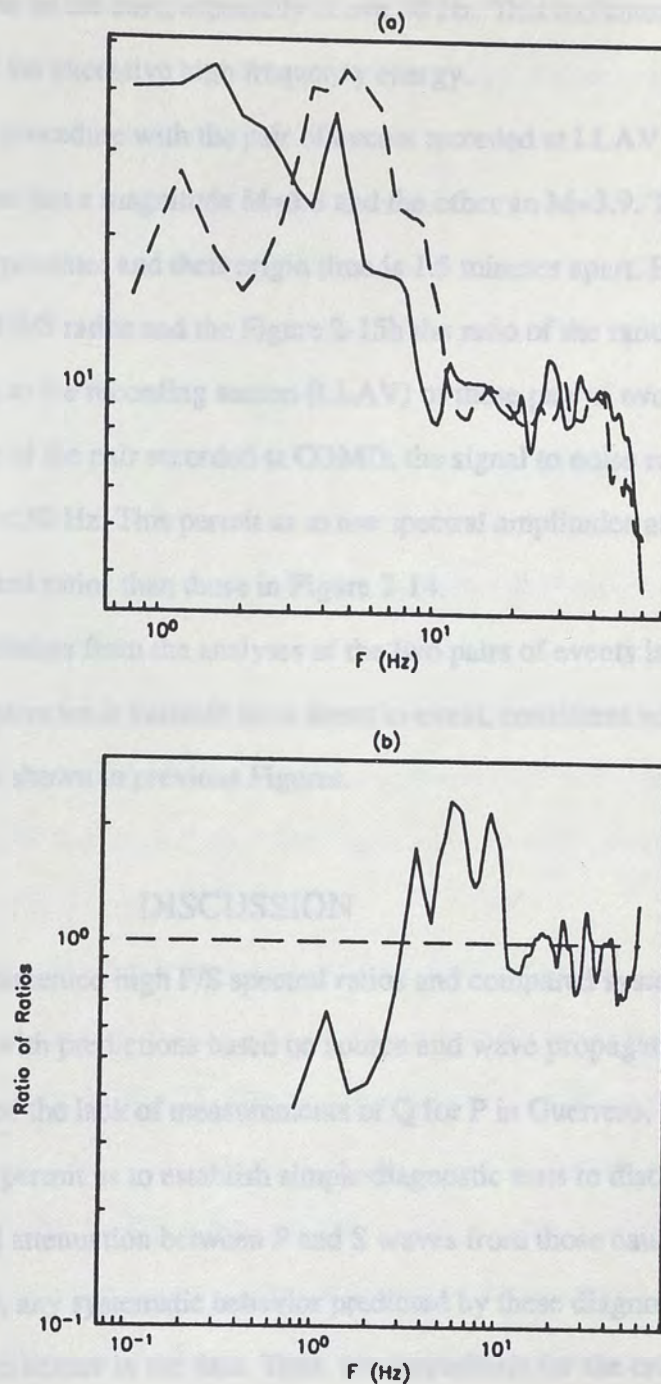


Figure 2-14. Spectral ratios at LLAV from a pair of events recorded on 31 May 1990 at 07hrs:35min ($M=5.8$) and 07hrs:36min ($M=3.9$). As in Figure 13, (a) P/P and S/S ratios; and (b) the ratio of the ratios.

proportionately more high frequency energy than the earthquake in the denominator. Figure 2-14b show this to be the case, especially above 30 Hz. This indicates an origin at the source of some of the excessive high frequency energy.

We used the same procedure with the pair of events recorded at LLAV on 31 May 1990. One of these events has a magnitude $M=5.8$ and the other an $M=3.9$. The two events have the same hypocenter and their origin time is 1.5 minutes apart. Figure 2-15a shows the P/P and S/S ratios and the Figure 2-15b the ratio of the ratios. Since the hypocentral distance to the recording station (LLAV) of these pair of events is shorter than the distance of the pair recorded at COMD, the signal to noise ratio is higher for frequencies $f < 50$ Hz. This permit us to use spectral amplitudes at higher frequencies for the spectral ratios than those in Figure 2-14.

An important conclusion from the analyses of the two pairs of events is that the source ratio of high frequencies is variable from event to event, consistent with the large scatter in the ratios shown in previous Figures.

DISCUSSION

This paper has documented high P/S spectral ratios and compared systematic behavior of these ratios with predictions based on source and wave propagation models for their origin. In spite of the lack of measurements of Q for P in Guerrero, the use of reported values of Q_p/Q_s permit us to establish simple diagnostic tests to distinguish the effects of the differential attenuation between P and S waves from those caused by the source. To a large extent, any systematic behavior predicted by these diagnostic tests has been masked by large scatter in the data. Thus, any hypothesis for the origin of these high ratios must explain the scatter. Figure 2-13 is particularly suggestive towards a unifying hypothesis, since all the effects are isolated. On this Figure, at 10, 20 and 40 Hz particularly, there is a well developed trend of points, with averages at 0.145, 0.265,

and 0.631, respectively, that might be taken to represent the "normal values" incorporating attenuation, that is the value for which $S(f)_p/S(f)_s = \text{constant}$. At 5 Hz, the trend at 0.135 is less well developed. Significant deviations from this trend occur primarily with the occurrence of higher P/S values. We suggest that normal motions on the fault to cause the high deviations, are common, but not universal in occurrence. Quantitative comparison of the "normal values" with Figure 2-2 is interesting. At 5 to 20 Hz, these "normal values" are all closest to the prediction based on attenuation for $Q_p/Q_s < 1$, but at 40 Hz they are greater. While this may be explained by a different Q model, it might also result from a greater probability for 40 Hz data at all the magnitudes considered to be affected by small asperities as suggested by the model presented on Figure 2-3b. Furthermore, we see a tendency for more deviations (i.e., excess of P-wave energy) at small magnitudes than at large. This may be a consequence of a tendency for tensile sub-events, when they occur, to be small (Figure 2-3b) as opposed to the alternative model (Figure 2-3a) in which the tensile sub-events are proportional to the size of the fault. Then, the tendency for the larger events to be more concentrated toward a "normal value" is in line with Figure 2-3b.

In summary, it appears likely that both attenuation and source processes contribute to higher than expected ratios of P- to S-spectra. The sensitivity study in Figure 2-2 shows that, at short ranges ($r < 30$ km), Q alone is not sufficient to generate ratios over one, but it contributes to some increase. Figures 2-3a and 2-3b demonstrate the plausibility of normal motions on the fault generating the high, but variable, ratios at short range. The validity of the assumed source functions, the appropriate strength of the normal motions, and the sensitivity of the calculated ratios to these assumptions remains an open question. We conclude that normal motions during the rupture process may play an important role in determining the amount of high frequency P-wave energy that is radiated.

REFERENCES

- Abrahamson, N. A. and J. J. Litchiser (1989). Attenuation of vertical peak acceleration, *Bull. Seism. Soc. Am.* 79, 549-580.
- Aki, K. and P. Richards (1980). *Quantitative Seismology: Theory and Methods*, W. H. Freeman and Company, San Francisco, California.
- Anderson, J. G. and S. E. Hough (1984). A model for the shape of the Fourier amplitude spectrum of acceleration at high frequencies, *Bull. Seism. Soc. Am.* 74, 1969-1993.
- Anderson, J.G., R. Quaas, S. K. Singh, R. Castro, D. Almora, J.M. Velasco, E. Mena, R. Vasquez, G. Castro, C. Perez, B. Lopez and R. Mejia (1989). Accelerograms from the Guerrero, Mexico, strong motion array for the April 25, 1989 earthquake ($M_L=6.9$): A preliminary report, Report GAA-6, Seismological Laboratory, Mackay School of Mines, University of Nevada, Reno.
- Bakun, W. and C.G. Bufe (1975). Shear wave attenuation along the San Andreas fault zone in central California, *Bull. Seism. Soc. Am.* 65, 439-459.
- Blandford, R.R. (1975). A source theory for complex earthquakes, *Bull. Seism. Soc. Am.*, 65, 1385-1405.
- Boore, D.M. (1986). Short-period P- and S-wave radiation from large earthquakes: Implications for spectral scaling relations, *Bull. Seism. Soc. Am.* 76, 43-64.
- Boore, D.M. and J. Boatwright (1984). Average body-wave radiation coefficients, *Bull. Seism. Soc. Am.*, 74, 1615-1621.
- Brune, J.N., P.A. Johnson and C. Slater (1989). Constitutive relations for foam rubber stick-slip, *Seis. Res. Lett.* 60, 26.
- Castro, R.R. (1983). Source parameters and propagation-path effects for earthquakes in the Baja California Norte and Imperial Valley regions, M.S. Thesis, University of California at San Diego, La Jolla, Calif.
- Castro, R.R., J.G. Anderson, and S.K. Singh (1990). Site response, attenuation and source spectra of S waves along the Guerrero, Mexico, subduction zone, *Bull. Seism. Soc. Am.*, 80, (in press).
- Frankel, A. (1982). The effects of attenuation and site response on the spectra of micro-earthquakes in the Northeastern Caribbean, *Bull. Seism. Soc. Am.*, 72, 1379-1402.
- Frankel, A. and L. Wennerberg (1989). Microearthquake spectra from the Anza, California, seismic network: Site response and source scaling. *Bull. Seism. Soc. Am.*, 79, 581-609.
- Furuya, I. (1969). Predominant period and magnitude, *J. Phys. Earth* 17, 119-126.

- Hanks, T.C. and M. Wyss (1972). The use of body-wave spectra in the determination of seismic-source parameters, *Bull. Seism. Soc. Am.* 63, 561-589.
- Hanks, T. C. (1981). The corner frequency shift, earthquake source models, and Q , *Bull. Seism. Soc. Am.* 71, 597-612.
- Haskell, N.A. (1964). Total energy and energy spectral density of elastic wave radiation from propagating faults, *Bull. Seism. Soc. Am.*, 54, 1811-1841.
- Haskell, N.A. (1967). Analytic approximation for the elastic radiation from a contained underground explosion, *J. Geophys. Res.* 72, 2583-2587.
- Hough, S.E., J.G. Anderson, J. Brune, F. Vernon, III, J. Berger, J. Fletcher, L. Haar, T. Hanks, and L. Baker (1988). Attenuation near Anza, California, *Bull. Seism. Soc. Am.*, 78, 672-691.
- Hough, S.E. and J.G. Anderson (1988). High-frequency spectra observed at Anza, California: Implications for Q structure, *Bull. Seism. Soc. Am.*, 78, 692-707.
- King, D. and D.V. Helmberger (1975). Time functions appropriate for some after-shocks of the Point Magu, California earthquake of February 21, 1973, *Bull. Seism. Soc. Am.* 65, 127-132.
- Knopoff, L. (1964). Q , *Rev. Geophys.* 2, 625-660.
- Linde, A. T. and I. S. Sacks (1972). Dimensions, energy, and stress release for South American deep earthquakes, *J. Geophys. Res.* 77, 1439-1451.
- Mahdyar, M., S. K. Singh, and R. P. Meyer (1986). Moment-magnitude scale for local earthquakes in the Petatlan region, Mexico, based on recorded peak horizontal velocity, *Bull. Seism. Soc. Am.* 76, 1225-1240.
- Molnar, P., B.E. Tucker and J.N. Brune (1973). Corner frequencies of P and S waves and models of earthquake sources, *Bull. Seism. Soc. Am.* 63, 2091-2104.
- Novelo-Casanova, D. A., E. Berg, V. Hsu, and C. E. Helsley (1985). Time-space variation of seismic S-wave coda attenuation (Q_c) and magnitude distribution (b-values) for the Petatlan earthquake, *Geophys. Res. Lett.* 12, 789-792.
- Oden, J.T. and J.A.C. Martins (1985). Models and computational methods for dynamic friction phenomena, *Comp. Meth. Appl. Mech. Eng.*, 52, 527-634.
- Rautian, T.G., V.I. Khalturin, V.G. Martinov, and P. Molnar (1978). The use of coda for determination of the earthquake source spectrum, *Bull. Seism. Soc. Am.* 68, 949-972.
- Singh, S.K., R.J. Apsel, J. Fried and J.N. Brune (1982). Spectral attenuation of SH waves along the Imperial fault, *Bull. Seism. Soc. Am.* 72, 2003-2016.
- Singh, S. K., E. Mena, J. G. Anderson, J. Lermo, and R. Quaas (1989). Source spectra and RMS acceleration of Mexican subduction zone earthquakes, *Pure and Applied Geophys.*, in press.

Trifunac, M. D. (1972). Stress estimates for the San Fernando, California, earthquake of February 9, 1971: main event and thirteen aftershocks, *Bull. Seism. Soc. Am.* 62, 721-750.

Tucker, B.E. and J.N. Brune (1973). Seismograms, S-wave spectra, and source parameters for aftershocks of San Fernando earthquake, in San Fernando, California, Earthquake of February 9, 1971, vol. III, 69-122, U.S. Department of Commerce.

Vidale, J.E. (1989). Influence of focal mechanism on peak accelerations of strong motions of the Whittier Narrows, California, earthquake and an aftershock, *J. Geophys. Res.* 94, 9607-9613.

Wyss, M. and T.C. Hanks (1972). The source parameters of the San Fernando earthquake inferred from teleseismic body waves, *Bull. Seism. Soc. Am.* 62, 591-602.

P AND S-WAVE DISPLACEMENTS FROM KINEMATIC DISLOCATION MODELS

INTRODUCTION

Complex rupture kinematics (e.g. of the kind commonly features reported from many studies of real earthquakes (e.g. Wyss and Brune, 1967; Trifunac and Brune, 1970; Kanamori and Stewart, 1971). The complex nature of the fault displacements is usually interpreted as multiple events (Singh et al., 1984; Anderson et al., 1988; Choy and Boatwright, 1993 among others). These complexities can also be caused by an inhomogeneous distribution of the strength on the fault, by irregularities of the fault geometry (Sibson, 1983, 1989) and by variations of the friction on the fault surface (e.g. irregular rupture front, models that incorporate complexities on planar faults assume stress heterogeneities in the form of Denbro, Ghassemi and Abd, 1987) or in the form of a step (e.g. Sibson and Wallace, 1987). Complexity due to irregularities of the fault geometry has also been considered in terms of roughness (Sibson, 1989).

Recently, in addition to that, Sibson et al. (1989) have suggested that fault-normal

CHAPTER III

P AND S-WAVE DISPLACEMENTS FROM KINEMATIC DISLOCATION MODELS

INTRODUCTION

Complex rupture histories are one of the most common features reported from many studies of real earthquakes (e.g. Wyss and Brune, 1967; Trifunac and Brune, 1970; Kanamori and Stewart, 1978). The complex nature of the fault displacements is usually interpreted as multiple events (Singh et al., 1984; Anderson et al., 1986; Choy and Boatwright, 1988 among others). These complexities can also be caused by an inhomogeneous distribution of the strength on the fault, by irregularities of the fault geometry (Sibson, 1985, 1989) and by variations of the friction on the fault that produce an irregular rupture front. Models that incorporate complexities on planar faults assume stress heterogeneities in the form of barriers (Papageogiou and Aki, 1983) or in the form of asperities (Rudnicki and Kanamori, 1981). Complexity due to irregularities of the fault geometry has also been introduced in models of nonplanar faults (Andrews, 1989).

Recently, in addition to these, Brune et al (1989) have suggested that fault-normal

vibrations are a characteristic of seismic faulting, an idea suggested originally by Haskell (1964) and considered by Blandford (1975). Because tensile dislocations tend to emit higher P-wave energy than shear faults (Haskell, 1964), normal vibrations on the fault would increase P/S spectral ratios at high frequencies.

Two recent studies (Vernon et al., 1989 and Castro et al., 1989) have examined data specifically to look for high P/S ratios in this context. Castro et al. 1990 found P/S ratios greater than what can be easily explained by attenuation. Figure 3-1 shows several examples of the typical P/S spectral ratios observed in Guerrero, Mexico after correction for Q_r .

The occurrence of tensile faults has been observed in rock mechanic experiments (Reches and Lockner, 1990). Tensile faulting might also occur during the intrusion of magmatic material. Although for real earthquakes the predominant motion on the fault is likely to be purely shear, important tensile contributions or fault-normal vibrations may occur. If this is the case, there must be a relationship between the increase of P/S relative to pure shear faulting and the amount of normal motion on the fault. In this paper we explore simple dislocation models with superimposed normal motions. We study a planar fault in which small normal motions occur during slip. We also analyze the dilatational effect of a fault jog linking strike-slip fault segments. These models provide us with an estimate of the amount of normal motion required to explain the high P/S spectral amplitudes observed in a previous study of earthquakes in the Guerrero subduction zone (Castro et al., 1990).

SENSITIVITY TO SOURCE TIME FUNCTION

We use the formulation of Haskell (1969) and Haskell and Thomson (1972) to calculate the displacement at a point in an infinite space for a homogeneous, isotropic, elastic solid. We evaluate the integrals of Haskell's (1969) equations using Romberg's

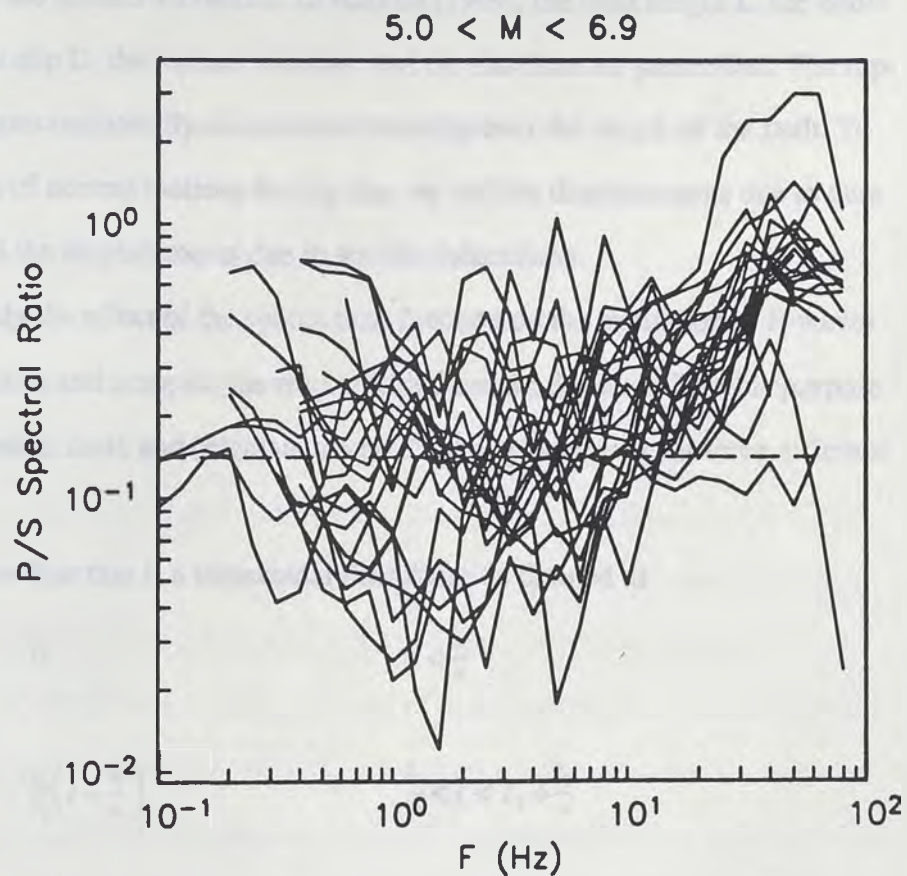


Figure 3-1. Typical P/S spectral amplitudes observed in the Guerrero, Mexico subduction zone after the S-waves were corrected by Q_s . Taken from Castro et al. (1990).

method of integration (e.g. Anderson, 1974; Anderson and Richards, 1975). As in Haskell's formulation the shear displacement on the fault surface is prescribed by a propagating ramp on a rectangular fault. In this paper we also use a trapezoidal time function of dislocation for the normal vibrations. In Haskell (1969), the fault length L , the width W , the permanent slip D , the rupture velocity, and the rise time are prescribed. The rupture front propagates unilaterally at a constant velocity over the length of the fault. To analyze the effect of normal motions during slip, we add the displacements due to pure shear faulting and the displacements due to tensile dislocations.

We first study the effect of the source time function on the excitation of P-waves for pure tensile faults and compare the results with those for S-waves. For this purpose we consider a vertical fault, and calculate the far-field displacements for three different time functions.

The first time function is a trapezoidal time function defined as

$$D_3(\xi_1, t) = \begin{cases} 0 & t < \frac{\xi_1}{v} \\ \frac{D}{T_1} \left(t - \frac{\xi_1}{v} \right) & \frac{\xi_1}{v} < t < T_1 + \frac{\xi_1}{v} \\ D & T_1 + \frac{\xi_1}{v} < t < T_2 + \frac{\xi_1}{v} \\ -\frac{D}{T_1} \left(t - T - \frac{\xi_1}{v} \right) & T_2 + \frac{\xi_1}{v} < t < T + \frac{\xi_1}{v} \\ 0 & T + \frac{\xi_1}{v} < t \end{cases}$$

where T is the duration, $T_1 = T/3$, $T_2 = 2T/3$, D is the amplitude of the normal motion, v the rupture velocity and ξ_1 the distance along the fault from the hypocenter. This time function is used to simulate a tensile fault that opens and closes during the time T . For

all the calculations we use P and S velocities of the medium of $\alpha = 4.5$ Km/sec and $\beta = 2.6$ km/sec, respectively. We make $L = W = 0.6$ km, $T = 0.1$ sec and $D = 1$ cm. Figure 3-2 shows the geometry of the reference system used. The azimuths are defined as the angle measure from the X_1 axis in the counter-clockwise direction. We calculate the P and S-wave displacements for azimuths of 30, 60 and 90 degrees for rupture velocities of 0.9α and 0.9β . We used 130 km for the epicentral distance to be sure we were in the far field.

The second time function used to calculate P and S-wave displacements is a propagating ramp (Haskell and Thomson, 1972), using a rise time of 0.1 seconds and the same geometry and parameters as above. Whereas the first time function does not have a permanent offset, this one does. The "moment" is $\mu L W D$.

The third time function is intended to represent a circular tension crack. For this case the rupture starts at the center of the fault and propagates radially outwards. The radiated energy for P and S-waves for a circular crack has been studied in detail by Walter and Brune (1990). The displacement of the crack is maximal at the center and decreases to zero for $r=c$, where $r = \sqrt{\xi_1^2 + \xi_2^2}$ and c is the radius of the fault. We characterized the spatial variation of this displacement with the function $u(r) = D_c (c^2 - r^2)^{1/2}/c$. This function is the displacement function obtained by Sneddon (1951) for a circular tensile crack. The time history of the rupture was stipulated using ramp functions with variable rise time, $T(r) = \frac{c-r}{\beta} + \frac{c+r}{\alpha}$ so that the final dislocation is

$$D_3(r,t) = \begin{cases} 0 & t < t_r \\ u(r) (t-t_r) / T(r) & t_r < t < t_r + T(r) \\ u(r) & t_r + T(r) < t \end{cases}$$

where $t_r = \frac{r}{\beta}$, and the moment for this case is $\frac{2}{3} \pi \mu D_c c^3$.

Figure 3-3 shows the P wave and Figure 3-4 the S-waves obtained using these source time functions. The displacement at the observation point is proportional to the dis-

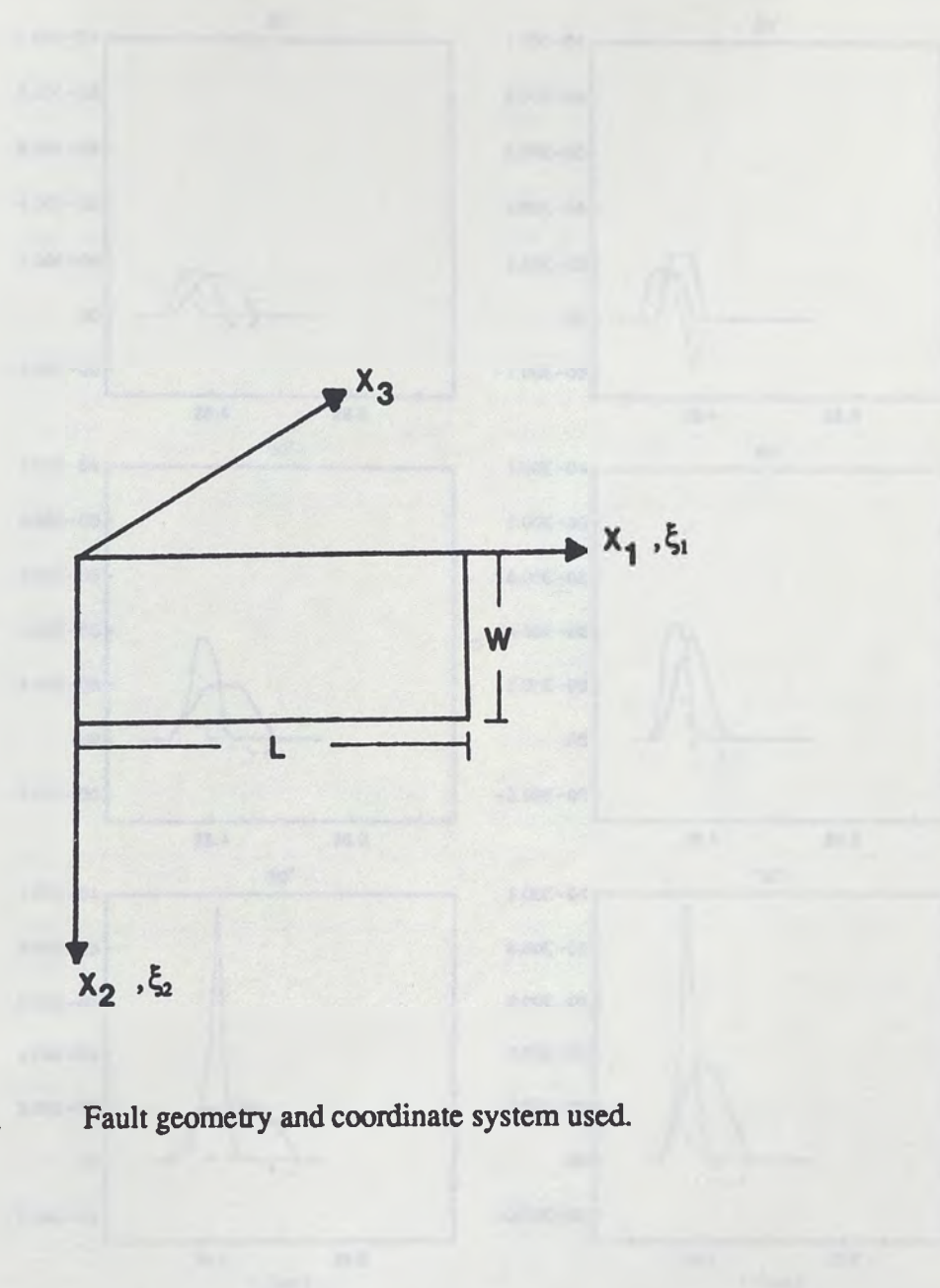


Figure 3-2. Fault geometry and coordinate system used.

Figure 3-3.

The field P-wave displacements from a nearby station, 500 ft from the fault, are shown. The solid line is the observed data, the dashed line is the theoretical response for a crack of width W . The W values on the left were calculated using a rupture velocity of 2.54 km/sec and the velocity on the right is 4.07 km/sec. Only the component with the maximum displacement is shown.

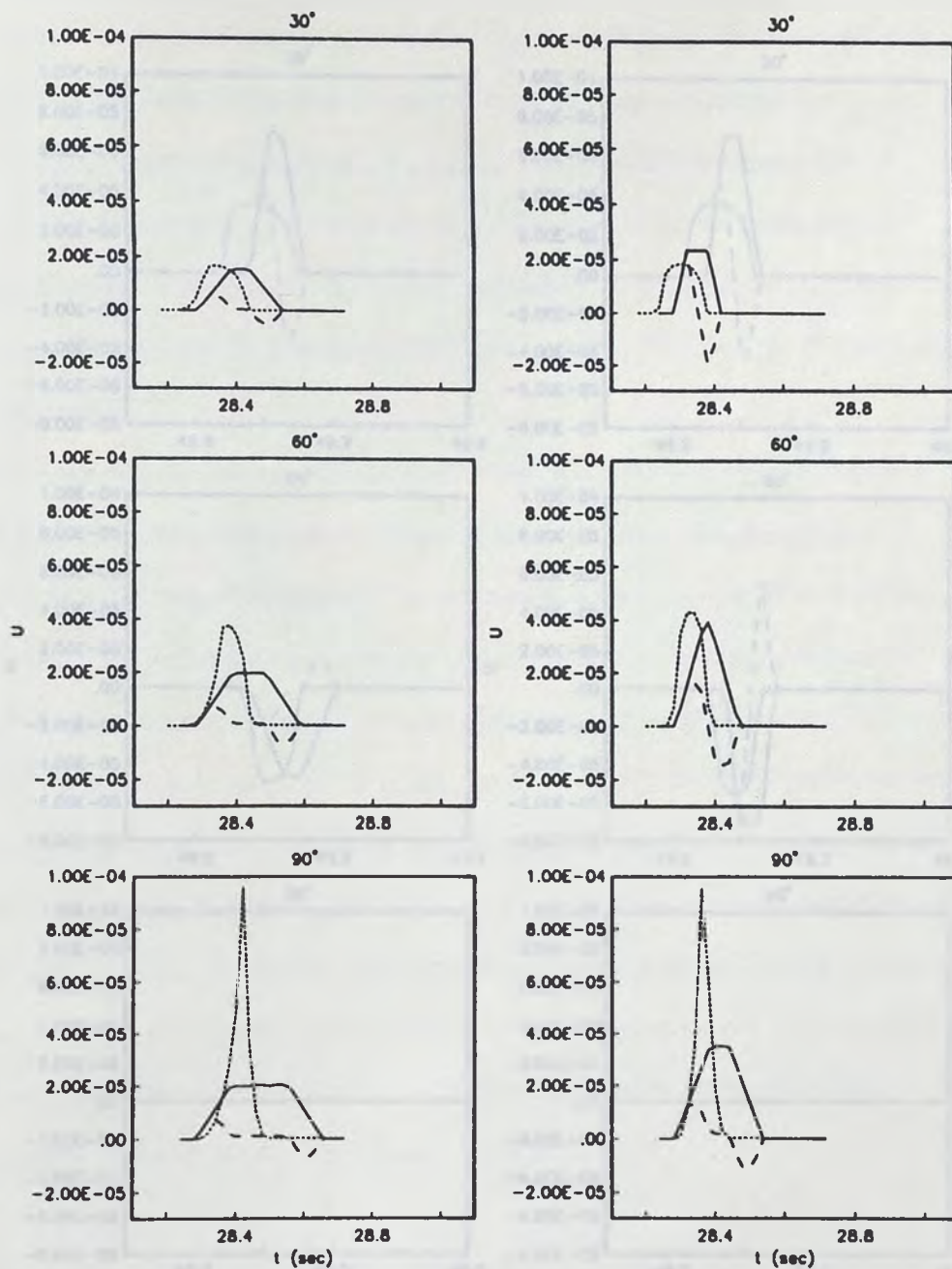


Figure 3-3.

Far-field P-wave displacements from a tensile fault. Solid line when using a ramp function, dashed line for a trapezoidal time function and dotted line for a circular crack. The P-waves on the left were calculated using a rupture velocity of 2.34 km/sec and the waves on the right for 4.05 km/sec. Only the component with the maximum displacement is shown.

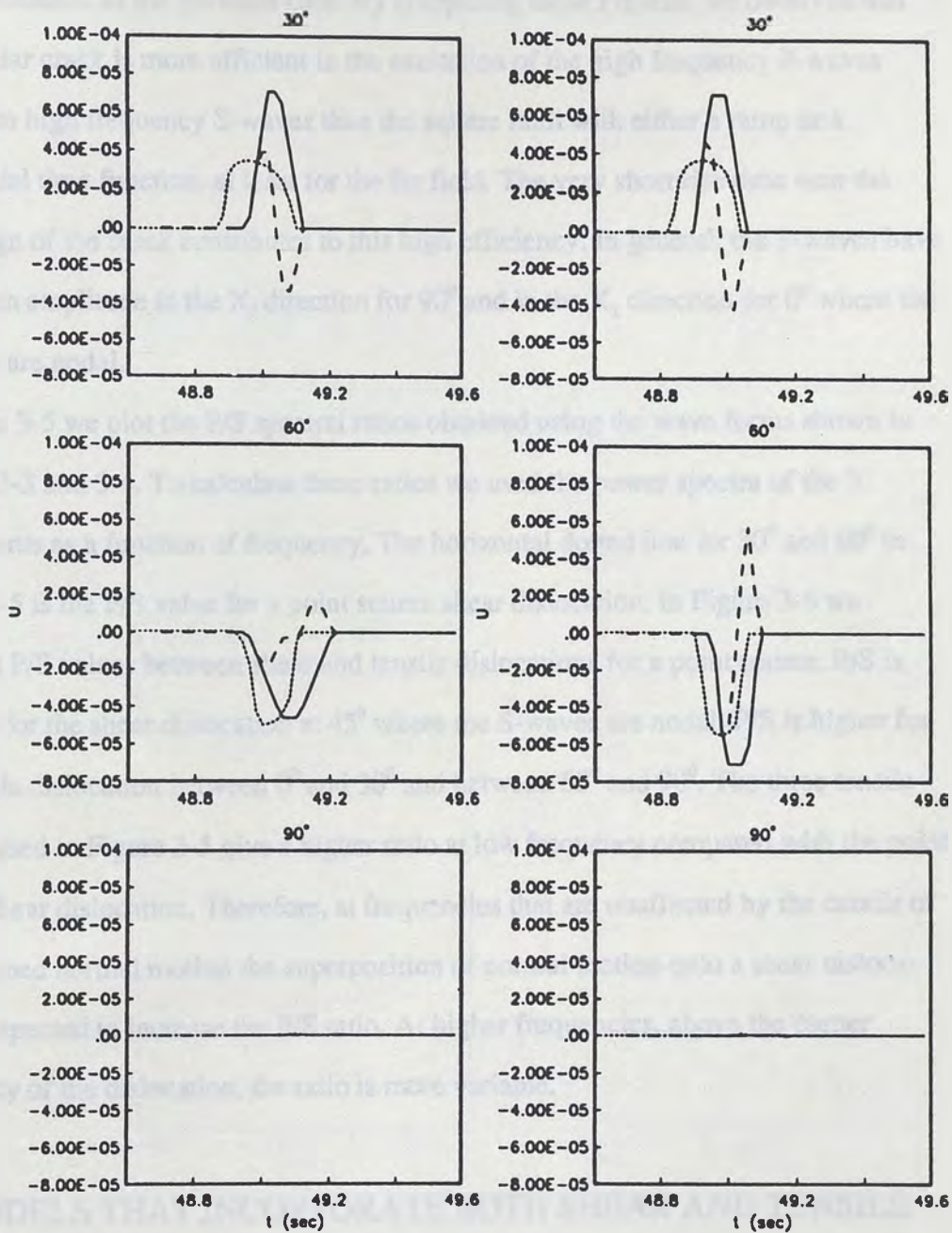


Figure 3-4. Same as in Figure 3-3 but for the S-wave.

Because observations of high P/S spectral ratios (Molnar et al., 1973; Vernon et al., 1982; Castro et al., 1991, and others) suggest that complex source ruptures may

placement and the area of the fault. Thus, to make the comparison in Figures 3-3 and 3-4 meaningful, we normalize the displacement of the circular crack to the same seismic moment as the previous case. By comparing these Figures, we observed that the circular crack is more efficient in the excitation of the high frequency P-waves relative to high frequency S-waves than the square fault with either a ramp or a trapezoidal time function, at least for the far field. The very short rise time near the outer edge of the crack contributes to this high efficiency. In general, the P-waves have maximum amplitude in the X_3 direction for 90° and in the X_1 direction for 0° where the S-waves are nodal.

In Figure 3-5 we plot the P/S spectral ratios obtained using the wave forms shown in Figures 3-3 and 3-4. To calculate these ratios we used the power spectra of the 3 components as a function of frequency. The horizontal dotted line for 30° and 60° in Figure 3-5 is the P/S value for a point source shear dislocation. In Figure 3-6 we compare P/S values between shear and tensile dislocations for a point source. P/S is singular for the shear dislocation at 45° where the S-waves are nodal. P/S is higher for the tensile dislocation between 0° and 30° and between 60° and 90° . The three tensile models used in Figure 3-5 give a higher ratio at low frequency compared with the point source shear dislocation. Therefore, at frequencies that are unaffected by the details of the assumed normal motion the superposition of normal motion onto a shear dislocation is expected to increase the P/S ratio. At higher frequencies, above the corner frequency of the dislocation, the ratio is more variable.

MODELS THAT INCORPORATE BOTH SHEAR AND TENSILE MOTIONS

Because observations of high P/S spectral ratios (Molnar et al., 1973; Vernon et al., 1989; Castro et al., 1991, and others) suggest that complex source ruptures may

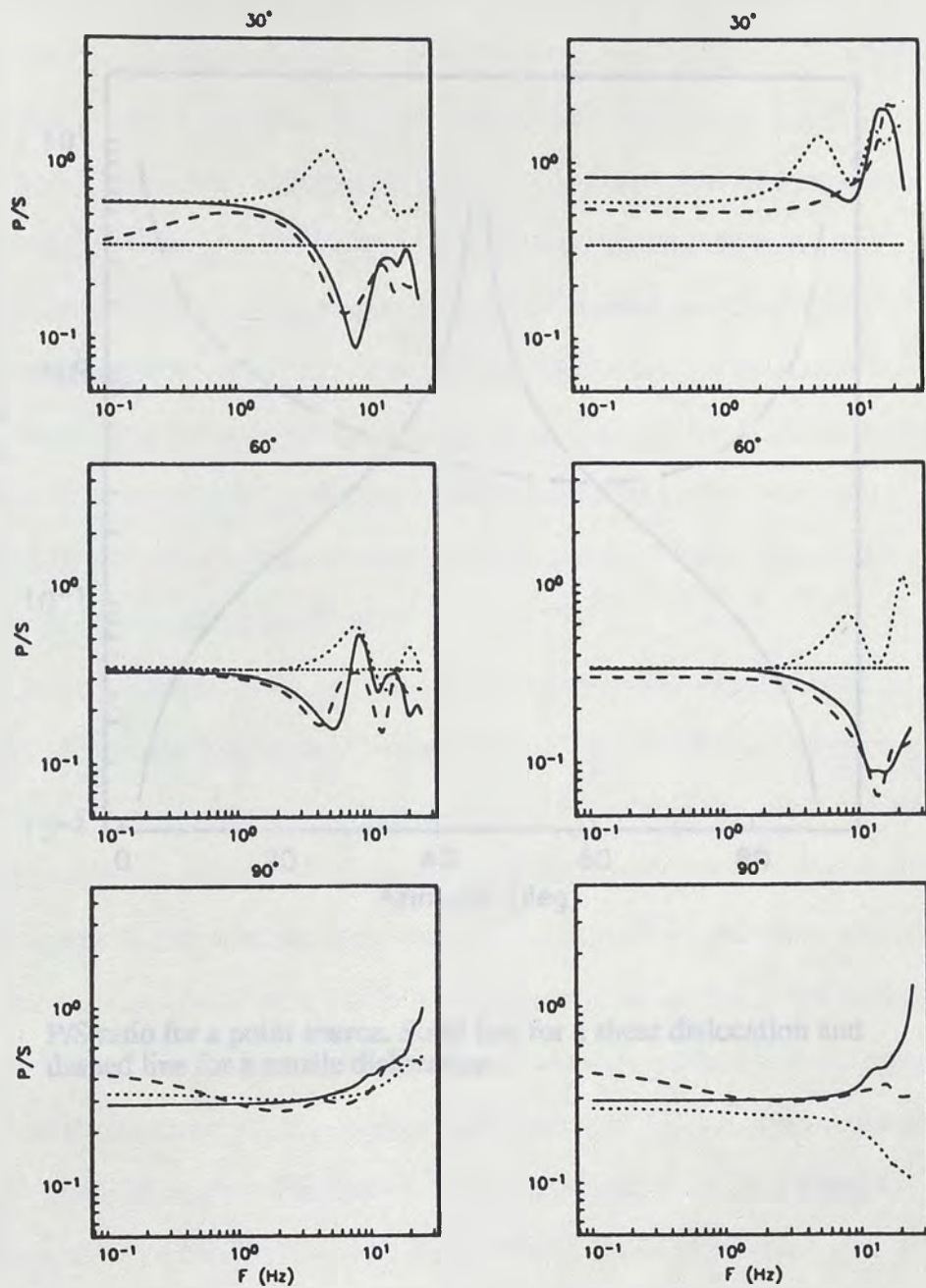


Figure 3-5.

P/S spectral ratios obtained using the wave forms shown on Figures 3-3 and 3-4. The different lines identify the source time functions used as in Figure 3-3.

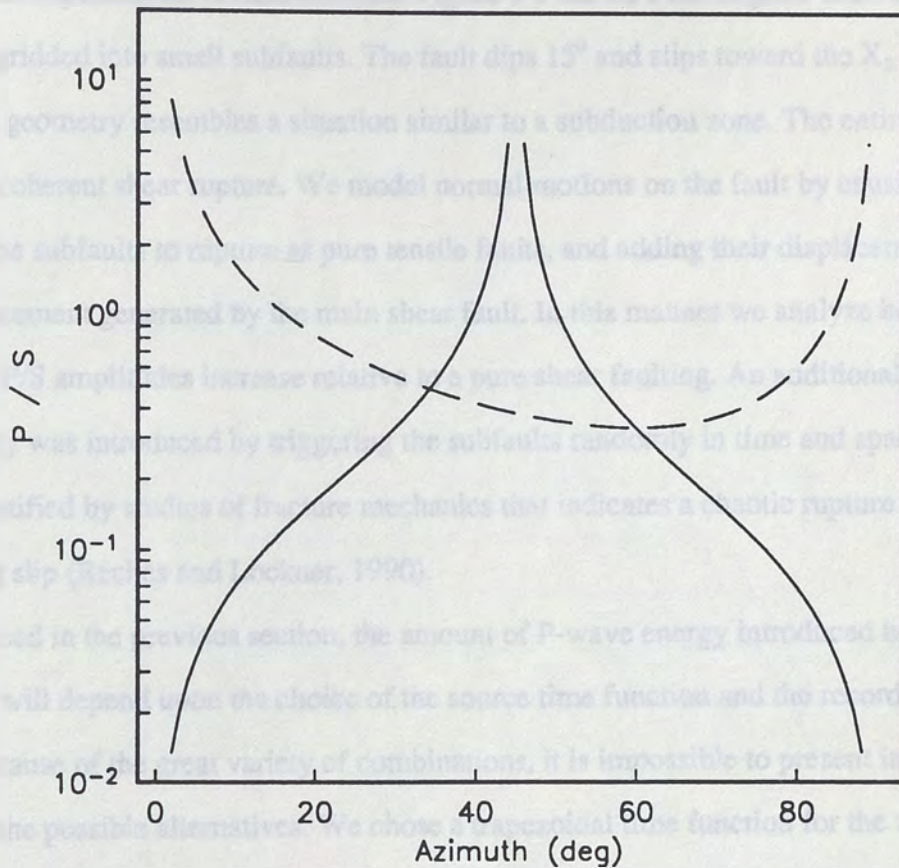


Figure 3-6. P/S ratio for a point source. Solid line for a shear dislocation and dashed line for a tensile dislocation.

need to be modeled using non-pure shear faulting, we explore models that introduce normal vibrations on the fault plane. We consider a planar shear fault containing patches that superimpose normal motions. Figure 3-7 shows a rectangular fault which has been gridded into small subfaults. The fault dips 15° and slips toward the X_3 direction. This geometry resembles a situation similar to a subduction zone. The entire fault slips in a coherent shear rupture. We model normal motions on the fault by causing some of the subfaults to rupture as pure tensile faults, and adding their displacements to the displacement generated by the main shear fault. In this manner we analyze how much the P/S amplitudes increase relative to a pure shear faulting. An additional source complexity was introduced by triggering the subfaults randomly in time and space. This is justified by studies of fracture mechanics that indicates a chaotic rupture behavior during slip (Reches and Lockner, 1990).

As discussed in the previous section, the amount of P-wave energy introduced by the subfaults will depend upon the choice of the source time function and the recording azimuth. Because of the great variety of combinations, it is impossible to present in this paper all the possible alternatives. We chose a trapezoidal time function for the tensile subfaults and a ramp function for the shear fault. Thus, although we introduce normal vibrations during the rupture process, the fault will not open permanently. We used a fault length of 3 Km and a width of 1 km and divided it into 21 subfaults. We calculated P and S-wave displacements for an epicentral distance of 130 km and an azimuth of 60° . We calculated the body-wave displacements of the main shear fault using a ramp function with two seconds of rise time and final dislocation of 10 cm. Figure 3-8 shows the P and S-waves obtained before the addition of the tensile subfaults. Each of the subfault displacements were obtained using a trapezoidal function with 0.5 seconds duration and maximum amplitude of 1 cm. Figure 3-9 shows the body-wave displacements obtained for three of the subfaults (note the shorter time scale). We add to the displacements shown in Figure 3-8 the displacements of the tensile faults. 21 random

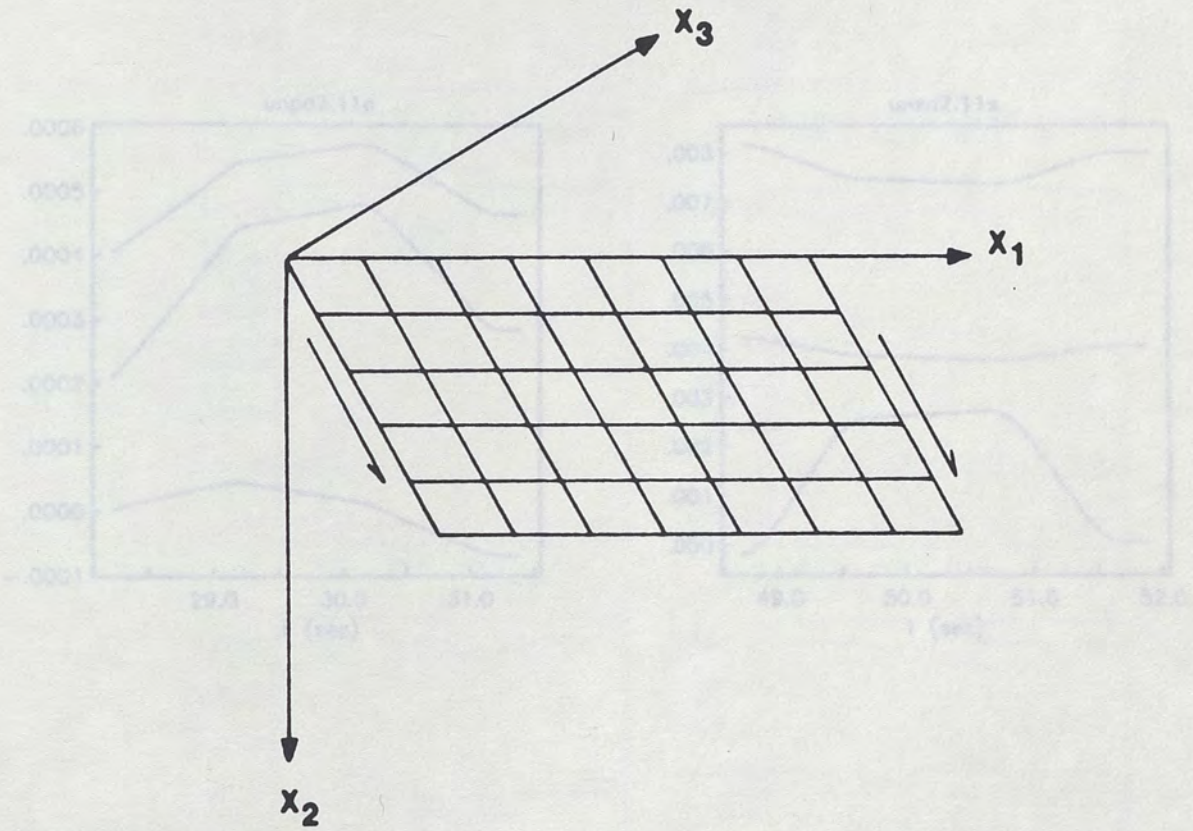


Figure 3-8. Body wave displacements from a pure shear rectangular fault. The left frame for P and the right for the S-wave. A ramp with 2.0 seconds of rise time and 10 cm of final distortion was used.

Figure 3-7. Fault plane geometry.

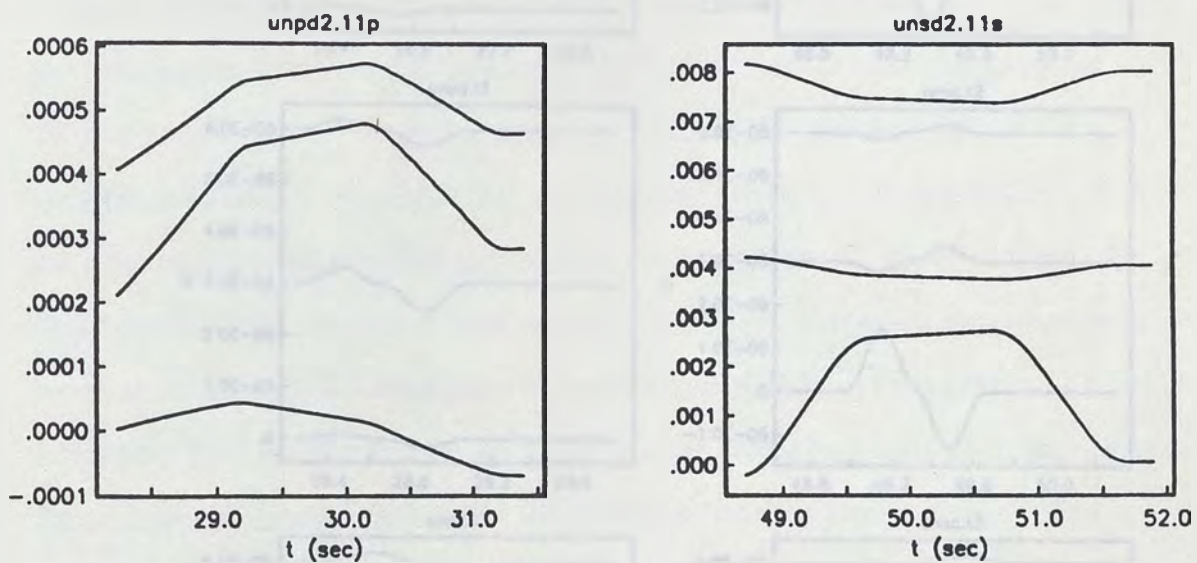


Figure 3-8. Body wave displacements from a pure shear rectangular fault. The left frame for P and the right for the S-wave. A ramp with 2.0 seconds of rise time and 10 cm of final dislocation was used.

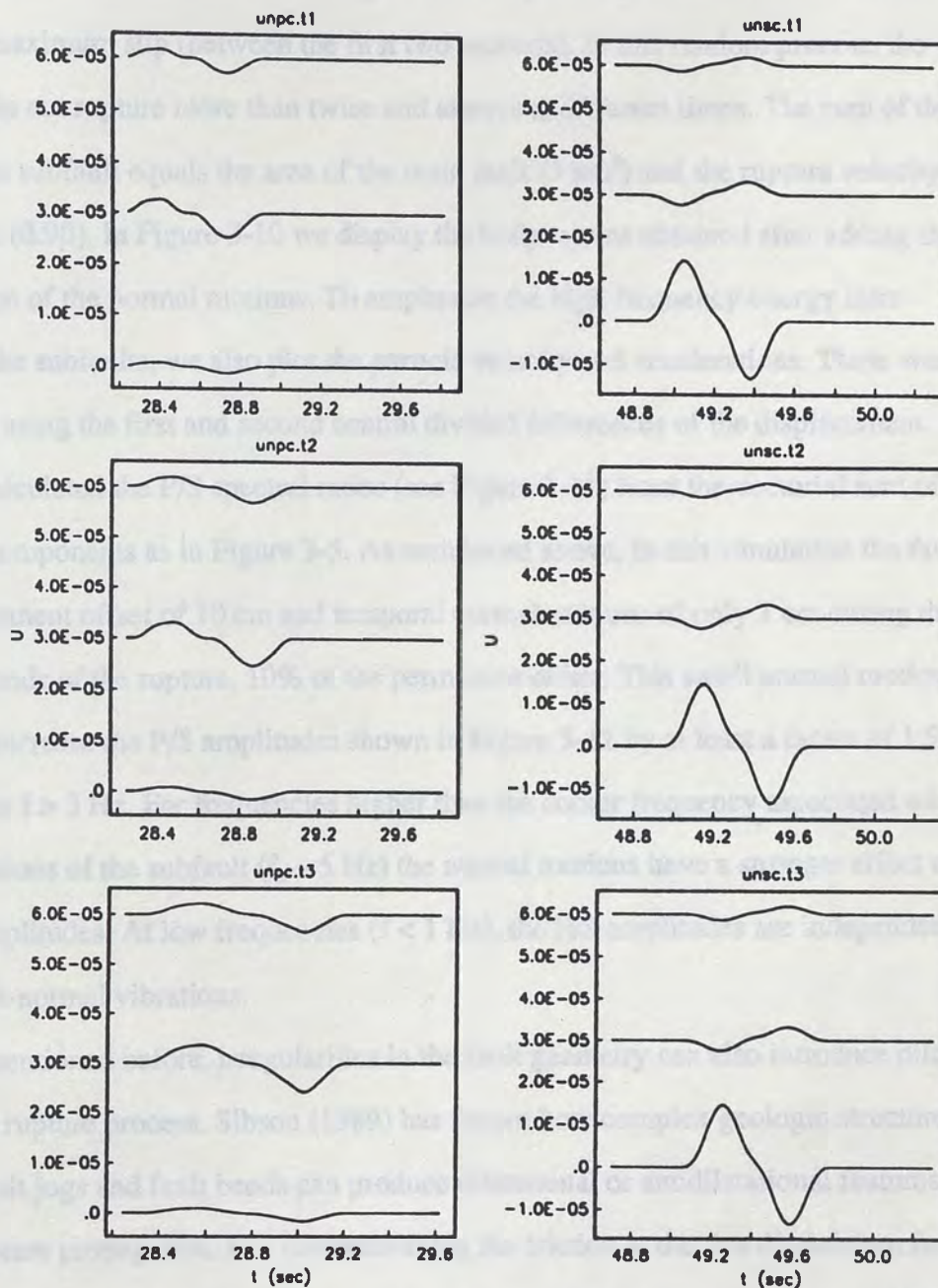


Figure 3-9. P and S-wave displacements (left and right frames, respectively) from 3 of the 21 tensile subfaults.

subfaults were used in the addition along with random starting time. We restricted the trigger time of the subfaults to be during the time required by the main shear fault to reach the maximum slip (between the first two seconds). In this random process, the subfaults do not rupture more than twice and always at different times. The sum of the areas of the subfault equals the area of the main fault (3 km^2) and the rupture velocity is 2.3 km/sec (0.9β). In Figure 3-10 we display the body-waves obtained after adding the contribution of the normal motions. To emphasize the high frequency energy introduced by the subfaults, we also plot the particle velocity and accelerations. These were calculated using the first and second central divided differences of the displacement. We also calculated the P/S spectral ratios (see Figure 3-11) from the vectorial sum of the three components as in Figure 3-5. As mentioned above, in this simulation the fault has a permanent offset of 10 cm and temporal normal motions of only 1 cm during the first 2 seconds of the rupture, 10% of the permanent offset. This small normal motions, however, increase the P/S amplitudes shown in Figure 3-11 by at least a factor of 1.5 at frequencies $f > 3 \text{ Hz}$. For frequencies higher than the corner frequency associated with the dimensions of the subfault ($f_c \sim 5 \text{ Hz}$) the normal motions have a stronger effect on the P/S amplitudes. At low frequencies ($f < 1 \text{ Hz}$), the P/S amplitudes are independent of the fault-normal vibrations.

As mentioned before, irregularities in the fault geometry can also introduce dilatation in the rupture process. Sibson (1989) has shown how complex geologic structures such as fault jogs and fault bends can produce dilatational or antidilatational features during rupture propagation. In a dilatational jog the friction at the tips diminishes, facilitating sliding so that the slip can be transferred along the fault system. Sibson (1985), however, also points out that for several recent earthquakes the rupture has stopped near a large dilatational jog. We nevertheless analyze how a dilatational jog may introduce additional P-wave energy in the particle displacements when the slip is transferred from one section of the fault to another.

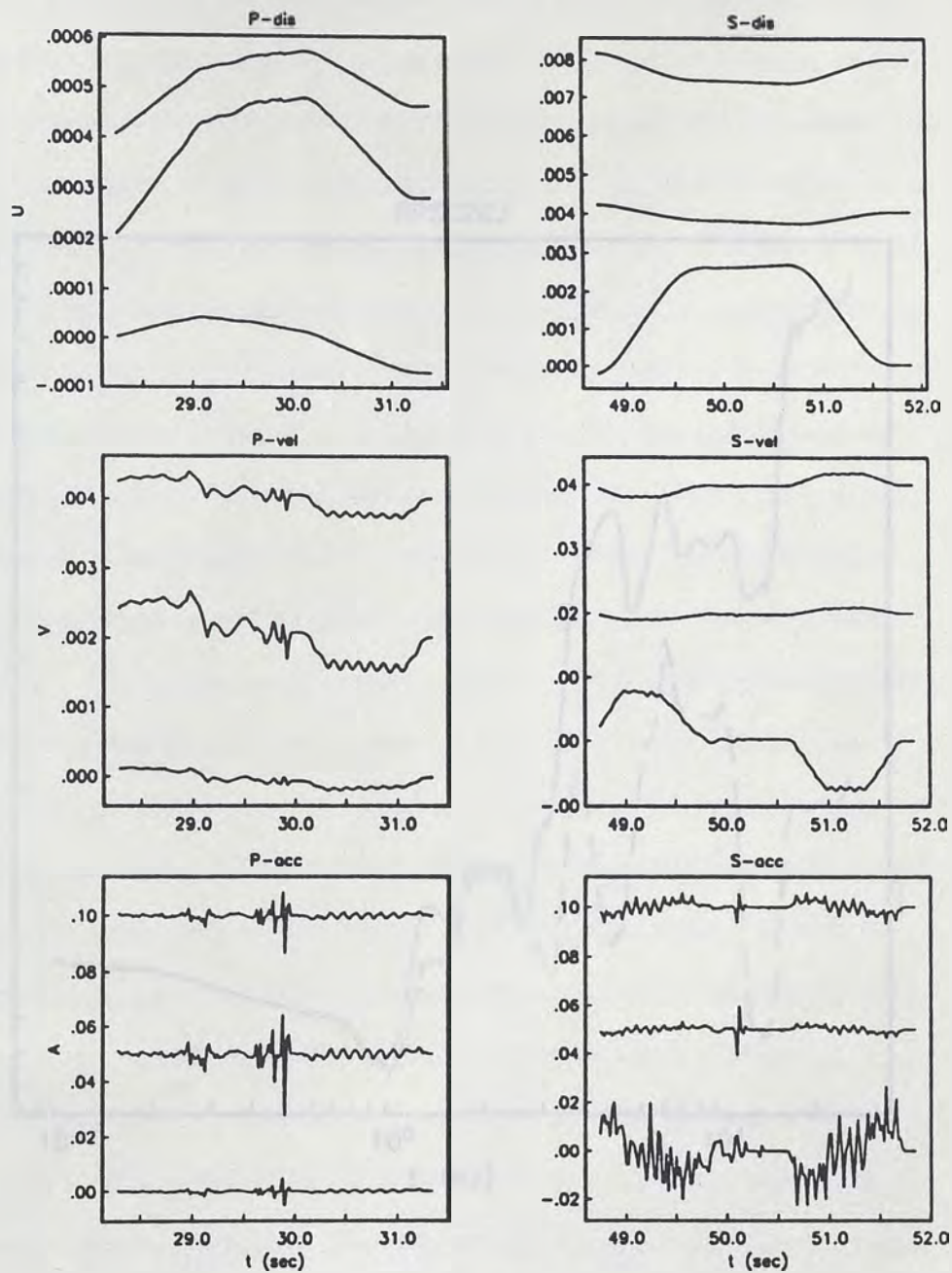


Figure 3-10.

Displacement, velocity and acceleration obtained after adding the contribution of the tensile subfaults.

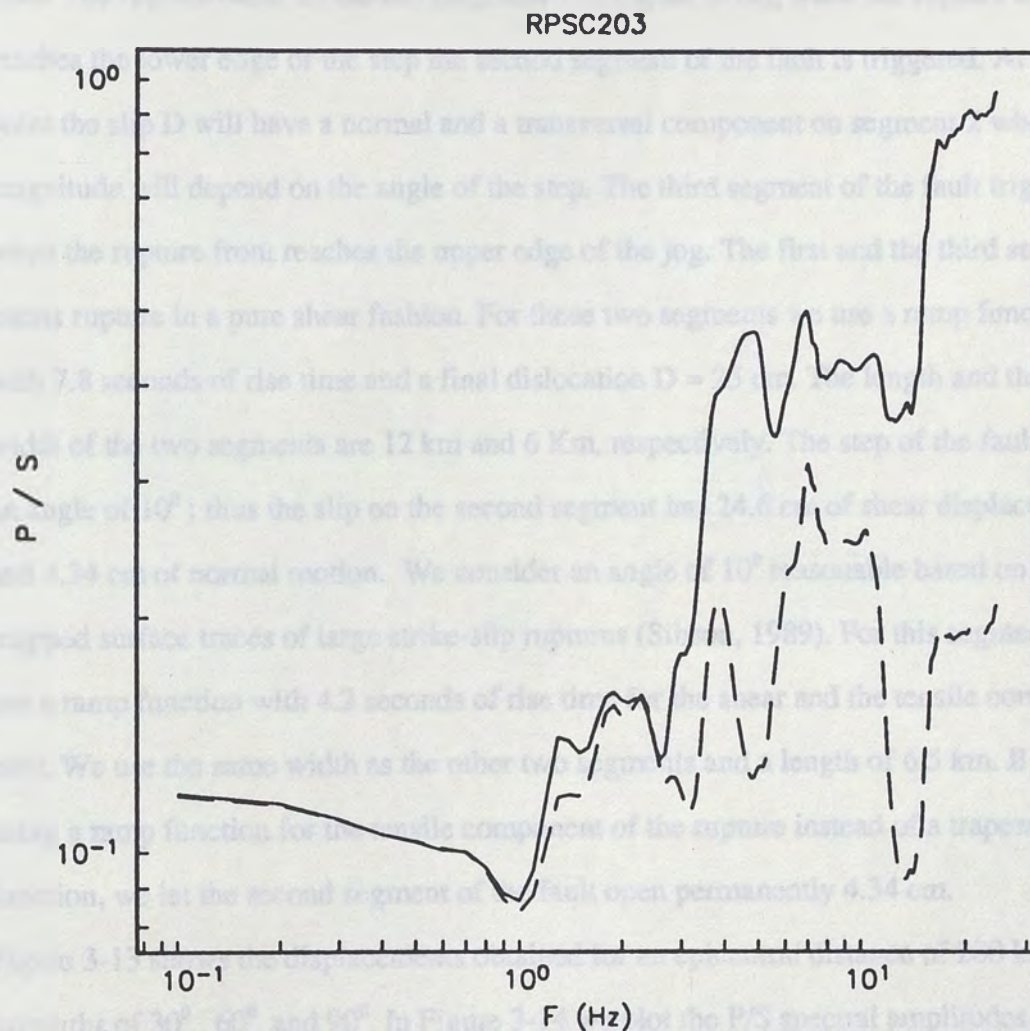


Figure 3-11. P/S spectral amplitudes calculated from the displacements displayed in Figure 3-9. The dashed line is the spectral ratio for the pure shear displacement (see also Figure 3-8).

Figure 3-12 shows a strike-slip system of faults like those described by Sibson (1985, 1989), that is, a dilatational jog consisting of a left step under left-lateral shear. We assume that the three segments of the system rupture in a progressive manner so that the total body-wave displacement consists of the contribution of the 3 segments of the fault. The rupture starts on the left (segment 1 in Figure 3-12); when the rupture front reaches the lower edge of the step the second segment of the fault is triggered. At this point the slip D will have a normal and a transversal component on segment 2 whose magnitude will depend on the angle of the step. The third segment of the fault triggers when the rupture front reaches the upper edge of the jog. The first and the third segments rupture in a pure shear fashion. For these two segments we use a ramp function with 7.8 seconds of rise time and a final dislocation $D = 25$ cm. The length and the width of the two segments are 12 km and 6 Km, respectively. The step of the fault has an angle of 10° ; thus the slip on the second segment has 24.6 cm of shear displacement and 4.34 cm of normal motion. We consider an angle of 10° reasonable based on mapped surface traces of large strike-slip ruptures (Sibson, 1989). For this segment we use a ramp function with 4.2 seconds of rise time for the shear and the tensile component. We use the same width as the other two segments and a length of 6.5 km. By using a ramp function for the tensile component of the rupture instead of a trapezoidal function, we let the second segment of the fault open permanently 4.34 cm.

Figure 3-13 shows the displacements obtained for an epicentral distance of 200 km and azimuths of 30° , 60° and 90° . In Figure 3-14 we plot the P/S spectral amplitudes obtained using the vectorial sum of the 3 components. We also test the case in which the second segment of the fault opens and closes in the 4.2 sec interval by using a trapezoidal function. Figure 3-15 shows the P/S spectral amplitudes obtained for this case. For both cases, the P/S amplitudes are independent of the fault normal motion at frequencies lower than the corner frequency of the dilatational jog ($f_c \sim 0.3$ Hz). In Figures 3-14 and 3-15 we also plot the P/S amplitudes obtained from a planar pure-shear

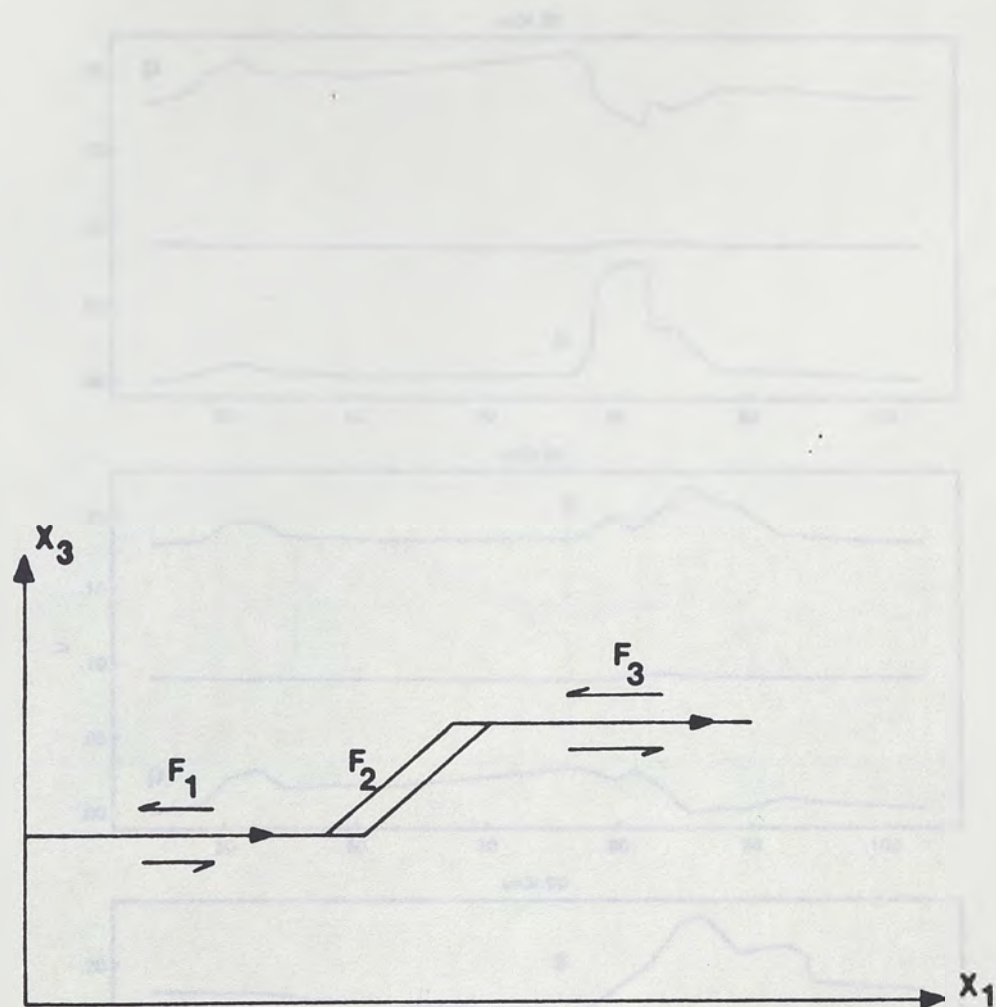


Figure 3-12. Cartoon of a dilatational jog on a left-lateral strike-slip fault (modified from Sibson, 1989). The rupture propagates from left to right.

Figure 3-11. Seislogram displacements obtained from the fault system shown in Figure 3-12. Top for an azimuth of 30° , middle for 60° and on the bottom for 90° and an epicentral distance of 300 km. A ramp function was used for the three segments of the fault.

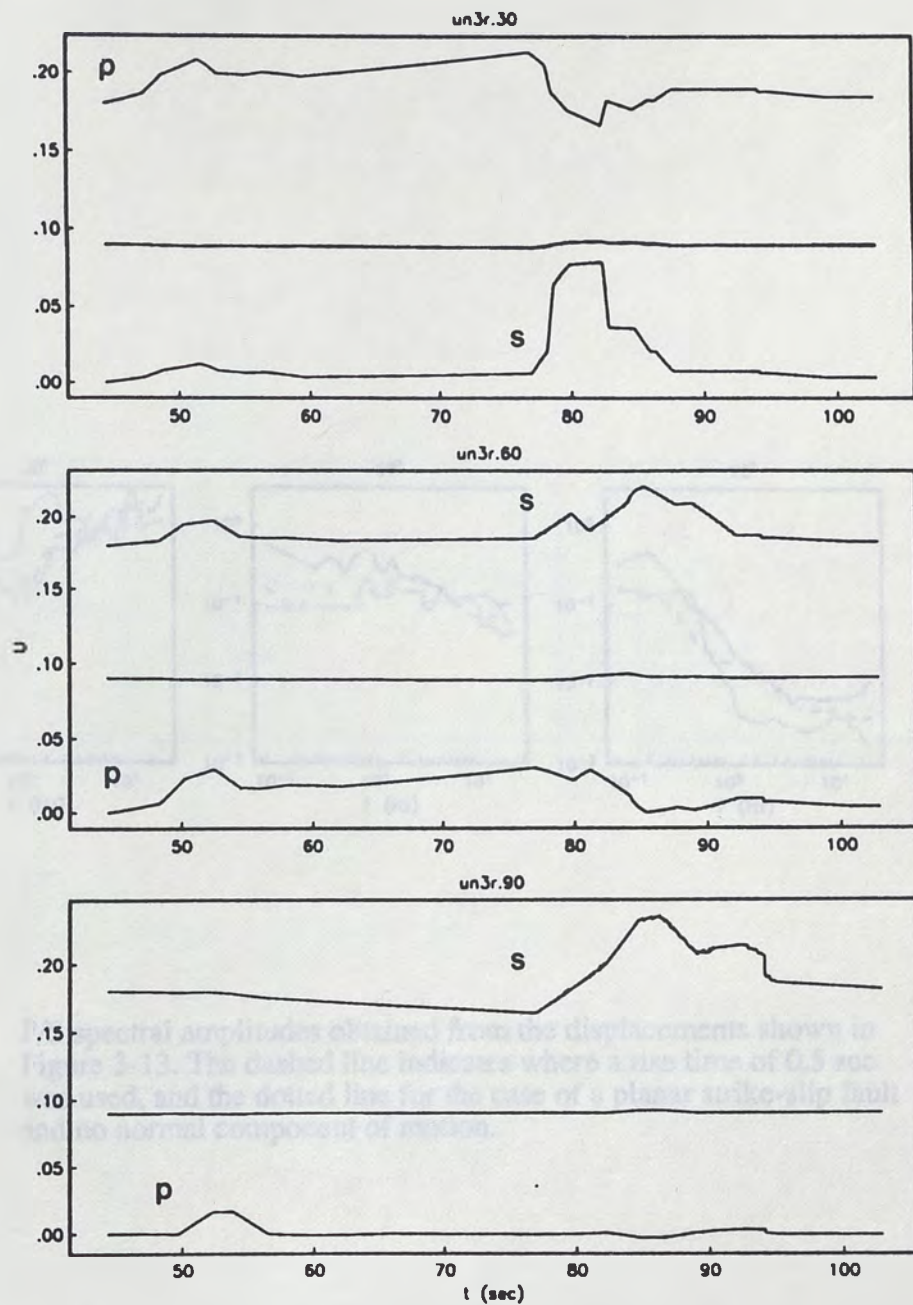


Figure 3-13. Body-wave displacements obtained from the fault system shown in Figure 3-12. Top for an azimuth of 30° , middle for 60° and on the bottom for 90° and an epicentral distance of 200 km. A ramp function was used for the three segments of the fault.

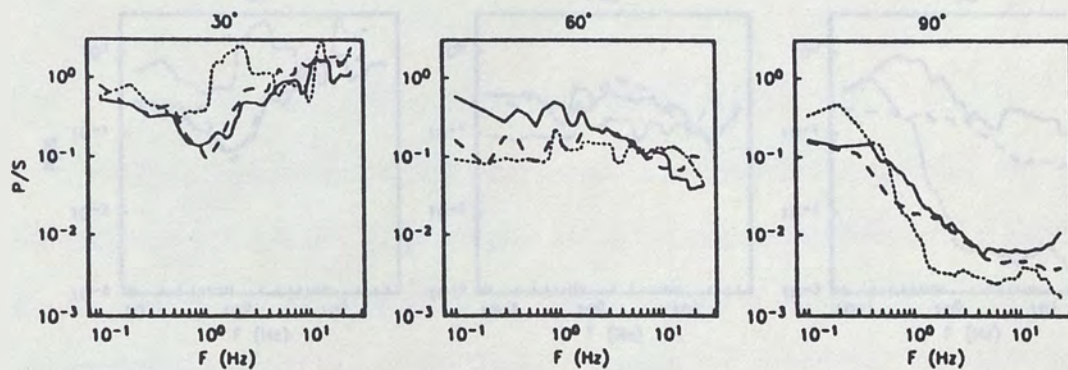


Figure 3-14. P/S spectral amplitudes obtained from the displacements shown in Figure 3-13. The dashed line indicates where a rise time of 0.5 sec was used, and the dotted line for the case of a planar strike-slip fault and no normal component of motion.

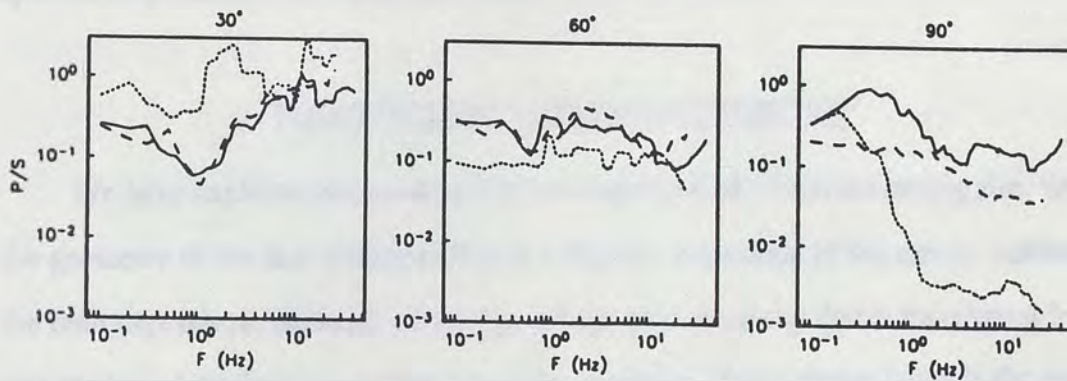


Figure 3-15. Same as Figure 3-14 but P/S spectral amplitudes obtained using a trapezoidal time function for the second segment of the fault shown in Figure 3-12.

fault with a length of 30.5 km and a width of 6 km. We generate the P- and S-waves using a ramp function with a rise time of 7.8 sec and a permanent offset of 25 cm. The rise time used in the above calculations are consistent with the rupture duration, however, dislocation time histories obtained from recent studies of earthquakes (Heaton, 1989) suggest that slip-pulse models may be more adequate. We test this model by using a rise time of 0.5 seconds for the ramp functions and the duration of the trapezoidal function used to model the system of faults shown in Figure 3-12. We keep the same values for the other parameters. Figures 3-14 and 3-15 also show the P/S spectral amplitudes obtained for this case.

DISCUSSION AND CONCLUSIONS

We have explored two models that introduce normal vibrations during slip. When the geometry of the fault changes (Figure 3-12), the magnitude of the motion normal to the fault depends on the angle of the jog and the amount of slip that is transferred from one section of the fault to another. Thus, the geometry of non-planar faults is the main physical constrain on the amount of normal motion on the fault. In both models, however, the amplitudes of the body-waves will depend on the source time function chosen (see Figures 3-3 and 3-4). To simulate the opening and closing of the fault, we selected a trapezoidal time function to model the tensile component of faulting for the models considered in this paper. As it turns out, this time function is not the most efficient way to excite P relative to S-waves. However, by using this function we establish an upper limit on the magnitude of the normal motions on the fault required to explain P/S spectral amplitudes observed in previous studies (Castro et al., 1990). For the planar-fault model (Figure 3-7), normal motions of 10 % of the slip on the fault increase the P/S amplitudes from a factor of 1.5 at 3 Hz to a factor of 4.7 at 25 Hz (see Figure 3-11). For this model, the subfaults also introduce complexity into the S-waves as can be seen

from the accelerations shown in Figure 3-10. However, the excitation of P-waves at high frequencies ($f > 1$ Hz) is more efficient for a tensile rupture; thus, P/S tends to increase with frequency.

For the non-planar model (Figure 3-12), a jog with an angle of 10° introduces a normal component of 18 % of the slip on the fault. In this model, however, the area of the jog represents only 20 % of the area of the whole system. In Figures 3-14 and 3-15 we compare the P/S spectral amplitudes between this model and a planar pure-shear fault with same rupture area. At 30° the S-waves for the pure-shear fault are close to the node while at 90° the P-waves are nodal. Thus, P/S is high for 30° and low for 90° . When the fault opens and closes (Figure 3-15) P/S is higher than when opens permanently (Figure 3-14) for 60° and 90° . For intermediate azimuths ($\sim 60^\circ$), the P/S values shown in Figure 3-15 increase by a factor of 1.9 between 1 Hz and 10 Hz relative to the planar model. This indicates that the near and intermediate field terms for the trapezoidal time function introduce more P-wave energy relative to S-wave than the ramp time function. We also observed in Figures 3-14 and 3-15 that a source with a rise time shorter than the overall rupture duration tends to give higher P/S amplitudes for azimuths between 30° and 60° and smaller for an azimuth of 90° .

Based on the geometry of mapped surface traces of earthquake ruptures (Sibson, 1989), a fault normal motion of 18 % of the slip on the fault is plausible. This introduce additional P-wave energy in the particle motions that explain the high P/S spectral amplitudes observed in previous studies (Castro et al., 1990). For a planar fault, normal vibrations of only 10 % of the slip also give P/S amplitudes consistent with the observations. It is clear from Figures 3-5, 3-14 and 3-15 that for an homogeneous full space the radiation pattern plays an important role on the P/S spectral amplitudes. For the real earth, the elastic properties of the medium changes laterally and with depth. It

is likely that at high frequencies, the scattering may tend to average the radiation pattern. Thus, any conclusion from this study must be based on the overall values obtained.

- LITTLE, A. (1971) A study of the growth of the Pacific oyster, *Crassostrea gigas*, in the Pacific Northwest. *J. Geophys. Res.*, **76**, 471-480.
- MARSHALL, N.A. and P. SUTHERLAND (1977) Distribution of water bodies from aerial reconnaissance. *Geophys. J. R. astr. Soc.*, **91**, 347-373.
- MARSHALL, N.A., P. SUTHERLAND, J.W. BROWN, J. PROSS, S.B. FAIRBANKS, R. QUINN and H. GIBSON (1980) Using ground waves from the Northwest. *Microseismicity: Sources*, **23**, 1043-1048.
- MARSHALL, N.A. (1980) Microseismicity from the Pacific Northwest. *J. Geophys. Res.*, in press.
- MARSHALL, N.A. (1973) A study of the growth of the Pacific oyster, *Crassostrea gigas*, in the Pacific Northwest. *J. Geophys. Res.*, **78**, 1485-1492.
- MARSHALL, N.A., P.A. HARRIS and D. BROWN (1980) Characteristics of the Pacific oyster, *Crassostrea gigas*, in the Pacific Northwest. *J. Geophys. Res.*, **85**, 25.
- MARSHALL, N.A., J.D. ANDERSON and J.H. BRUCE (1981) TSS spectral index estimates from microseismicity. *Mar. Geol.*, in press.
- CHAPMAN, G.L. and BOURWRIGHT (1980) The growth and size distribution of the Pacific oyster, *Crassostrea gigas*, in the Northwest Territories, Canada. *Mar. Geol.*, **35**, 167-182.
- MARSHALL, N.A. (1984) Total energy and energy spectral density of steady wave radiating from propagating fronts. *Mar. Geol.*, **54**, 341-355.
- MARSHALL, N.A. (1985) Energy characteristics of the wave field of a propagating front. *Mar. Geol.*, **59**, 345-352.
- MARSHALL, N.A. and J.C. HARRIS (1977) Microseismic noise field of a steady propagating wave front. *Mar. Geol.*, **62**, 373-397.
- HARRIS, J.C. (1980) Evidence for the importance of wave heading patterns of the microseismic energy spectrum.
- HARRIS, J.C. and G.E. GIBSON (1972) Seismological aspects of the California earthquake of February 4, 1970. *J. Geophys. Res.*, **77**, 3427-3436.
- FRANCOISE, A. and R. M. (1981) A quantitative method for the determination of microseismicity sources and its application to the Pacific Northwest. *Mar. Geol.*, **39**, 305-322.
- MARSHALL, N.A. and D. ANDERSON (1980) The occurrence and growth of Pacific oysters, *Crassostrea gigas*, in the Pacific Northwest. *Science*, in press.
- MARSHALL, N.A. and H. GIBSON (1981) Studies of high frequency microseismicity, tides, deep, and wind energy systems. *J. Geophys. Res.*, **86**, 4705-4720.

REFERENCES

- Anderson, J. (1974). A dislocation model for the Parkfield earthquake, *Bull. Seism. Soc. Am.*, 64, 671-686.
- Anderson, J.G. and P.G. Richards (1975). Comparison of strong motion from several dislocation models, *Geophys. J. R. astr. Soc.*, 42, 347-373.
- Anderson, J.G., P. Bodin, J.N. Brune, J. Prince, S.K. Singh, R. Quaas, and M. Onate (1986). Strong ground motion from the Michoacan, Mexico earthquake, *Science*, 233, 1043-1049.
- Andrews, D.J. (1989). Mechanics of fault junctions, *J. Geophys. Res.*, 94, 9389-9397.
- Blandford, R.R. (1975). A source theory for complex earthquakes, *Bull. Seism. Soc. Am.*, 65, 1385-1405.
- Brune, J.N., P.A. Johnson and C. Slater (1989). Constitutive relations for foam rubber stick-slip, *Seis. Res. Lett.* 60, 26.
- Castro, R.R., J.G. Anderson, and J.N. Brune (1991). P/S spectral ratios from the Guerrero accelerograph array, *Bull. Seism. Soc. Am.*, Submitted.
- Choy, G.L., and Boatwright (1988). Teleseismic and near-field analysis of the Nahanni earthquakes in the Northwest Territories, Canada, *Bull. Seism. Soc. Am.*, 78, 1627-1652.
- Haskell, N.A. (1964). Total energy and energy spectral density of elastic wave radiation from propagating faults, *Bull. Seism. Soc. Am.*, 54, 1811-1841.
- Haskell, N.A. (1969). Elastic displacements in the near-field of a propagating fault, *Bull. Seism. Soc. Am.*, 59, 865-908.
- Haskell, N.A. and K.C. Thomson (1972). Elastodynamic near-field of a finite, propagating tensile fault, *Bull. Seism. Soc. Am.*, 62, 675-697.
- Heaton, T.H. (1989). Evidence for and implications of self-healing pulses of slip in earthquake rupture, submitted
- Kanamori, H. and G.S. Stewart (1978). Seismological aspects of the Guatemala earthquake of February 4, 1976, *J. Geophys. Res.*, 83, 3427-3434.
- Papageorgiou, A. and K. Aki (1983). A specific barrier model for the quantitative description of inhomogeneous faulting and the prediction of strong ground motion. Part I. Description of the model, *Bull. Seism. Soc. Am.* 73, 693-722.
- Reches, Z., and D. Lockner (1990). The nucleation and growth of faults in brittle rocks, *Science*, submitted.
- Rudnicki, J.W., and H. Kanamori (1981). Effects of fault interaction on moment, stress drop, and strain energy release, *J. Geophys. Res.*, 86, 1785-1793.

- Sibson, R.H. (1985). Stopping of earthquake ruptures at dilatational fault jogs, *Nature*, 316, 248-251.
- Sibson, R.H. (1989). Earthquake faulting as a structural process, *J. Struct. Geol.*, 11, 1-14.
- Singh, S.K., T. Dominguez, R. Castro, and M. Rodriguez (1984). P waveform of large, shallow earthquakes along the Mexican subduction zone, *Bull. Seism. Soc. Am.* 74, 2134-2156.
- Sneddon, I.N. (1951). *Fourier Transforms*, in *International Series in Pure and Applied Mathematics*, McGraw-Hill book Company.
- Trifunac, M. and J.N. Brune (1970). Complexity of energy release during the Imperial Valley, California, earthquake of 1940, *Bull. Seism. Soc. Am.*, 60, 137-160.
- Vernon, F., J.N. Brune, and J. Fletcher (1989). P/S spectral ratios for the Anza array: Evidence for normal motions during fault rupture, *Trans. Am. Geoph. Union*, 70, 1226.
- Walter and Brune (1991). The spectra of seismic radiation from a tensile crack, submitted.
- Wyss, M. and J.N. Brune (1967). The Alaska earthquake of 28 March 1964: A complex multiple rupture, *Bull. Seism. Soc. Am.* 57, 1017-1023.

APPENDIX A

The attenuation model, Equation (1-1) in the text, e.g.

$$D_i(f,r) = M_i A(f,r) \quad (\text{A-1})$$

is linearized by taking logarithms at both sides of the equation. Then (A-1) for a fix frequency f can be rewritten as

$$d_{ij} = m_i + a_j \quad (\text{A-2})$$

where $d_{ij} = \text{Log } D_i(f,r)$ is the spectral amplitude from event i at distance j , $m_i = \text{Log } M_i$ is the scalar for event i and $a_j = \text{Log } A(f,r)$ the attenuation at distance j .

In matrix form, Equation (A-2) is

$$\Gamma \mathbf{x} = \mathbf{b} \quad (\text{A-3})$$

where \mathbf{b} is the data vector containing the elements d_{ij} (the subscripts only identify the origin of the data), \mathbf{x} is the solution vector containing the model parameters m_i and a_j and the elements of Γ are illustrated in Figure A-1. The smoothing constrain is also included on Γ .

The weighting factors w_1 and w_2 are used to constrain $a_1=0$ at $r=0$ and to weight the second derivative respectively. In practice w_2 is varied in multiple runs, and an optimal choice is selected by visual examination of the solution.

For the case of the parametric model, Equation (1-6) in the text can be rewritten as

$$d_{ij} = s_i + z_j + t \quad (\text{A-4})$$

where $d_{ij} = \text{Log } D_{ij}(f,r) - \text{Log } G(r)$ is the spectral amplitude from event i at site j after the geometrical spreading correction, $s_i = \text{Log } S_i(f)$, $z_j = \text{Log } Z_j(f)$ and $t = -\pi fr/\beta Q \text{Log } e$. Equation (A-4) in matrix form becomes:

$$\Gamma \mathbf{x} = \mathbf{b} \quad (\text{A-5})$$

where now no smoothness constraints are needed because of the assumed distance dependence.

The system of equations (A-3) and (A-5) is solved for 26 frequencies between 0.1 and 40 Hz using a least-squares inversion (Menke, 1984). The solution is given by

$$\mathbf{x} = (\Gamma^T \Gamma)^{-1} \Gamma^T \mathbf{d}$$

(A-6)

APPENDIX B

Haskell (1964) derived expressions for the spectral energy density radiated by point sources over a fault plane. In his model the fault is assumed to be rectangular and propagates at a constant velocity in the direction of the length L . The slip occurs simultaneously across the width of the fault W .

For a longitudinal shear fault the spectral energy density (Haskell, 1964, equations 45 and 46) is given by:

$$E_p(\omega)^L = (\rho W^2 L^2 D^2 / 2\pi\beta) (\beta/\alpha)^5 |\hat{G}(\omega)|^2 B_1(\omega) \quad (\text{B-1})$$

$$E_s(\omega)^L = (\rho W^2 L^2 D^2 / 2\pi\beta) |\hat{G}(\omega)|^2 B_2(\omega) \quad (\text{B-2})$$

where ρ is the density, α and β the P- and S-wave velocities, respectively, $G(\omega)$ the acceleration spectra of the time function, and $B_1(\omega)$ and $B_2(\omega)$ (Haskell, 1964 equations 47 and 48) are the integrals that account for effects of rupture propagation.

We use a ramp function of duration T for the displacement time function and make $T=L/V_r$, where V_r is the rupture velocity.

Similarly, the spectral energy density for a tensile fault with displacement normal to the fault plane (Haskell, 1964, equations 80 and 81) are:

$$E_p(\omega)^T = (\rho W^2 D^2 L^2 / 2\pi\alpha) |\hat{G}(\omega)|^2 B_3(\omega) \quad (\text{B-3})$$

$$E_s(\omega)^T = (\rho W^2 D^2 L^2 / 2\pi\beta) |\hat{G}(\omega)|^2 B_6(\omega) \quad (\text{B-4})$$

Instead of using a ramp function for $G(t)$ as above, we choose a trapezoidal time function. This function simulates a fault that opens and then closes in a time $T=W/V_r$. If we superimpose small tensile faults to a main longitudinal fault and assume that the faults are linearly independent, then the total spectral energy will be:

$$E_c(\omega) = E_c(\omega)^L + n E_c(\omega)^T \quad (\text{B-5})$$

where n is the number of tensile faults superimposed.

Then the P/S spectral energy ratio is:

$$\frac{E_p(\omega)}{E_s(\omega)} = \frac{E_p(\omega)^L + nE_p(\omega)^T}{E_s(\omega)^L + nE_s(\omega)^T} \quad (\text{B-6})$$

This energy ratio can be converted to displacement using equation (2-5) of the text (Haskell, 1967), i.e.:

$$\frac{U_p(\omega)}{U_s(\omega)} = \frac{\beta^{1/2} \{ [E_p(\omega)^L]^{1/2} + n[E_p(\omega)^T]^{1/2} \}}{\alpha^{1/2} \{ [E_s(\omega)^L]^{1/2} + n[E_s(\omega)^T]^{1/2} \}} \quad (\text{B-7})$$